UNIVERSITY OF CALIFORNIA
RIVERSIDE

Chemical Functionalization and Application of Graphene and Single-Walled Carbon Nanotubes

A Dissertation submitted in partial satisfaction
of the requirements for the degree of

Doctor of Philosophy

in

Chemical and Environmental Engineering

by

Xiaojuan Tian

March 2015

Dissertation Committee:
Dr. Robert C. Haddon, Chairperson
Dr. David Kisailus
Dr. Yadong Yin

The Dissertation of Xiaojuan Tian is approved:

_____

_____

_____

Committee Chairperson

University of California, Riverside

ACKNOWLEDGEMENT

It is a great experience being a member of the Haddon Research Group, where I learned to be a professional researcher under the help of so many talented scientists.

I wish to express my thanks to the current and former members of the Haddon group. Firstly, I give my thanks to Dr. Haddon. I sincerely thank him for providing me with the opportunity to work in the wonderful group and for leading me into the carbon nanomaterials field. I am always amazed by his in-depth knowledge in theory as an experimental scientist. He applies his solid theory knowledge coming up with new direction and explaining complicated results. This work could not have been done without his continuous support and sincere guidance. Secondly, my thanks go to Misha. He helped me so much since I joined the lab. He guided me in designing experiments, explaining results, writing papers and making presentations, always kindly and patiently. He can always find the value in a bunch of data, give reasonable explanations, and point the next step. Thirdly, I give my thanks to Elena. She mentored me in chemical projects. She supplied so much help in designing chemical instruments, discussing results and editing writing. Every time Elena helps in chemical reactions, I learn new skills. She helped with the XPS and UPS measurements in Chapter 2. Thanks to Aron for absorption and Raman characterizations of metal deposited SWNT films, and theory calculations for the effect of rational orientation on the absorption spectra of graphene film. Thanks to Feihu for

helping to set up the conductivity measurements system. Thanks to Santanu and Irina for teaching me chemical functionalization of SWNTs and GNPs, and their characterization. Thanks to Xiaobo for showing me the preparation and measurements of thermal composites. Thanks to Matt for experimental help of SWNTs films. Pradip and Sushanta are always helpful in chemical experiments. Thanks go to ladies in the Center for Nanoscale Science and Engineering: Nancy, Eva, Nadine, Andy and Amanda. I am also grateful to the staff in the cleanroom for all the help; they are Mark, Dong and Dexter.

I give special thanks to Dr. David Kisailus and Dr. Yadong Yin for taking the time to serve on my committee and review my work.

I wish to acknowledge the financial support from the Defense Microelectronics Activity (DMEA) under agreement number H94003-10-2-1003 and H94003-10-2-1004, and NSF under contract DMR-1305724.

Portions of the dissertation are adapted with permission from the following references:

Chapter 2: X. Tian, M. L. Moser, A. Pekker, S. Sarkar, J. Ramirez, E. Bekyarova, M. E. Itkis, R. C. Haddon, *Nano Lett.* **2014**, *14*, 3930.

Chapter 3: X. Tian, S. Sarkar, A. Pekker, M. L. Moser, I. Kalinina, E. Bekyarova, M. E. Itkis, R. C. Haddon, *Carbon* **2014**, *72*, 82.

Chapter 4: X. Tian, M. E. Itkis, E. Bekyarova, R. C. Haddon, *Sci. Rep.* **2013**, *3*, 1710.

ABSTRACT OF THE DISSERTATION

Chemical Functionalization and Application of Graphene and Single-Walled Carbon Nanotubes

by

Xiaojuan Tian

Doctor of Philosophy, Graduate Program in Chemical and Environmental Engineering
University of California, Riverside, March 2015
Dr. Robert C. Haddon, Chairperson

Graphene and single-walled carbon nanotubes (SWNTs) are new low dimensional carbon allotropes discovered in recent decades. They have attracted attention because of their unique features from the standpoint of new science and engineering applications. My thesis is focused on the chemical functionalization and applications of these new materials.

The covalent chemical functionalization of graphitic surfaces usually leads to the conversion of sp^2 carbon to sp^3, thus introducing defects and decreasing the charge carriers mobility. Recently, we discovered that the organometallic chemistry of graphitic surfaces results in the formation of an electronically conjugating, organometallic bis-hexahapto-graphene junction while maintaining

the electronic structure of the individual graphene nanostructures; such bonds involve minimal (structural) rehybridization.

Reduction of graphene oxide has been studied as promising method to produce graphene in a large scale, while the conjugation is usually not completely recovered. The characterization of the graphene derived materials and their degree of conjugation remains an important topic in carbon sciences. We have applied absorption spectroscopy and conductivity measurements to measure the conjugation degree of graphene derived materials.

The high thermal conductivity of a graphene layer makes graphite nanoplatelets (GNPs) promising fillers in thermal interface materials. As 2D materials, the orientation of GNPs in thermal composite was investigated. The electrical and thermal properties in in-plane and through-plane directions were measured, showing that the in-plane conductivity is higher than that in through-plane direction. Scanning electron microscopy (SEM) reveals that the anisotropy in the transport properties is due to the in-plane alignment of the GNPs which occurs during the formation of the thermal interface layer. Because the alignment in the thermal interface layer suppresses the through-plane component of the thermal conductivity, the anisotropy strongly degrades the performance of GNPs-based composites in the geometry required for typical thermal management applications and must be taken into account in the development of GNPs-based TIMs. Spherical microparticles were applied to disrupt the GNPs alignment. The

hybrid filler formulations reported herein resulted in a synergistic enhancement of the through-plane thermal conductivity of GNP/Al_2O_3 and GNP/Al filled TIM layers confirming that the control of GNP alignment is an important parameter in the development of highly efficient GNP and graphene-based TIMs.

Contents

List of Figures

Chapter 1. Introduction of Graphene and Carbon Nanotubes

1.1 Introduction of graphene

Carbon forms many kinds of allotropes partly due to its variable valency. The carbon allotropes attract attention for their value in basic science research and potential applications in engineering. Diamond and graphite are well known carbon allotropes, but in recent decades, low dimensional new carbon allotropes were discovered: 0D fullerenes,[1] 1D carbon nanotube,[2] and 2D graphene, [3-5] , among which the graphene sheet is the basic building block for the other materials. It can be transformed into fullerenes, rolled into carbon nanotube, and stacked to give graphite (Fig.1.1).

1.1.1 Synthesis of graphene

The existence of graphene was demonstrated through the mechanical exfoliation of graphite using scotch tape.[3] The graphene produced could be observed under an optical microscope on the Si/SiO_2 wafer of specific thickness. After that, scientists start to synthesize graphene besides obtaining it from natural sources. (Fig. 1.2)

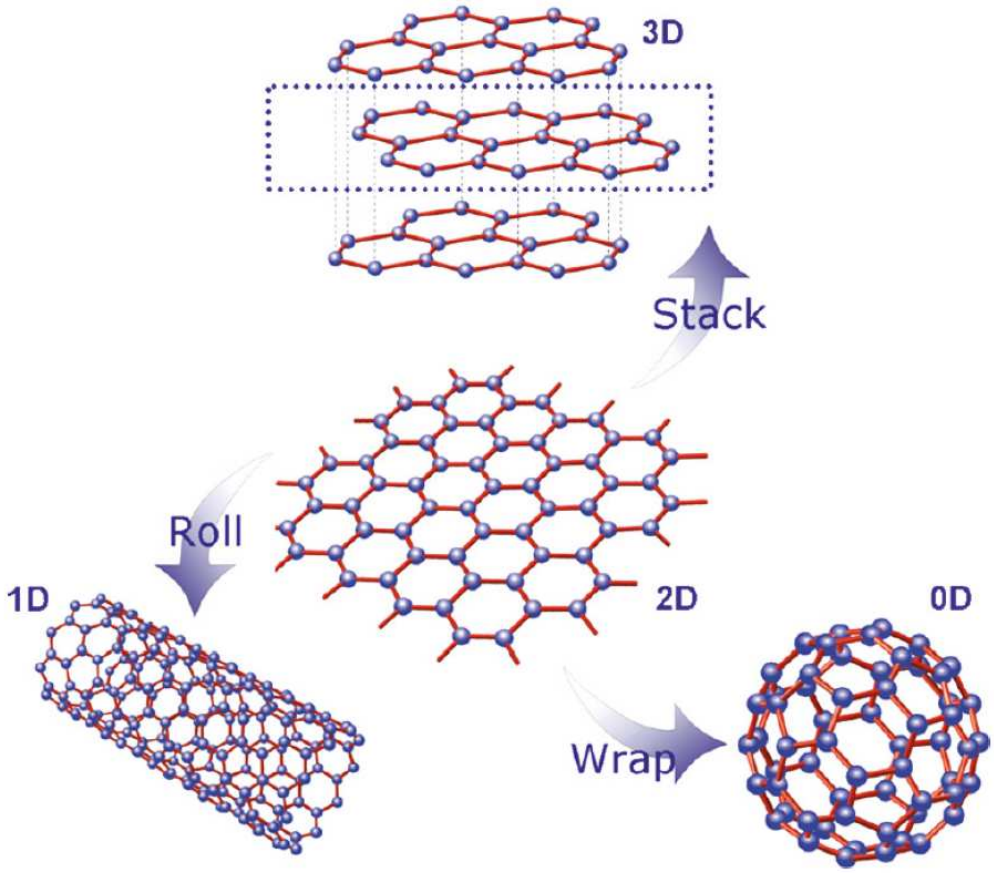

Figure 1.1 Graphene, 2D carbon atomic layer, is the basis for 0D fullerene, 1D carbon nanotubes, and 3D graphite. Reprinted with permission from ref. [6] Copyright (2012) American Chemical Society.

Chemical vapor deposition (CVD) graphene

CVD has been used as a popular method to grow graphene since 2008.[7-11] In the CVD process, a gas phase carbon source is fed into a furnace, decomposed to carbon radicals on the substrate surface, and forms graphene (Figure 1.3). Nickel and copper foil are commonly used as substrates.[7 8-10] The metal substrates act as a catalyst in the process and control the quality of the produced graphene.

It has been pointed out that the copper substrate helps to produce more uniform monolayer graphene than other substrates,[12] because the carbon solubility in copper is very low. In the CVD process, carbon atoms from the decomposition of gas source deposit on the Cu surface. After the first layer of graphene is formed, the substrate is not exposed to the vapor, thus losing its efficiency as a catalyst. The produced CVD graphene with metal substrate is not convenient for further applications in electronics. Methods have been developed to transfer the CVD graphene. A common method to transfer CVD graphene is to apply a polymer layer to allow handling. Usually, polymethyl methacrylate (PMMA) is spin coated on the graphene surface. In the next step the copper substrate is etched away. After cleaning in DI water, the graphene is transferred onto the target substrate and PMMA is removed by acetone.[13]

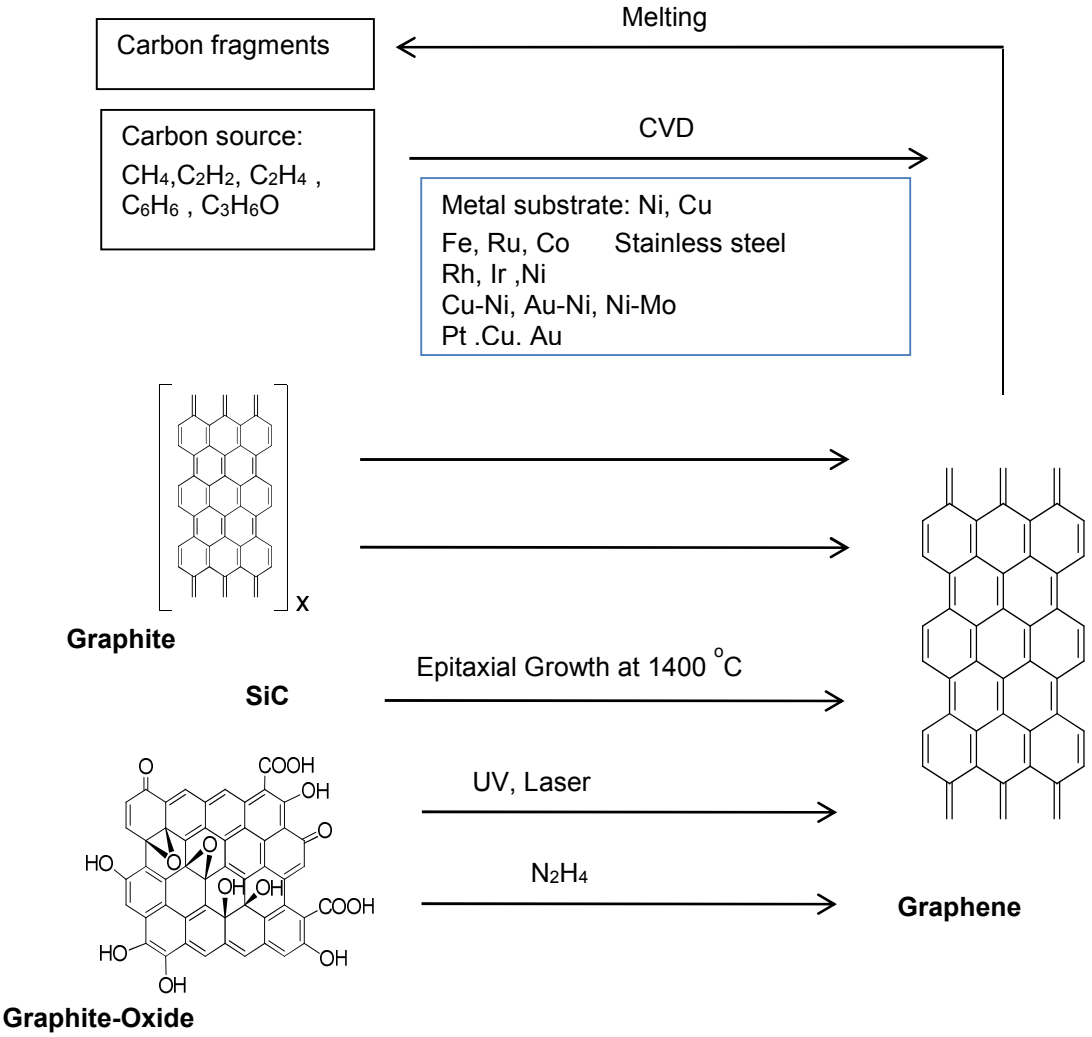

Figure 1.2 Synthesis of graphene. Reprinted with permission from ref. [14] Copyright (2013) American Chemical Society.

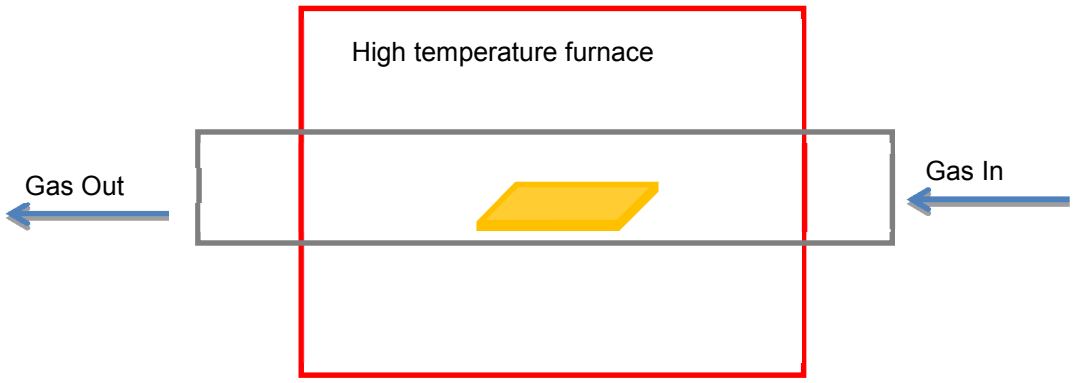

Figure 1.3 Synthesis of graphene by CVD method.

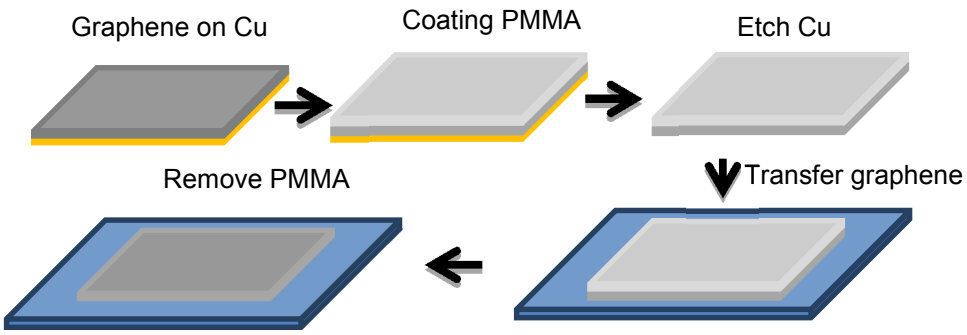

Figure 1.4 Transfer of CVD graphene.

Epitaxial graphene (EG)

Epitaxial graphene is grown on silicon carbide crystals at high temperature under vacuum. Although the EG usually consists of a few layers, the layers are non-interacting and show band structure of Dirac cone corresponding to a single layer graphene.[4, 15, 16]

Liquid exfoliated graphene

Liquid exfoliation has been developed to produce few layer graphene on a large scale. Powdered graphite is exfoliated under sonication in solvents such as dimenthylformamide (DMF), N-methyl-pyrrolidone (NMP), and ortho-dichlorobenzene.[17, 18] Transmission electron microscopy (TEM) is used to confirm the existence of single layer graphene.[17, 18] For few layer graphene with small lateral size, the D peak is visible in the Raman spectrum due to the high concentration of edges; the intensities of the D to G peak can be used to determine the lateral size of graphene flakes produced.[18] Besides organic solvents, aqueous surfactants can exfoliate graphite to few layer graphene.[19, 20] Liquid exfoliation is also efficient for other layered 2D materials, such as BN, MoS_2, and WS_2.[21, 22]

Reduced graphene oxide

Oxidation of graphite leads to the formation of graphite oxide, a material that has proven to be a viable starting point for a wide-range of applications. There are a range of oxygen functionalities and defects in graphite oxide [23-25], and due to its excellent solubility, particularly in water, it is widely employed as a graphene precursor.[23, 25, 26] Some common methods for graphite oxide production were developed by Brodie, [27] Staudenmaier, [28] and Hummers.[29] Hydroxyl groups, epoxide groups, carboxylic, and carbonyl groups are formed after oxidation based on solid state ^{13}C NMR spectroscopy and Mid-IR spectroscopy.[30-32] Graphite oxide is composed of layered graphene oxide. It is hyphophilic and water molecules can intercalate between graphene oxide layers, and then exfoliate it into graphene oxide sheets under sonication.[33, 34] Graphene oxide sheets have negative charges in water and the electrostatic repulsion results in their stable dispersions.[35] The graphene oxide can be reduced to partially recover the electronic conjugation and a variety of methods have been developed for reduction of graphene oxide.[36] Commonly used chemical reduced reagents are hydrazine,[37, 38] hydroquinone,[39] and $NaBH_4$.[40] Thermal methods are also applied to reduce graphene oxide.[41]

Graphite nanoplatelets (GNPs)

Graphite nanoplatelets (GNPs) are 2D graphitic materials consisting of a few stacked graphene layers. The thickness of GNPs varies from sub-nanometer

to tens of nanometers range, and their lateral dimensions are usually in the one to tens of micrometers range resulting in a very high aspect ratio. GNPs are usually prepared by intercalation and exfoliation of graphite, followed by a pulverization treatment. The various intercalation, exfoliation, and pulverization treatments result in a range of GNP size distributions. Acid intercalation is the most commonly used technique,[42-45] which is usually conducted by immersing the natural graphite into a mixture of concentrated sulfuric and nitric acid. Oxidizers can also be added into the acid solution to act as intercalants. The next step following intercalation is exfoliation: in the exfoliation process, rapid heating is applied to the intercalated graphite forcing its dramatic expansion due to the generation of a large volume of gas. Besides heating, microwave irradiation has also been used to provide sufficient energy to promote the expansion of intercalated graphite.[46-48] Lastly, to obtain GNPs, a pulverization treatment is applied to break down the worm-like exfoliated graphite. Shear mixing, ultrasonication and ball milling are commonly used methods; the pulverization treatment plays an important role in the size distribution of the resulting GNPs, which affects the properties of GNP-based composites.[49, 50] GNPs can also be produced utilizing alkali metal and molecular intercalants. [51, 52]

1.1.2 Structure and properties of graphene

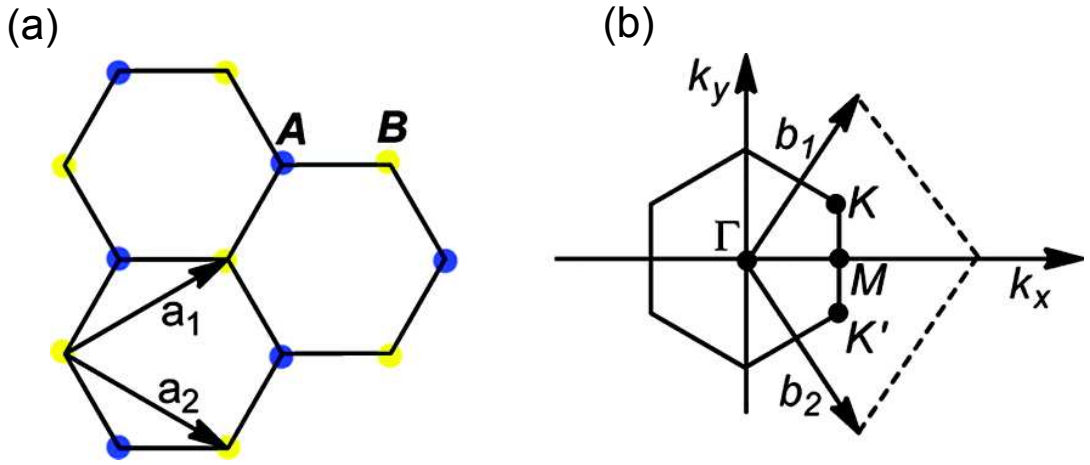

Figure 1.5 (a) Graphene honeycomb lattice, a_1 and a_2 are the unit vectors. (b) The corresponding Brillouin zone in momentum space. Reprinted with permission from ref.[53] Copyright (2009) American Physical Society.

The electronic structure of graphene attracts attention for its unique properties. Carbon atoms lie in a hexagonal structure in the graphene lattice. From the standpoint of crystallography, the honeycomb structure of graphene contains two different types of carbon atoms, labelled as A and B in Figure 1.5. [53]

The primitive lattice vectors are $\mathbf{a}_1 = (3a/2)\,\mathbf{i} + (\sqrt{3}a/2)\,\mathbf{j}$ and $\mathbf{a}_2 = (3a/2)\,\mathbf{i} - (\sqrt{3}a/2)\,\mathbf{j}$, where a=1.421 Å is the carbon-carbon bond length; the reciprocal lattice vectors are $\mathbf{b}_1 = (\frac{2\pi}{3a})\,\mathbf{i} + (\frac{2\sqrt{3}\pi}{3a})\,\mathbf{j}$ and $\mathbf{b}_2 = (\frac{2\pi}{3a})\,\mathbf{i} - (\frac{2\sqrt{3}\pi}{3a})\,\mathbf{j}$. Figure 1.5 (b) shows the Brillouin zone of the graphene. The six corners of the Brillouin zone are named the Dirac points. Due to the symmetry, only K and K′ are unique. Their positions are given by $K= (\frac{2\pi}{3a}, \frac{2\pi}{3a\sqrt{3}})$, $K' =(\frac{2\pi}{3a}, -\frac{2\pi}{3a\sqrt{3}})$. And the remaining four are related by symmetry. The Dirac points are of great importance in the electronic structure, transport properties and chemistry of graphene.

The electronic properties of graphene can be simply analyzed by utilizing the tight-binding approach. [54-56]

Figure 1.6 (a) shows the electronic dispersion in the honeycomb lattice. The conduction and valence bands touch at the Dirac points resulting in zero band gap. The energy at all corners of Brillouin zone is zero. Thus perfect single-layer graphene is a semimetal or a zero-band-gap semiconductor. The band structure at the K or K′ is magnified in (Figure 1.6(b)), showing the Dirac cones.

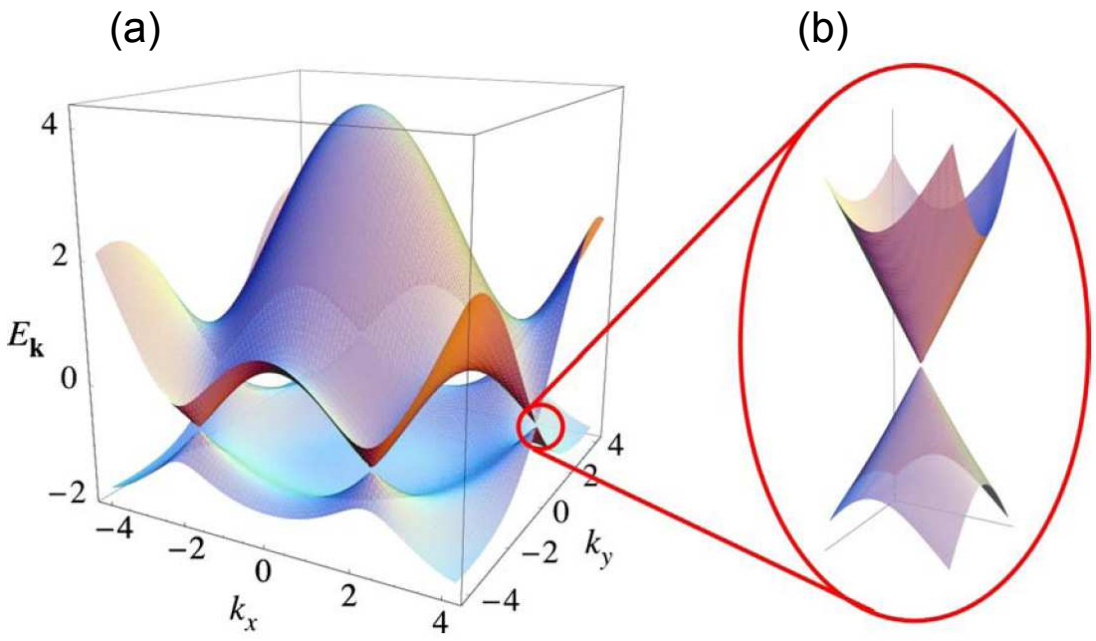

Figure 1.6 (a) Graphene band structure. (b) The band structure in the vicinity of the K and K′ points showing the Dirac cones. Reprinted with permission from ref.[53] Copyright (2009) American Physical Society.

Graphene has unique electron transport properties. In graphene, the highest hole and electrons mobilities are quite similar exceeding 15000 $cm^2/V/s$ in exfoliated graphene, [3, 5, 57-59] and much higher in epitaxial graphene nanoribbons.[60]

Graphene is also an excellent thermal conductor. For a suspended single layer graphene, a thermal conductivity as high as 5000 W/mK at room temperature is reported, which is higher than the thermal conductivity of other

carbon allotropes.[61] The suspension reduces the thermal coupling and scattering from the substrate. When graphene is on substrate, a thermal conductivity of 600 W/mK is measured.[62] The high thermal conductivity of graphene makes it promising for fillers in thermal interface materials.

1.1.3 Chemical reactivity of graphene

From the standpoint of chemistry, the A, B carbon atoms in the honeycomb lattice are equivalent,[63] although crystallographically distinct. The simple tight binding band structure of graphene at the level of Huckel Molecular Orbital Theory (HMO theory) is presented in Figure 1.7, which shows the dispersions of the π-bands in momentum space. [63, 64] The intersection of the valence and conduction bands at the Dirac point (K) defines the work function of graphene (W ≈ 4.6 eV), which corresponds to the level of the nonbonding molecular orbital (NBMO = -W) in HMO theory and also defines the highest occupied molecular orbital (HOMO) and lowest unoccupied molecular orbital (LUMO) of graphene. The existence of a very high lying HOMO and low lying LUMO in conjunction with the orbital symmetries at the Dirac point are of importance for the facile reactivity of graphene. [63-65]

The intra-layer conjugation and interlayer van der Waals forces make few layer graphene quite stable and not easy to modify. Ideally, graphene is an infinite 2D sheet of all sp^2-carbon atoms.[66] However, in real graphene, there are edges effects, basal plane fluctuations, atom vacancies and impurities, which

increases its chemical reactivity.[66] Practically, graphene is supported on the underlying substrate which affects its chemical reactivity.[67]

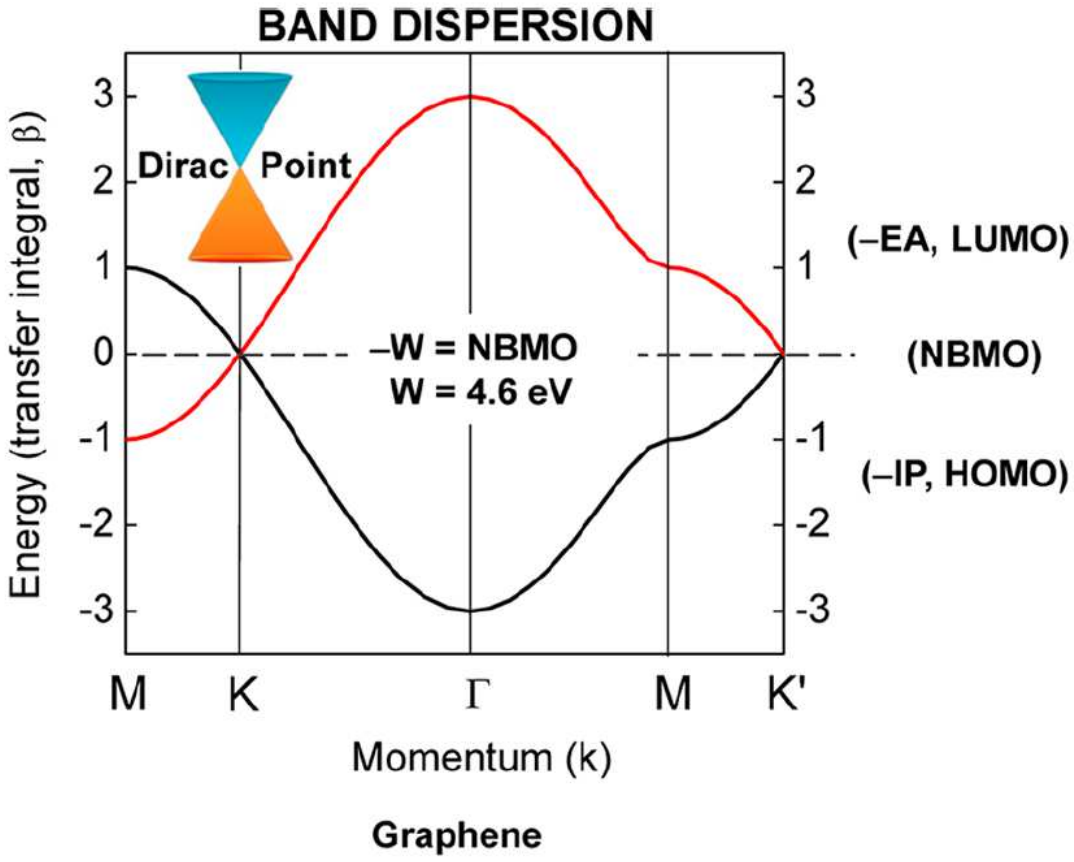

Figure 1.7 Simple tight binding band structure of graphene at the level of Huckel Molecular Orbital Theory (HMO theory) Reprinted with permission from Ref. [64] Copyright (2013) American Chemical Society.

1.1.4 Characterization of graphene

Characterization is of importance to understand the intrinsic properties of graphene and monitor changes introduced by external modification. Most characterization techniques for graphene involve microscopy and spectroscopy. They are used to determine the number of layers and the quality of graphene. The optical microscope can observe the graphene on silicon/ SiO_2 substrate. The visibility results from the reflection at the air-graphene-SiO_2 interfaces. The thickness of SiO_2 and light wavelength also affect its visibility.[68, 69]

Scanning electron microscopy (SEM) can also be used for observing graphene. For different number of graphene layers, the contrast in SEM image varies. Transmission electron microscopy (TEM) can directly show the number of layers by viewing the edge of sample.

Another commonly used characterization technique for graphene is Raman spectroscopy. In the Raman spectra of graphene, a first order Raman effect results in the G peak (~ 1580 cm^{-1}), where the energy of the scattered incident monochromatic light is proportional to the energy of quantized lattice vibrations (E_{2g} phonon).[70-74] The 2D peak (2670 cm^{-1}) is from a second order Raman effect, which arises from lattice vibrations when first order processes activate another phonon. For a single-layer graphene (SLG), the intensity of 2D peak is higher than the intensity of G-peak. The ratio of the intensities of 2D to G peak indicates the number of graphene layers.[70]

The covalent chemical modification of graphene usually results in conversion of sp^2 hybridized carbons to sp^3, which activates the A_{1g} breathing vibration mode and results in a D peak (ω_D ~1345 cm^{-1}). Chemical functional groups attached to graphene surface can be detected by infrared spectroscopy. Appearance of D peak can also originate from physically defective graphitic materials, such as graphene nanoribbons (GNRs), the edges of graphene, and disordered graphene samples. For the D peak resulting from graphene edges, the ratio of intensities of D to G peak has a linear relationship with lateral size of graphene.[18]

Raman spectra also provide information about quality of the samples,[75] and types and degree of doping (based on observed shift of G and 2D band).[76]

1.2 Introduction of carbon nanotubes

Carbon nanotubes can be imagined as being produced by rolling a graphene sheet. In 1991, Iijima of the NEC laboratory in Tsukuba, Japan observed multiwall carbon nanotube using high resolution transmission electron microscopy (HR-TEM). [2]

Since Iijima's observation, many scientists enter into the carbon nanotube field. People are attracted into the field because of the 1D quantum effects predicted for carbon nanotubes' electronic properties. The unique structure and properties of carbon nanotubes make them promising for applications. Two years

after Iijima's observation of multiwall carbon nanotubes (MWNTs) [2], single wall carbon nanotubes (SWNTs) were discovered.[77, 78]

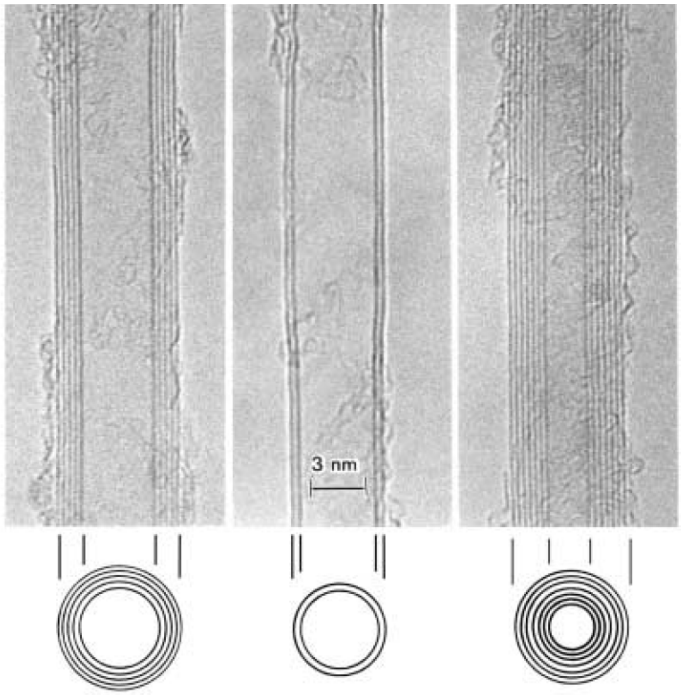

Figure 1.8 Multi-walled carbon nanotubes (MWNTs) observed by Iijima under HR-TEM in 1991. Reprinted with permission from Ref. [2] Copyright (1991) Nature Publishing Group

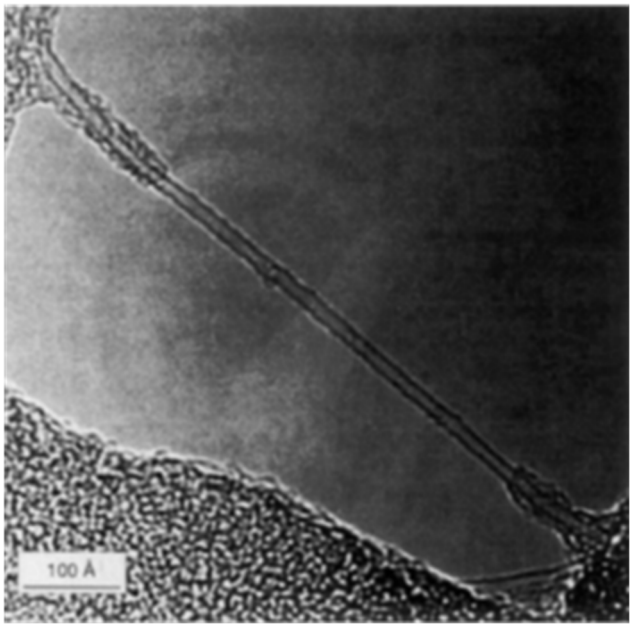

Figure 1.9 TEM image of single-walled carbon nanotube (SWNTs) synthesized by Bethune in 1993. Reprinted with permission from Ref. [78] Copyright (1993) Nature Publishing Group

1.2.1 Synthesis of carbon nanotubes

Several methods are applied to produce carbon nanotubes, including electric arc (EA) method, [77 79] laser ablation (LA), [79 80] chemical vapor deposition (CVD), [81-83] and tubular fluidized bed method. [84] Varying parameters processed and methods applied produce CNTs with different diameter, length and type (SWNTs, MWNTs). Five popular types of SWNTs are in use: EA-SWNTs, Laser-

SWNTs, CVD-SWNTs, HiPco-SWNTs and CoMoCat SWNTs. The EA-SWNTs can be prepared in bulk scale, but are of moderate purity. The laser method results in high quality nanotubes but the yield is low. The production of SWNTs with controlled diameter, length and chirality still remains a challenge.

1.2.2 Structure and properties of carbon nanotubes

SWNT can be visualized as a seamless cylinder formed by rolling graphene sheet along a chiral vector $C_h = n\overrightarrow{a_1} + m\overrightarrow{a_2}$. The structure of SWNT depends on the pair of integers (n, m). The chiral angle θ and unit vectors $\overrightarrow{a_1}$ and $\overrightarrow{a_2}$ are shown in Figure 1.10.[85] A zigzag nanotube is formed if a graphene sheet is rolled along the direction where θ=0°. The armchair nanotube corresponds to θ=30° and $0° < \theta < 30°$ correspond to the chiral nanotubes. The diameter of SWNT is calculated as $d = \sqrt{3}a_{c-c}\sqrt{n^2 + nm + m^2}$ where $a_{c\text{-}c}$=0.142nm is the carbon to carbon distance, and the chiral angel is $\theta = tan^{-1}[\frac{\sqrt{3}n}{2m+n}]$. In the case of armchair nanotube, m=n, while in the case of zigzag nanotube, m=0 or n=0; the other types are called chiral nanotubes.

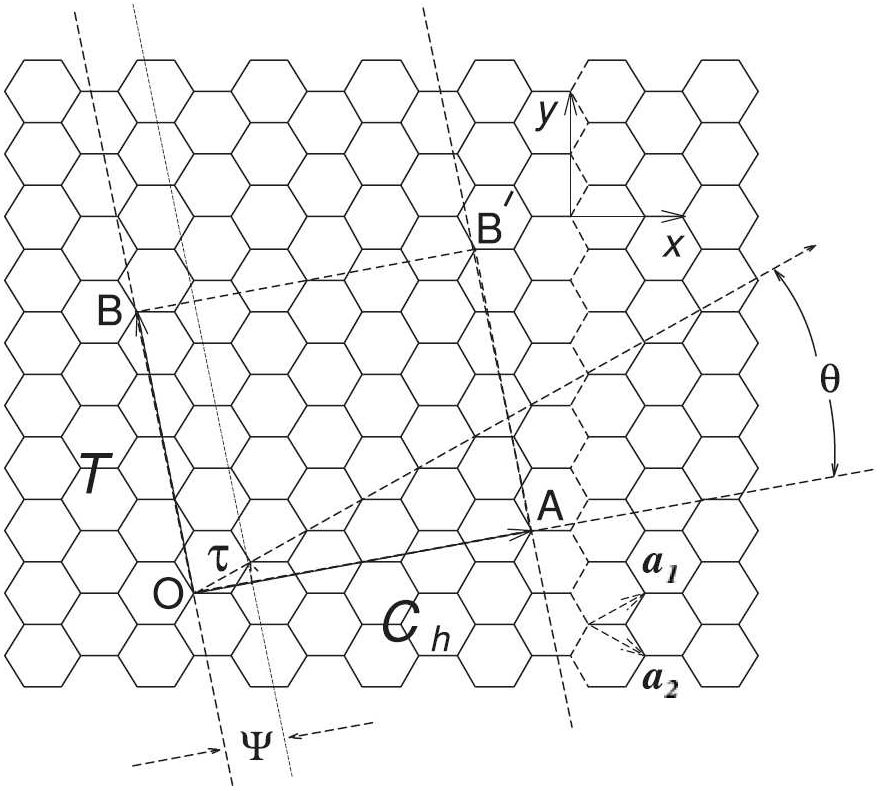

Figure 1.10 Chiral vector and chiral angel of SWNTs. Reprinted with permission from Ref. [85] Copyright (2001) Springer.

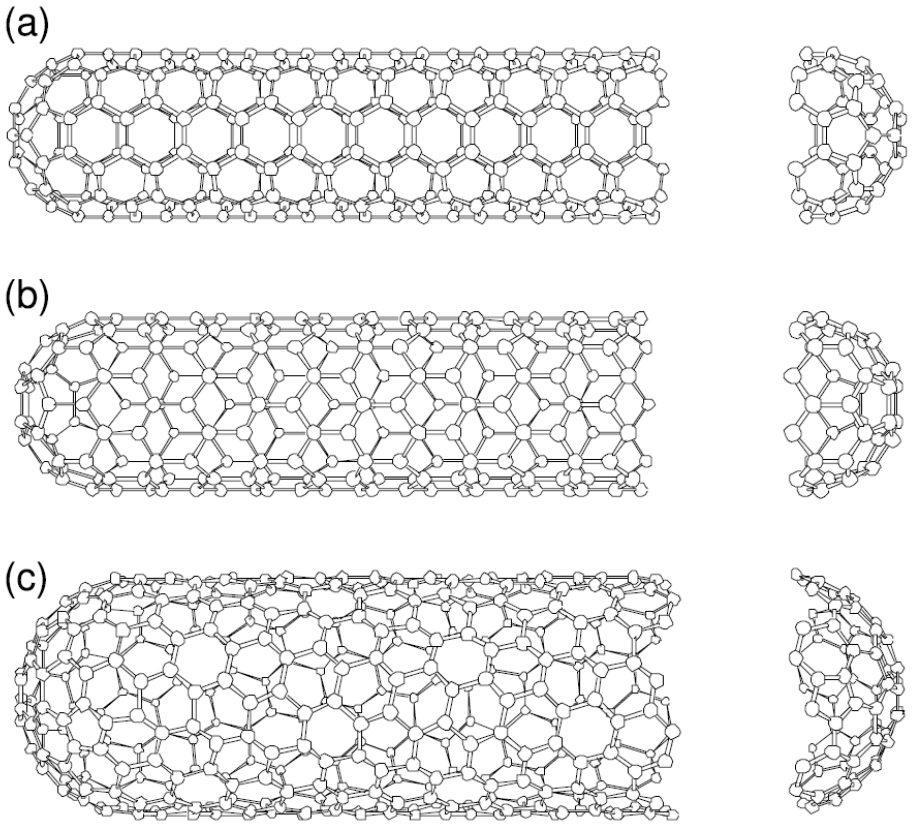

Figure 1.11 Scheme of (a) armchair, (b) zigzag, and (c) chiral nanotubes. Reprinted with permission from Ref. [85] Copyright (2001) Springer.

The electronic properties of SWNTs depend on their structures. Since graphene and SWNTs are composed of all sp^2 hybridized carbon, band structure theory of graphite is applied as simple model to calculate band structure of SWNTs. Graphene has zero band gap. The valence and conduction bands touch

at Dirac points. SWNT could be considered as 1D tube formed by rolling graphene sheet along the chiral vector Ch, and the allowed 1D subbands of SWNT fulfill the periodic boundary conditions imposed by Ch. The quantized states are $C_h \cdot k = 2\pi q$ where q is an integer, and k is the wavevector quantized along the circumferential direction. The nanotube is metallic if there are subbands passing through one of the K points, The armchair tubes (n.n) are metallic. For zigzag (n,0) or chiral (n,m) type, the tube is metallic only if (n-m)/3 is an integer. All other cases correspond to semiconducting SWNT. The energy gap of semiconducting nanotube is inversely proportional to its diameter.

Scanning tunneling spectroscopy experiments confirmed the presence and theoretical assignments of metallic and semiconducting SWNTs in 1998.[86, 87] The electronic transitions between the energy bands of SWNTs can be observed by standard spectroscopic technique. [88-91]

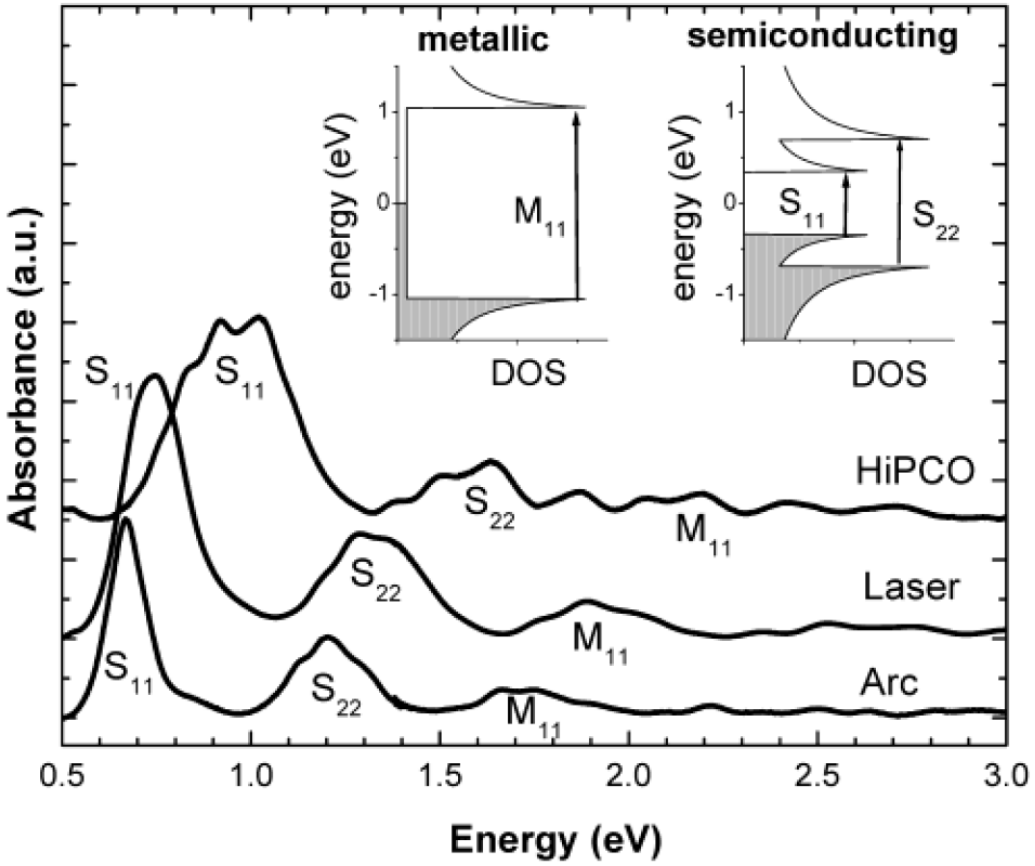

Figure 1.12 Electronic transitions between the SWNTs energy bands observed by spectroscopic techniques. Reprinted with permission from Ref. [91] Copyright (2002) American Chemical Society.

Charge carriers in individual semiconducting SWNT have extraordinary mobilities, as high as 10^5 cm^2 /s/V.[92, 93] Thin films prepared from purified SWNTs have conductivities of 250-400 S/cm.[94] The electronic properties of SWNT thin films are sensitive to chemical doping. The SWNT thin film networks have been shown to be promising materials for next generation electronic devices[95-99]

In theory, the thermal conductivity of a single SWNT can reach 6000 W/mK.[100] A thermal conductivity of 3000 W/mK was measured for individual MWNT.[101] The measured thermal conductivity of SWNT film was around 100 W/mK.[102]

The mechanical properties of CNTs are also outstanding. Tensile strength of CNTs is two orders of magnitude higher than steel.[103] The calculated Young's modulus for an individual (10,10) SWNT is ~0.64 TPa and 1.47 TPa for a bundle of 15 SWNTs. [104] Measured Young's modulus of MWNTs is 1-2 TPa, and the bending strength of individual MWNTs is 28.5 GPa.[105, 106]

1.2.3 Chemical reactivity of carbon nanotubs

A perfect SWNT is composed of all sp^2 hybridized carbon and the electron conjugation makes it quite stable. SWNT has local strains from curvature-induced pyramidalization and mis-alignment of the π-orbitals, which makes it more reactive than flat graphene sheet. [90, 107-113] At the level of chemistry, carbon nanotubes sites can be classified into two regions: the end caps and sidewall. The sidewall carbon is less reactive than those in the end cap.[91]

Dissolution of SWNTs is important because most synthetic chemistry and biological processes occur in solution, and many characterization techniques require the solution stte. When SWNTs were just recognized, it was found that SWNTs are very difficult to be wetted.[114] They usually exist as bundles and aggregates in solid state and there are no surface functional groups on SWNTs. These factors result in their difficulties in dispersing in organic solvents.[107]

One way commonly applied to disperse SWNTs is the treatment in refluxing nitric acid, which oxidizes end caps to carboxylic acid and other weakly acidic functionalities.[115-117] With the help of sonication, the acid treated SWNT material is dispersed in organic solvents.[118] The nitric acid also purifies the SWNTs by removing metal catalysts and amorphous carbon. At the same time, defects are introduced on the nanotube surface. [119]

The other way to disperse SWNT is the addition of long-chain hydrocarbon at the ends of SWNTs. The acid functionality in SWNTs is converted to amide of octadecylamine (ODA).[88] The amide bond formation can be confirmed by mid-IR spectroscopy. The long-chain hydrocarbon is helpful to disrupt and compensate for the loss of van der walls attraction in SWNT bundles. Bulky side chain can also be added by other types of amide bond or ester bond. [120-125]

References

1. Kroto, H. W.; Heath, J. R.; O'Brien, S. C.; Curl, R. F.; Smalley, R. E. *Nature* **1985,** 318, 162.

2. Iijima, S. *Nature* **1991,** 354, 56.

3. Novoselov, K. S., et al. *Science* **2004,** 306, 666.

4. Berger, C., et al. *J. Phys. Chem. B* **2004,** 108, 19912.

5. Novoselov, K. S., et al. *Nature* **2005,** 438, 197.

6. Wan, X.; Huang, Y.; Chen, Y. *Acc. Chem. Res.* **2012,** 45, 598.

7. Yu, Q. K., et al. *App. Phys. Lett.* **2008,** 93, 113103.

8. Chae, S. J., et al. *Adv. Mater.* **2009,** 21, 2328.

9. De Arco, L. G.; Zhang, Y.; Kumar, A.; Zhou, C. W. *IEEE Trans. Nanotechnol.* **2009,** 8, 135.

10. Li, X. S., et al. *Science* **2009,** 324, 1312.

11. Reina, A., et al. *Nano Lett.* **2009,** 9, 30.

12. Zhang, Y.; Zhang, L.; Zhou, C. *Acc. Chem. Res.* **2012,** 46, 2329.

13. Suk, J. W., et al. *ACS Nano* **2011,** 5, 6916.

14. Haddon, R. C. *Acc. Chem. Res.* **2013,** 46, 1.

15. Ohta, T.; Bostwick, A.; Seyller, T.; Horn, K.; Rotenberg, E. *Science* **2006,** 313, 951.

16. Wu, X.; Li, X.; Song, Z.; Berger, C.; De Heer, W. A. *Phys. Rev. Lett.* **2007,** 98, 136801.

17. Hernandez, Y., et al. *Nature Nanotech.* **2008,** 3, 563.

18. Khan, U.; O'Neill, A.; Lotya, M.; De, S.; Coleman, J. N. *Small* **2010,** 6, 864.

19. Lotya, M., et al. *J. Am. Chem. Soc* **2009,** 131, 3611.

20. Lotya, M.; King, P. J.; Khan, U.; De, S.; Coleman, J. N. *ACS Nano* **2010,** 4, 3155.

21. Coleman, J. N., et al. *Science* **2011,** 331, 568.

22. Coleman, J. N. *Acc. Chem. Res.* **2013,** 46, 14.

23. Marcano, D. C., et al. *ACS Nano* **2010,** 4, 4806.

24. Erickson, K., et al. *Adv. Mater.* **2010,** 22, 4467.

25. Dreyer, D. R.; Park, S.; Bielawski, C. W.; Ruoff, R. S. *Chem. Soc. Rev.* **2010,** 39, 228.

26. Stankovich, S., et al. *Nature* **2006,** 442, 282.

27. Brodie, B. C. *Ann. Chim. Phys.* **1860,** 59, 466.

28. Staudenmaier, L. *Ber. Dtsch. Chem. Ges.* **1898,** 31, 1481.

29. Hummers, W. S.; Offeman, R. E. *J. Am. Chem. Soc.* **1958,** 80, 1339.

30. He, H. Y.; Riedl, T.; Lerf, A.; Klinowski, J. *J. Phys. Chem.* **1996,** 100, 19954.

31. Lerf, A.; He, H. Y.; Forster, M.; Klinowski, J. *J. Phys. Chem. B* **1998,** 102, 4477.

32. Tian, X., et al. *Carbon* **2014,** 72, 82.

33. Lerf, A., et al. *J. Phys. Chem. Solids.* **2006,** 67, 1106.

34. Stankovich, S., et al. *J. Mater. Chem.* **2006,** 16, 155.

35. Li, D.; Muller, M. B.; Gilje, S.; Kaner, R. B.; Wallace, G. G. *Nature Nanotech.* **2008,** 3, 101.

36. Park, S.; Ruoff, R. S. *Nature Nanotech.* **2009,** 4, 217.

37. Stankovich, S., et al. *Carbon* **2007,** 45, 1558.

38. Tung, V. C.; Allen, M. J.; Yang, Y.; Kaner, R. B. *Nature Nanotech.* **2009,** 4, 25.

39. Wang, G. Z.; Shen, X.; Wang, B.; Yao, J.; Park, J. *Carbon* **2009,** 47, 1359.

40. Shin, H. J., et al. *Adv. Funct. Mater.* **2009,** 19, 1987.

41. Becerril, H. A., et al. *ACS Nano* **2008,** 2, 463.

42. Debelak, B.; Lafdi, K. *Carbon* **2007,** 45, 1727.

43. Cho, D.; Lee, S.; Yang, G.; Fukushima, H.; Drzal, L. T. *Macromol. Mater. and Eng.* **2005,** 290, 179.

44. Chen, G. H., et al. *Carbon* **2004,** 42, 753.

45. Yasmin, A.; Luo, J. J.; Daniel, I. M. *Compos. Sci. Technol.* **2006,** 66, 1182.

46. Zhu, Y., et al. *Carbon* **2010,** 48, 2118.

47. Hendricks, T. R.; Lu, J.; Drzal, L. T.; Lee, I. *Adv. Mater.* **2008,** 20, 2008.

48. Kalaitzidou, K.; Fukushima, H.; Drzal, L. T. *Compos. Part A: Appl. Sci.* **2007,** 38, 1675.

49. Raza, M. A.; Westwood, A.; Brown, A.; Hondow, N.; Stirling, C. *Carbon* **2011,** 49, 4269.

50. Raza, M. A.; Westwood, A. V. K.; Brown, A. P.; Stirling, C. *Comp. Sci. Technol.* **2012,** 72, 467.

51. Viculis, L. M.; Mack, J. J.; Mayer, O. M.; Hahn, T.; Kaner, R. B. *J. Mater. Chem.* **2005,** 15, 974.

52. Mack, J. J., et al. *Adv. Mater.* **2005,** 17, 77.

53. Castro Neto, A. H.; Guinea, F.; Peres, N. M. R.; Novoselov, K. S.; Geim, A. K. *Rev. Mod. Phys.* **2009,** 81, 109.

54. Wallace, P. R. *Phys. Rev.* **1947,** 71, 622.

55. Saito, R.; Fujita, M.; Dresselhaus, G.; Dresselhaus, M. S. *Appl. Phys. Lett.* **1992,** 60, 2204.

56. Saito, R.; Dresselhaus, G.; Dresselhaus, M. S., *Physical Properties of Carbon Nanotubes*. Imperial College Press: Singapore, 1998.

57. Novoselov, K. S., et al. *Proc. Nat. Acad. Sci. USA* **2005,** 102, 10451.

58. Zhang, Y.; Tan, Y. W.; Stormer, H. L.; Kim, P. *Nature* **2005,** 438, 201.

59. Geim, A. K.; Novoselov, K. S. *Nature Mater.* **2007,** 6, 183.

60. Baringhaus, J., et al. *Nature* **2014,** 506, 349.

61. Balandin, A. A., et al. *Nano Lett.* **2008,** 8, 902.

62. Seol, J. H., et al. *Science* **2010,** 328, 213.

63. Sarkar, S.; Bekyarova, E.; Haddon, R. C. *Acc. Chem. Res.* **2012,** 45, 673.

64. Bekyarova, E., et al. *Acc. Chem. Res.* **2013,** 46, 65.

65. Sarkar, S.; Bekyarova, E.; Niyogi, S.; Haddon, R. C. *J. Am. Chem. Soc.* **2011,** 133, 3324.

66. Yan, L., et al. *Chem. Soc. Rev.* **2012,** 41, 97.

67. Wang, Q. H., et al. *Nature Chem.* **2012,** 4, 724.

68. Roddaro, S.; Pingue, P.; Piazza, V.; Pellegrini, V.; Beltram, F. *Nano Lett.* **2007,** 7, 2707.

69. Blake, P., et al. *Appl. Phys. Lett.* **2007,** 91, 063124.

70. Ferrari, A. C., et al. *Phys. Rev. Lett.* **2006,** 97, 187401.

71. Ferrari, A. C. *Solid State Commun.* **2007,** 143, 47.

72. Malard, L. M.; Pimenta, M. A.; Dresselhaus, G.; Dresselhaus, M. S. *Phys. Report* **2009,** 473, 51.

73. Niyogi, S., et al. *Nano. Lett.* **2010,** 10, 4061–4066.

74. Niyogi, S., et al. *J. Phys. Chem. Lett.* **2011,** 2, 2487.

75. Lucchese, M. M., et al. *Carbon* **2010,** 48, 1592.

76. Dong, X. C., et al. *Small* **2009,** 5, 1422.

77. Iijima, S.; Ichihashi, T. *Nature* **1993,** 363, 603.

78. Bethune, D. S., et al. *Nature* **1993,** 363, 605.

79. Journet, C., et al. *Nature* **1997,** 388, 756.

80. Guo, T.; Nikolaev, P.; Thess, A.; Colbert, D. T.; Smalley, R. E. *Chem. Phys. Lett.* **1995,** 243, 49.

81. Dai, H., et al. *Chem. Phys. Lett.* **1996,** 260, 471.

82. Nikolaev, P., et al. *Chem. Phys. Lett.* **1999,** 313, 91.

83. Joselevich, E.; Lieber, C. M. *Nano Lett.* **2002,** 2, 1137.

84. Kitiyanan, B.; Alvarez, W. E.; Harwell, J. H.; Resasco, D. E. *Chem. Phys. Lett.* **2000,** 317, 497.

85. Dresselhaus, M. S.; Dresselhaus, G.; Avouris, P., *Carbon Nanotubes: Synthesis, Structure, Properties and Applications*. Springer-Verlag: Berlin, 2001; Vol. 80.

86. Wildoer, J. W. G.; Venema, L. C.; Rinzler, A. G.; Smalley, R. E.; Dekker, C. *Nature* **1998,** 391, 59.

87. Odom, T. W.; Huang, J.-L.; Kim, P.; Lieber, C. M. *Nature* **1998,** 391, 62.

88. Chen, J., et al. *Science* **1998,** 282, 95.

89. Itkis, M. E., et al. *Nano Lett.* **2002,** 2, 155.

90. Hamon, M. A., et al. *J. Am. Chem. Soc.* **2001,** 123, 11292.

91. Niyogi, S., et al. *Acc. Chem. Res.* **2002,** 35, 1105.

92. Durkop, T.; Getty, S. A.; Cobas, E.; Fuhrer, M. S. *Nano Lett.* **2004,** 4, 35.

93. Dai, H. *Acc. Chem. Res.* **2002,** 35, 1035.

94. Bekyarova, E., et al. *J. Am. Chem. Soc.* **2005,** 127, 5990.

95. Bradley, K.; Gabriel, J.-C. P.; Gruner, G. *Nano Lett.* **2003,** 3, 1353.

96. Snow, E. S.; Campbell, P. M.; Ancona, M. G.; Novak, J. P. *Appl. Phys. Lett.* **2005,** 86, 033105.

97. Stadermann, M., et al. *Phys. Rev. B* **2004,** 69, 201402.

98. Hu, L.; Hecht, D. S.; Gruner, G. *Nano Lett.* **2004,** 4, 2513.

99. Kang, S. J., et al. *Nature Nanotech.* **2007,** 2, 230.

100. Hone, J.; Whitney, M.; Piskoti, C.; Zettl, A. *Phys. Rev. B* **1999,** 59, R2514.

101. Kim, P.; Shi, L.; Majumdar, A.; McEuen, P. L. *Phys. Rev. Lett.* **2001,** 87, 215502.

102. Itkis, M. E.; Borondics, F.; Yu, A.; Haddon, R. C. *Nano Lett.* **2007,** 7, 900.

103. Yakobson, B. I.; Smalley, R. E. *American Scientist* **1997,** 85, 324.

104. Gao, G.; Cagin, T.; Goddard III, W. A. *Nanotechnology* **1998,** 9, 184.

105. Treacy, M. M. J.; Ebbsen, T. W.; Gibson, J. M. *Nature* **1996,** 381, 678.

106. Wong, E. W.; Sheehan, P. E.; Lieber, C. M. *Science* **1997,** 277, 1971.

107. Chen, Y., et al. *J. Mater. Res.* **1998,** 13, 2423.

108. Haddon, R. C. *Science* **1993,** 261, 1545.

109. Haddon, R. C. *J. Am. Chem. Soc.* **1990,** 112, 3385.

110. Scott, L. T.; Bratcher, M. S.; Hagen, S. *J. Am. Chem. Soc.,* **1996,** 118, 8743.

111. Haddon, R. C.; Raghavachari, K. *Tetrahedron* **1996,** 52, 5207.

112. Weedon, B. R.; Haddon, R. C.; Spielmann, H. P.; Meier, M. S. *J. Am. Chem. Soc.* **1999,** 121, 335.

113. Bodwell, G. J.; Bridson, J. N.; Houghton, T. J.; Kennedy, J. W. J.; Mannion, M. R. *Chem. Eur. J.* **1999,** 5, 1823.

114. Dujardin, E.; Ebbesen, T. W.; Krishnan, A.; Treacy, M. M. J. *Adv. Mater.* **1998,** 10, 1472.

115. Ebbesen, T. W. *Acc. Chem. Res.* **1998,** 31, 558.

116. Mawhinney, D. B., et al. *Chem. Phys. Lett.* **2000,** 324, 213.

117. Hu, H., et al. *Chem. Phys. Lett.* **2001,** 345, 25.

118. Ausman, K. D.; Piner, R.; Lourie, O.; Ruoff, R. S.; Korobov, M. *J. Phys. Chem. B* **2000,** 104, 8911.

119. Monthioux, M., et al. *Carbon* **2001,** 39, 1251.

120. Riggs, J. E.; Guo, Z.; Carroll, D. L.; Sun, Y.-P. *J. Am. Chem. Soc.* **2000,** 122, 5879.

121. Sun, Y. P., et al. *Chem. Mater.* **2001,** 13, 2864.

122. Banerjee, S.; Wong, S. S. *Nano Lett.* **2002,** 2, 195.

123. Sano, M.; Kamino, A.; Okamura, J.; Shinkai, S. *Langmuir* **2001,** 17, 5125.

124. Pompeo, F.; Resasco, D. E. *Nano Lett.* **2002,** 2, 369.

125. Basiuk, E. V., et al. *J. Phys. Chem. B* **2002,** 106, 1588.

Chapter 2. Organometallic Chemistry of SWNT Films

2.1 Introduction

The interaction of metals with the benzenoid surfaces of carbon nanotubes and graphene can significantly modify their electronic and magnetic structure and plays an important role in the realization of electrical contacts to carbon-based electronic devices.[1] Depending on the nature of the metal atoms, their interaction with graphene surfaces is described by three distinct behaviors: (a) weak physisorption, (b) chemisorption with ionic character (doping) and little rehybridization, and (c) chemisorption with covalent bonding, in which there is minimal charge transfer but strong rehybridization of the carbon atoms from sp^2 to sp^3.[2, 3] We refer to this third category as destructive rehybridization as it usually leads to a loss of conductivity and a reduction in mobility of the graphene nanostructures. Recently, we suggested a fourth category: (d) chemisorption in which the covalent interaction leads to the formation of an electronically conjugating, organometallic bis-hexahapto-graphene junction while maintaining the electronic structure of the individual graphene nanostructures; such bonds involve minimal (structural) rehybridization and we have referred to this process as constructive rehybridization.[4]

The extended, periodic π-electron graphitic structures are narrow or zero band gap materials and thus the electron-donor and electron-acceptor interactions between the highest occupied molecular orbitals (HOMOs) and

lowest unoccupied molecular orbitals (LUMOs) of the arene π-system, and the d-orbitals of transition metals in hexa-hapto-metal bonds are strongly enhanced by the high lying valence band and low lying conduction band of the graphitic surfaces.[4, 5] In analogy with benzene, in which the e_{1g} and e_{2g} π-orbitals hybridize with the metal d-orbitals to form the hexahapto-metal-bonds in (η^6-benzene)$_2$Cr, the electronic structure of the graphitic π-electron systems is ideally suited for the realization of organometallic chemistry.[4, 6]

Single walled carbon nanotube (SWNT) networks offer a unique platform to study the effect of the hexahapto-metal bond on the establishment of electrical contact between graphitic surfaces. The electrical resistance of thin films of SWNTs is known to be dominated by the inter-nanotube junctions,[7] as confirmed in conductive tip atomic force microscopy[8-11] and cross junction electrical resistance studies.[12, 13] Because the current flows easily along the nanotubes before being forced to surmount the inter-nanotube junction resistance it is apparent that the percolation in these films is dominated by the nature of the inter-nanotube contacts. Thus the transport in such SWNT films – particularly in the vicinity of the percolation threshold – would be particularly sensitive to the formation of (η^6-SWNT)M(η^6-SWNT) interconnects because in this regime the conducting pathways become severely limited by the low density of SWNTs. The use of transition metals to interconnect SWNT surfaces represents the first attempt to use covalent bonding to modulate the conductivity of SWNT thin film

networks; prior to this work, the covalent functionalization of graphene and SWNT surfaces has led to a decrease in the conductivity and mobility.[14, 15] Previous approaches to improve the conductivity of SWNT thin film networks have relied on an increase in the carrier concentration by use of electrochemical and solid state gating or by exposure to dopants, which lead to ionic charge transfer chemistry and thus we rely on this latter technique to benchmark our use of hexahapto-metal SWNT interconnects.

The SWNT thin film networks are of interest in their own right and have been shown to provide a readily accessible platform for device applications, including their use as diodes and transistors,[16, 17], chemical and biosensors,[18-20] and near-IR detectors,[21-23]. The p-type semiconducting behavior of the SWNT thin films in conjunction with their optical transparency makes them suitable for transparent conductive coatings in large area solar cells, light emitting diodes and displays,[7, 16, 24-29] and as reconfigurable optical media.[30]

In the present section we report the effect of the deposition of suitably chosen metals on the conductivities of metallic (MT-), semiconducting (SC-), and unseparated SWNT films of nominal thickness (t), t = 0.5, 1, 2, 4, 8 nm. As we show below, these thicknesses approach the critical thickness (t_c) for percolation and offer an ideal platform with which to benchmark the ability of the covalent (η^6-SWNT)M(η^6-SWNT) bond to enhance the connectivity of a SWNT network. We chose metals to represent three of the limiting cases discussed above: (a)

physisorption (gold), (b) chemisorption with ionic doping (lithium), and (d) chemisorption with bis-hexahapto-bonding (constructive rehybridization, chromium).[4, 31] The experiments follow the e-beam version of the metal vapor synthesis (MVS) technique, which has proved to be very successful in the low temperature preparation of many bis-hexahapto-metal complexes,[32-34] although our substrates are held near room temperature.

2.2 Experimental

Preparation of SWNTs films

Aqueous dispersions of semiconducting (SC) and metallic SWNTs (MT) (IsoNanotubes (99%)) were obtained from NanoIntegris Inc. Unseparated tubes (P2) are from Carbon Solutions, Inc. For the metal deposition and conductivity measurements, SWNT films of predetermined effective thickness were prepared on alumina membranes by filtration; the requisite amount of 0.01 mg/ml SWNT dispersions were diluted with 50 mL of water, and the resulting mixture filtered through the alumina membrane (Anodisc 47, 0.02 μm, 47 mm diameter) and washed with DI water and ethanol to remove surfactants from the SWNTs. The effective film thickness was estimated using a SWNT density of 1.2 g/cm^3. The SWNT films on the alumina membranes were diced into 4 mm $\times$ 3 mm substrates and positioned on glass slides with pre-patterned gold electrodes. The finished devices were annealed at 300 ^{0}C for 3 h at a vacuum of 10^{-7} Torr to remove solvents.

For the spectroscopic studies, the SWNT films were prepared by filtration as described above using a nitrocellulose membrane (Millipore, 0.1 μm VCWP) and then transferred to the desired substrates. For the transfer a diced piece of the membrane with the SWNT film was placed on the substrate of choice (Au or HOPG for X-ray photoemission spectroscopy [XPS] and ultraviolet photoemission spectroscopy [UPS]). The substrates with the SWNT film on the membrane were held in an acetone bath for 1 hour to remove the cellulose membrane and then exposed to isopropanol vapors for 30 min.

Metal deposition

The Li, Cr, Au and Al deposition sources were obtained from Kurt Lesker. A customized cryo-pumped Temescal BJD 1800 e-beam evaporator operating at a base pressure of 10^{-6} Torr was used for the metal deposition experiments which were conducted at an evaporation rate of 0.01 nm/s.

Measurements and Characterization

The electrical measurements as a function of metal deposition were conducted with a custom-built feed-through assembly mounted in the e-beam chamber which was interfaced to a multiplexed Keithley 2700 data acquisition system that allowed the simultaneous collection of six channels of resistance data thereby providing a direct comparison of the transport properties of films of different thickness.

The SEM study was conducted with a Nova NanoSEM 450 instrument (FEI Company) with an acceleration voltage of 12 kV.

The X-ray photoelectron spectroscopy (XPS) was performed using a Kratos AXIS ULTRADLD XPS system equipped with an Al Kα monochromated X-ray source, He UV source, and a 165-mm electron energy hemispherical analyzer. The vacuum pressure was kept below 3×10^{-9} torr and a charge neutralizer was applied during the data acquisition. The slot size for the XPS is 300 × 700 μm and the UPS aperture has a diameter of 110 μm.

The survey XPS spectra were recorded at 270 kW with a step of 0.5 eV, dwell time of 100 ms and 80 pass energy. The high resolution scans were conducted at 300 kW with a step of 0.05 eV, dwell time 200 ms and pass energy (PE) of 20.

For the XPS and UPS measurements the SWNT films (1 nm, 4 nm and 50 nm thickness on Au and HOPG substrates, 1 cm x 1 cm), were annealed at 400ºC in a vacuum of 10^{-7} Torr for 4 hours. Cr deposition was performed by e-beam as described above and the samples quickly transferred to the XPS chamber to minimize the exposure to air.

2. 3 Results and discussion

Transport properties of pristine semiconducting single-walled carbon nanotube (SC-SWNT) thin films. Below we explore the use of metals in improving inter-nanotube junction resistance and we report the results of high vacuum metal deposition experiments conducted on ultrathin SWNT networks in the vicinity of the percolating threshold. The pristine films were annealed at 300ºC for 3 hour in a vacuum of 10^{-7} Torr before transfer to a cryo-pumped

Temescal BJD 1800 e-beam evaporator equipped with custom fittings to allow the measurement of the *in situ* film resistance**,** where they were further annealed at 110ºC to minimize atmospheric p-type doping;[35] The electrical conductivities were measured in a 2-probe configuration as 4-probe measurements showed a negligible contribution of the current contacts to the film resistance.

The SEM images in Fig. 2.1 show the emergence of network inhomogeneities in the thinnest films as evidenced by the appearance of spatial fluctuations in the density of SWNTs and is readily observed by comparing the uniformity of the films of effective thickness 0.5 nm (Fig.2.1 a,e) and 8 nm (Fig.2.1 d, f), in agreement with literature reports.[27, 36, 37]

The conductivity of the pristine SC-SWNT films at 300 K as a function of thickness is shown in Fig. 2.1g; the film of thickness t = 0.5 nm has a measured resistance of $R = 4 \times 10^{11}$ ohm and a conductivity $\sigma = 8 \times 10^{-5}$ S/cm. The conductivity of the pristine SC-SWNT films shows a pronounced increase between t = 0.5 nm and 2 nm, beyond which it saturates at a bulk conductivity, σ ~ 1 S/cm.

The strong dependence of conductivity on film thickness agrees with expectations based on percolation theory,[38, 39] and as shown in Fig. 2.1g (inset) can be satisfactorily described by the expression: $\sigma \propto (t - t_c)^{\alpha}$, with an estimated percolation threshold, t_c ~ 0.4 nm for the SC-SWNT films and critical exponent α = 2.4 in good agreement with the value of t_c = 1 – 3 nm previously obtained for thin films of non-separated SWNTs.[27, 40, 41] In order to test the

reproducibility of the data, a second set of independently prepared SWNT films was evaluated and found to give similar results (t_c ~ 0.45 nm and α = 2.2).

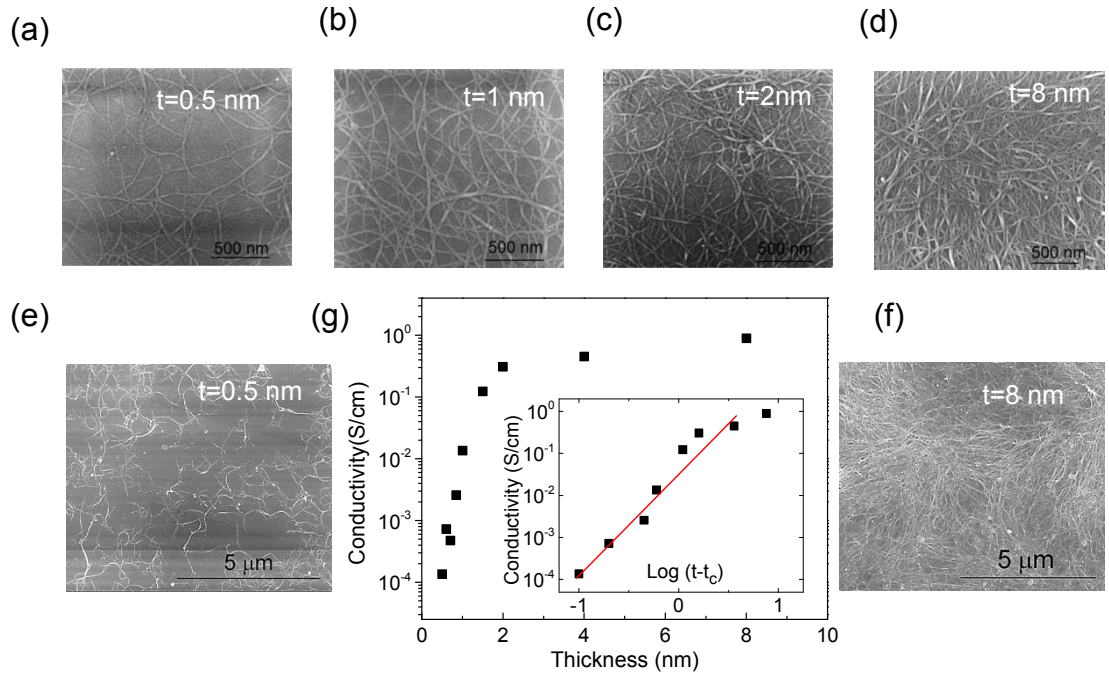

Figure 2.1 Conductivities of pristine SC-SWNT films. SEM images of SC-SWNT films of thicknesses (a, e) 0.5 nm; (b) 1 nm; (c) 2 nm; and (d, f) 8 nm. (g) Room temperature conductivity of pristine SC-SWNT films as a function of effective thickness. Inset of (g) shows a fit of conductivity data to $\sigma \propto (t - t_c)^{\alpha}$ with parameters t_c ~ 0.4 nm and α = 2.4

The critical thickness obtained from the percolation analysis is subject to two extrinsic factors: (a) the tendency of the SWNTs to rebundle during film

preparation, thereby reducing the number of conducting pathways available for electrical transport and, (b) the inhomogeneity of the SWNT network in very thin films which requires the percolating pathways to include the sparsely covered areas surrounding high density islands (Fig. 2.1e). The values of α obtained in this study exceed the universal critical exponents for 2D and 3D percolating systems of 1.33, and 1.94,[38] although critical exponents above the universal values were previously reported for SWNT networks[27, 41, 42] and composite system[39] and predicted theoretically for systems with a wide distribution of bond or junction resistances.[39, 43, 44]

Metal Deposition on SC-SWNT Thin Films. The behavior of the SC-SWNT conductivity on the deposition of one monolayer (ML) of metal is shown in Fig. 2.2 as a function of the SWNT film thickness. The SC-SWNT thin films show a strong increase in conductivity on deposition of alkali and transition metals, while the deposition of gold leads to a very small, monotonic increase in conductivity (not visible in Fig. 2.2), which is consistent with the formation of a parallel non-interacting film due to the fact that gold is unable to participate in bis-hexahapto-bonding owing to its filled outer d-orbital [physisorption, (a)].[4]

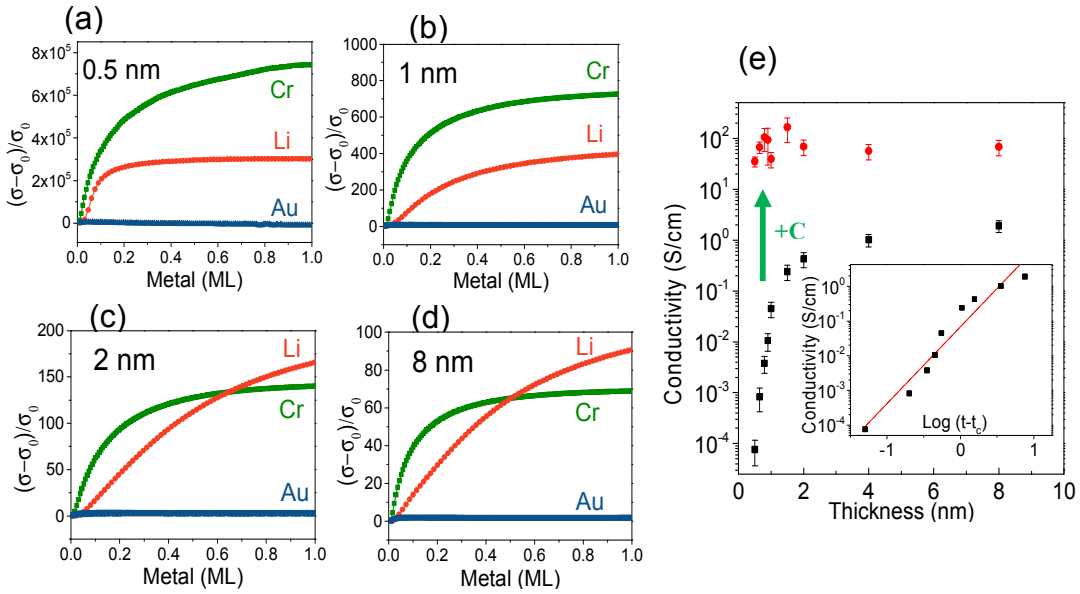

Figure 2.2 Effect of atomic interconnects on the conductivities of SC-SWNT films. Effect of metal deposition on the electrical conductivity of films of SC-SWNTs (a-d) of thicknesses: (a) 0.5 nm; (b) 1 nm; (c) 2 nm and (d) 8 nm. (e) Conductivities of SC-SWNT films before (black square symbols) and after (red circle symbol) 0.1 ML Cr deposition. Inset of (e) shows a fit of the conductivity data to $\sigma \propto (t - t_c)^{\alpha}$ with parameters t_c ~ 0.45 nm and α = 2.2.

The deposition of lithium is expected to result in charge transfer to the SWNTs [case (b) above, ionic chemisorption, doping], and alkali metals are known to produce a strong increase in the conductivity of carbon nanomaterials.[45-47]

Recently, we found that Cr can form (η^6-SWNT)M(η^6-SWNT) interconnects,[31, 48] and we have suggested that this mode of interaction with the graphene surfaces of carbon nanomaterials is totally distinct from ionic chemisorption and physisorption. The formation of (η^6-SWNT)Cr(η^6-SWNT) complexes is particularly favorable (Figure 2.3), because the distance between the benzene rings in the prototypical bis(benzene)chromium complex, (η^6-$C_6H_6)_2Cr$ (3.23 Å),[49] is close to the van der Waals gap of 3.15 Å within SWNT bundles.[50] The 6 valence electrons from the Cr atom in conjugation with two Clar sextets from the graphene surface[4] of the SWNTs lead to a total of 18 electrons which exactly fill the 3d4s4p metal valence shell and it is known to lead to a stable electronic configuration.[31, 51]

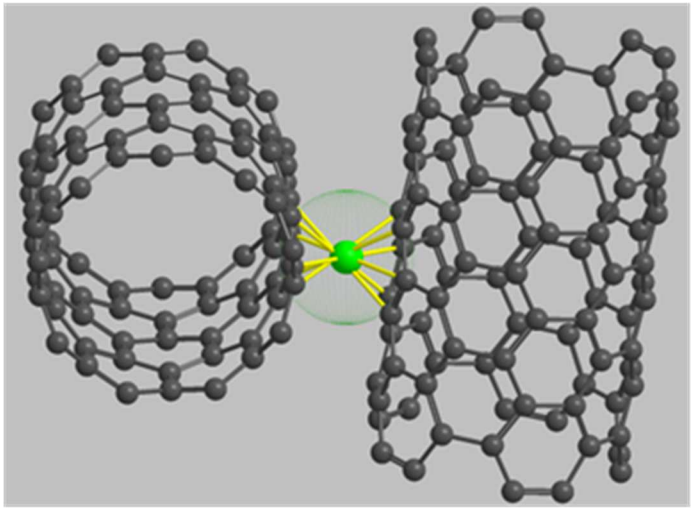

Figure 2.3 Formation of (η^6-SWNT)Cr(η^6-SWNT) bonds between the benzene rings of adjacent SWNTs.

Reference to Fig. 2.2 shows that in the initial stage of metal deposition (t_M < 0.5 ML) on SC-SWNT films, the conductivity enhancement induced by the Cr atoms is more efficient than the doping by Li and thus at very low coverage the ability of Cr to bridge the highly resistive SWNT contacts is always more effective than electron transfer via doping to the conduction band of SC-SWNTs. Beyond this point we distinguish between two cases: pristine SC-SWNT films which have reached the saturation conductivity (Fig. 2.2, $t_{SWNT} \geq 2$ nm), and pristine SC-SWNT films below this thickness (which are approaching t_c: $t_{SWNT} \leq 1$ nm). For those pristine SC-SWNT thin films beyond the saturation conductivity ($t_{SWNT} \geq 2$ nm), Li doping eventually becomes more effective in its ability to enhance the bulk SC-SWNT film conductivity. In the situation where the SC-SWNT film

approaches the percolation threshold ($t_{SWNT} \leq 1$ nm), it may be seen that Cr is always more effective than Li in enhancing the conductivity of the SC-SWNT network and this is in accord with a situation in which the conductivity is severely limited by the number of conducting pathways. At these thicknesses the SC-SWNT film conductivities are extremely dependent on the quality of the network junctions and the conductivity enhancements by the Cr atoms are about a factor of 700 (t = 1 nm) and 700,000 (t = 0.5 nm), clearly indicating that these films are in the vicinity of the critical thickness for percolation (t_c). In such sparse inhomogeneous network in the vicinity of percolation threshold turning on a very few intertube junctions by bis-hexahapto-bond formation can open new conducting pathways and dramatically increase the conductance of the film up to 5-6 orders of magnitude as can be seen in Fig.2.2a. After Cr deposition all of the SC-SWNT film conductivities are found to be independent of thickness which suggests that the formation of (η^6-SWNT)Cr(η^6-SWNT) bonds is able to completely remedy the weak links in the SWNT network to the point that percolation effects are no longer apparent in the data (Fig. 2.2e).

Metal Deposition on MT-SWNT Thin Films SEM images of networks of MT-SWNTs of effective thicknesses 0.5 – 8 nm are presented in Fig. 2.4 (a-d) together with the dependence of the electrical conductivity on the film thickness, which indicates a percolation threshold below a film thickness of 0.5 nm.

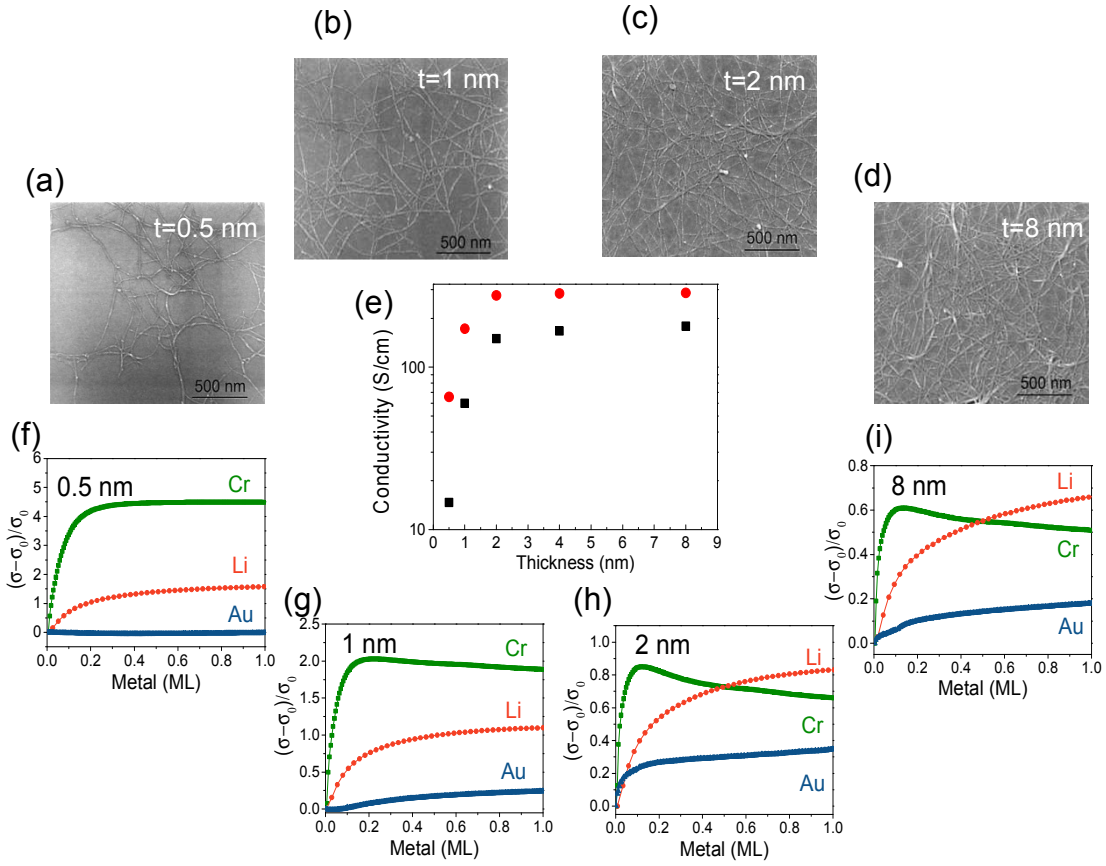

Figure 2.4 Effect of atomic interconnects on the conductivities of MT-SWNT films. SEM images of MT-SWNTs films (a-d) of thicknesses: (a) 0.5 nm; (b) 1 nm; (c) 2 nm; and (d) 8 nm. (e) Conductivities of MT-SWNT films before and after Cr deposition. Effect of metal deposition on electrical conductivity of MT-SWNTs films (f-i) of thicknesses: (f) 0.5 nm; (g) 1 nm; (h) 2 nm and (i) 8 nm.

For the thinnest measured MT-SWNT film (t = 0.5 nm), the room temperature resistance was R = 2.3×10^6 ohm (σ = 15 S/cm) which is 5 orders of magnitude lower than the value measured for a SC-SWNT film of the same thickness (above). Despite this difference in the film resistances, the saturation values of the conductivities occur in the same range of thicknesses (2-8 nm) for SC- and M-SWNTs; this result emphasizes the importance of the density of physical SWNT junctions in these films and number of conducting pathways rather than the absolute conductivities.

The behavior of the MT-SWNTs film conductivities on the deposition of gold (Fig. 2.4) is similar to that seen for the SC-SWNTs although this change is not visible in the results shown in Fig. 2.2.

The qualitative features of the response of the MT-SWNT films to the deposition of Li and Cr resemble that of the SC-SWNT films, although the magnitude of the response is two to four orders of magnitude less. In all cases, the deposition of about 0.1 ML Cr leads to an abrupt increase in the conductivity of the MT-SWNT films; for the pristine films, which have reached the saturation conductivity (Fig. 2.4h, $t_{SWNT} \geq 2$ nm), Li doping becomes more effective in its ability of enhance the MT-SWNT film conductivity at $t_M > \sim 0.5$ML. For the pristine MT-SWNT films, which are below the saturation conductivity ($t_{SWNT} \leq 1$ nm), Cr is always more effective than Li in enhancing the conductivity of the SWNT networks. In most of the films shown in Fig. 2.4, it may be seen that Cr metal deposition beyond about 0.1 ML leads to a slow decrease in the film

conductivities, which we attribute to hybridization of the Cr atom with the SWNT metallic states along the body of the SWNTs which act to weakly scatter the conduction electrons [chemisorption, (c); destructive rehybridization, see above]. This result emphasizes the very small number of Cr atoms that are actually involved in bridging the SWNT-SWNT junctions and in constructing conducting pathways.

Although the conductivities of the SC-SWNTs (Fig. 2.2 a-d) and the MT-SWNTs (Fig. 2.4 f-i) differ by many orders of magnitude, their response to ionic doping and to covalent bond formation are identical in the sense that Cr is always more effective below the saturation conductivity of the pristine films (Fig. 2.2a and 2.4f, $t_{SWNT} \leq 1$ nm). This is to be expected as above this thickness the conductivities of the pristine films are invariant to further increases in thickness, because the physical junction density has reached the bulk value.

Fig. 2.5 shows the important role of the (η^6-SWNT)Cr(η^6-SWNT) junctions in modulating the conductivity of SWNT films in the vicinity of the percolation threshold and highlights the differences in the magnitude of the response of SC-SWNT and MT-SWNT films to this phenomenon. The results clearly demonstrate that covalent bonding, in the form of the organometallic bis-hexahapto-bond (Fig. 2.3), offers an interesting alternative to the standard approach, whereby the carrier concentration of the SWNT film is increased by chemical doping or gating.[52-54] The effect of 0.1 ML Cr on an extended set of SC films is shown in Fig. 2.6.

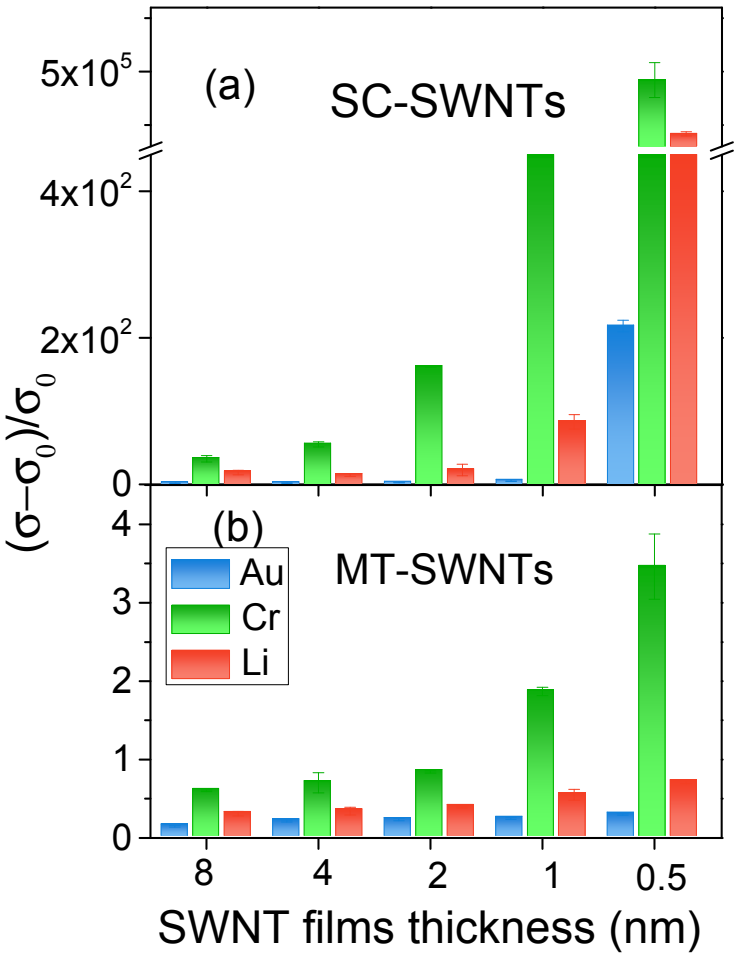

Figure 2.5 Conductivity enhancements at 0.1monolayer of deposited metal for semiconducting (a) and metallic (b) SWNT films.

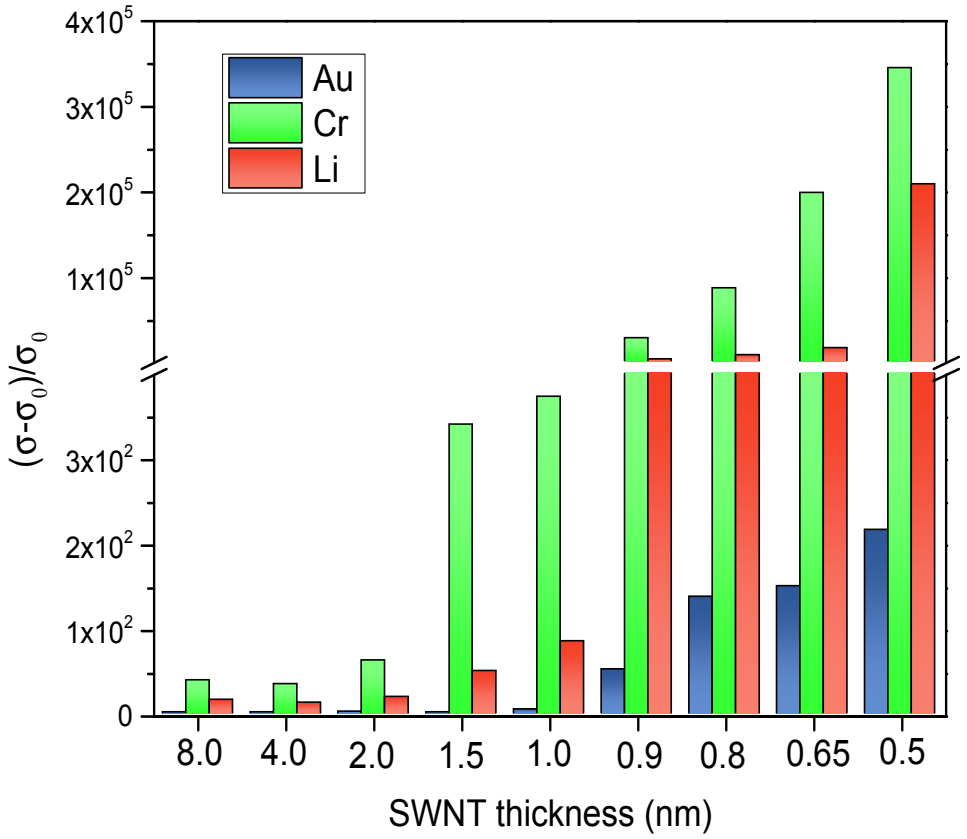

Figure 2.6 Conductivity enhancements on metal deposition (0.1ML), for an extended set of semiconducting SWNT films.

Metal Deposition on Unseparated P2-SWNT Thin Films We followed the same procedure to explore the effect of Cr deposition on unseparated SWNTs (P2-SWNT) films. Figure 2.7 shows SEM images of P2-SWNT films with a thickness of 2nm to 16nm. The SWNTs have larger bundles compared with the separated SC-SWNTs and MT-SWNTs. The 2nm film is in the vicinity of the critical thickness for the percolation threshold (Fig. 2.7a), and there is a gradual increase in conductivity up to a thickness of about 10 nm; thus the percolation threshold of the P2-SWNT films occurs at greater film thicknesses than the SC- and MT-SWNTs due to the larger bundle size. When Cr is deposited, the conductivities of these films increase dramatically on deposition of a small amount of Cr (0~0.2 ML); overall the behavior is similar to that seen for the separated SWNT films but shifted to larger thicknesses due to the enhanced bundling (compare with Fig 2.5 and 2.7).

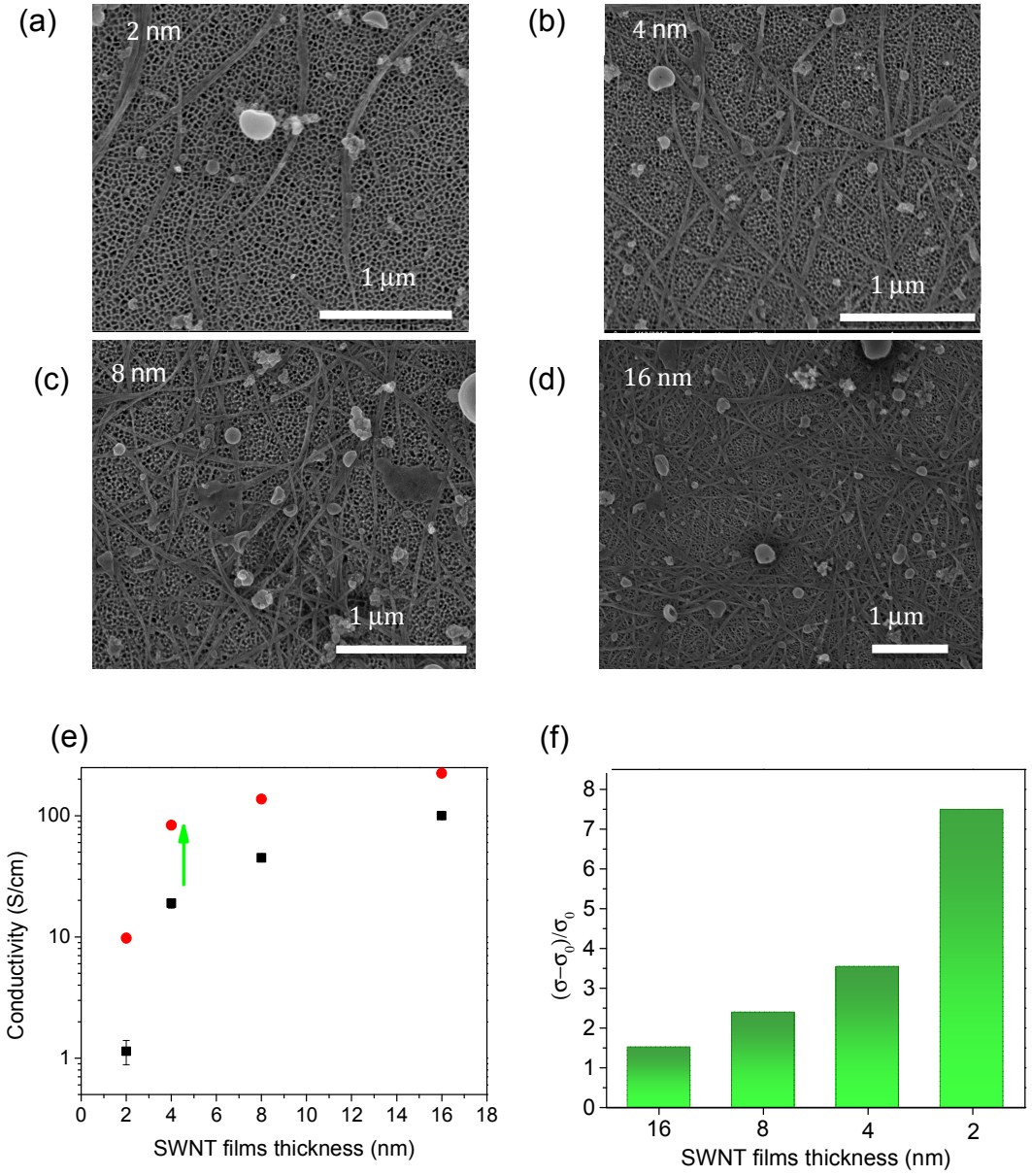

Figure 2.7 SEM images of P2-SWNTs with thickness of (a) 2nm, (b) 4nm, (c) 8nm, and (d) 16 nm. (e) Conductivity of P2 films before and after 0.1 monolayer of deposited Cr. (f) Conductivity enhancements at 0.1 monolayer of deposited Cr.

Spectroscopic Studies of the Metal-SWNT Thin Films.

The effect of chromium on the electronic structure of SC-SWNTs was further examined with ultraviolet photoelectron spectroscopy (UPS) and Fig. 2.8a shows the valence band spectra of a SC-SWNT film before and after the deposition of 1 nm Cr. The spectrum of pristine SC-SWNTs is very similar to that of HOPG (Fig. 2.9) with a band at around 3 eV assigned to the 2p-π states and broad overlapping bands at ~ 5 eV and 8 eV associated with the 2p-σ states. The SC-SWNT film with deposited Cr (1 nm, e-beam) initially exhibited a spectrum very similar to the pristine films presumably due to the chromium oxidation that occurs upon air exposure during transfer from the e-beam to the XPS chamber and this interpretation is supported by the core Cr2p spectrum (Fig. 2.8c) which shows that the majority of the surface Cr is present in oxide form. To remove oxygen from the surface, the sample was sputter etched with an Ar^+ beam for 10 s; this resulted in the development of a well-defined peak at ~ 2.4 eV, accompanied by a shoulder at ~3.5 eV(Fig. 2.8a). Increasing the sputtering time to 30 s did not change the position of the peak but led to a slight increase of the density of state (DOS) near the Fermi energy (E_F). The high DOS at the Fermi edge suggests that part of the surface chromium retains its metallic nature; the formation of small Cr clusters has been observed in (η^6-SWNT)$Cr_x(CO)_y$ synthesized in solution[55] and on e-beam deposition on graphene.[56]

A comparison of the photoemission spectrum of Cr/SCSWNT with that of Cr film (prepared by e-beam deposition, sputtered with Ar+ beam for 10 s to remove surface contamination prior to the measurement) is shown in Figure 2.8a. In our experiments, the Cr 3d states of the Cr film give a broad peak centered at ~1.9 eV, and thus, the peak at 2.4 eV in the Cr/SC-SWNT is related to the complexation of chromium atoms with the benzenoid ring system of the carbon nanotube surface. This agrees with previous reports, in which the d-states in metal clusters have been shown to shift to higher binding energies due to rehybridization with the graphite π*-states.[57] The SWNT C 1s core level spectra (Figure 2.8b) broaden after the deposition of Cr in agreement with previous studies on the interaction of low coverages of Cr with C60 films[58] as a result of the hybridization of the Cr dπ orbitals with the SWNT carbon π-orbitals.

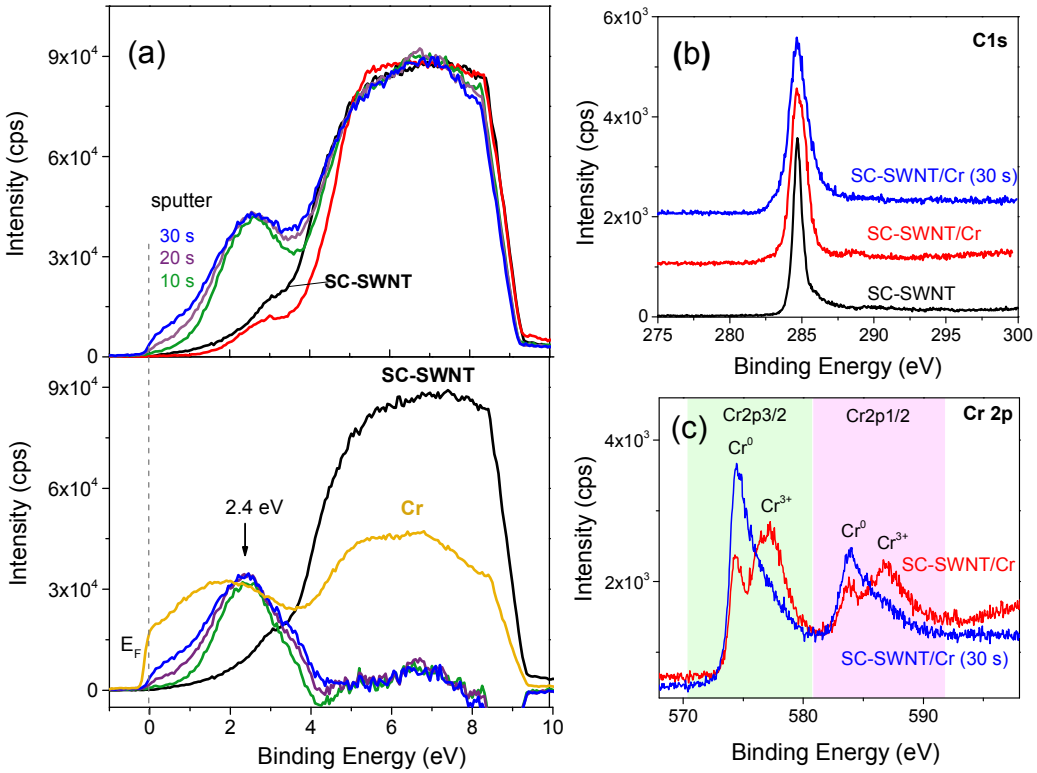

Figure 2.8 Photoelectron spectra in the ultraviolet (UPS, He I) and X-ray (XPS) regimes for a SC-SWNT film (50 nm film on a HOPG substrate), before and after e-beam deposition of 1 nm Cr. (a) UPS spectra of SC-SWNT (black line), SC-SWNT with 1 nm Cr (SC-SWNT/Cr, red), and SC-SWNT/Cr after sputtering for 10 s (green), 20 s (purple) and 30 s (blue); all spectra are normalized to the 2p-σ transitions at 6-7 eV. The bottom panel shows the difference spectra of the sputtered Cr/SC-SWNT sample obtained after subtraction of the SC-SWNT contribution. (b) Normalized C1s XPS spectra of SC-SWNT, SC-SWNT/Cr and 30 s sputtered SC-SWNT/Cr. (c) Normalized Cr2p XPS spectra of SC-SWNT, SC-SWNT/Cr and 30 s sputtered SC-SWNT/Cr.

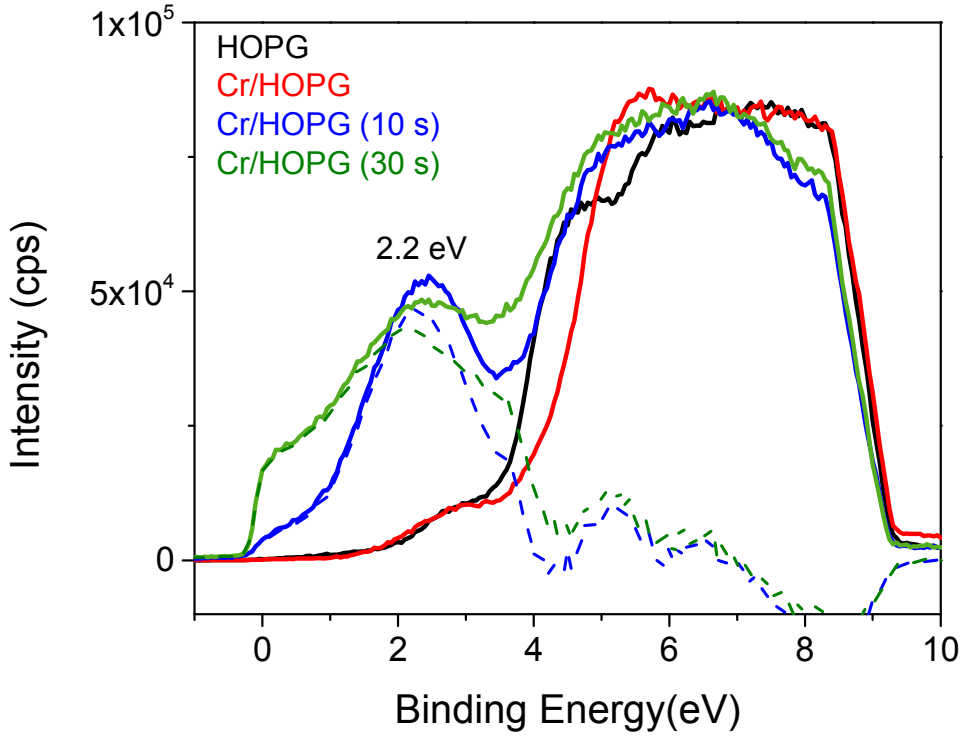

Figure 2.9 Ultraviolet photoemission spectra (UPS, He I) of HOPG before and after e-beam deposition of 1 nm Cr; the spectra are normalized to the 2p-σ transitions at ~7 eV. HOPG (black line) shows a band at around 3 eV assigned to the 2p-π states and broad overlapping bands at ~ 5 eV and 8 eV associated with 2p-σ states. Cr/HOPG (red line) exhibits similar spectrum to HOPG due to the oxidation of chromium during exposure to air. The sample was sputtered with Ar^+ to remove the top oxide layer and the evolution of UPS spectra after 10 s sputtering (blue line) and 30 s sputtering (green line) is illustrated. Dashed lines show the difference spectra obtained by subtracting the spectrum of HOPG.

This variant of covalent chemistry also contrasts with the standard carbon-carbon bond forming reactions where the graphene surface carbon atoms undergo full rehybridization from sp^2 to sp^3 and in which the pyramidalization angle formally changes from $\theta_P = 0^o$ to $\theta_P = 19.5^o$.[4, 59, 60] It is important to note that the hexahapto-metal bond forms with very little *structural rehybridization* – even in the case of bis(benzene)chromium, where the attached atoms are unconstrained, the pyramidalization angle only reaches $\theta_P = 1.7^o$.[4, 49] In situations where the complexed carbon atoms are incorporated in a graphene surface the structural rehybridization will be even less due to the geometrical constraints of the lattice. While it is well known that the graphene carbon atoms strongly hybridize with some transition metals, in hexahapto-coordination this electronic conjugation is able to function without marked structural rehybridization (pyramidalization).[3] The absence of structural rehybridization in bis-hexahapto-metal organometallic complexes also explains why this bond is likely the only covalent bond that can be successful in the electronic conjugation of graphene surfaces: if there is strong structural rehybridization of the reacting graphene carbon atoms, the one-center 2s, 2p orbital hybrids remain orthogonal, σ–π separation is maintained, and conjugation is minimized.[61] The bis-hexahapto-metal bond, which involves 12 carbon atoms coordinated with one metal atom, is highly delocalized and does not dominate the bonding of any single carbon atom and thus the individual carbon atoms maintain their conjugation with the graphene sheet - the metal d-orbitals and the carbon π-orbitals are non-

orthogonal, overlap effectively and thereby seamlessly conjugate the two graphene sheets.

2.4 Conclusion

In summary, we demonstrated the important role of the covalent hexahapto (η^6) bond formed by chromium atoms and the benzenoid rings of carbon nanotubes. The deposition of sub-monolayer of chromium on SWNT networks significantly increases the film conductivity as a result of reduced inter-nanotube junction resistance. Raman and NIR spectroscopies indicate that the interaction between the transition metal and SWNT does not induce significant charge transfer, thereby supporting the covalent nature of the bond in agreement with the valence band structure seen in the UPS experiments.

References

1. Banerjee, S.; Hemraj-Benny, T.; Wong, S. S. *Adv. Mater.* **2005,** 17, 17.
2. Chan, K. T.; Neaton, J. B.; Cohen, M. L. *Phys. Rev. B* **2008,** 77, 235430.
3. Liu, X., et al. *Crystals* **2013,** 3, 79.
4. Bekyarova, E., et al. *Acc. Chem. Res.* **2013,** 46, 65.
5. Sarkar, S.; Bekyarova, E.; Haddon, R. C. *Acc. Chem. Res.* **2012,** 45, 673.
6. Sarkar, S.; Niyogi, S.; Bekyarova, E.; Haddon, R. C. *Chem. Sci.* **2011,** 2, 1326.
7. Hu, L. B.; Hecht, D. S.; Gruner, G. *Chem. Rev.* **2010,** 110, 5790.
8. Nirmalraj, P. N.; Lyons, P. E.; De, S.; Coleman, J. N.; Boland, J. J. *Nano Lett.* **2009,** 9, 3890.
9. Topinka, M. A., et al. *Nano Lett.* **2009,** 9, 1866.
10. Lee, E. J. H.; Balasubramanian, K.; Burghard, M.; Kern, K. *Adv. Mater.* **2009,** 21, 2720.
11. Znidarsic, A., et al. *J. Phys. Chem. C* **2013,** 117, 13324.
12. Fuhrer, M. S., et al. *Science* **2000,** 288, 494.
13. Kim, D.; Huang, J.; Shin, H. K.; Roy, S.; Choi, W. *Nano Lett.* **2006,** 6, 2821.
14. Zhang, H., et al. *Nano Lett.* **2011,** 11, 4047.
15. Sarkar, S., et al. *Adv. Mater.* **2013,** 25, 1131.
16. Gruner, G. *J. Mater. Chem.* **2006,** 16, 3533.
17. Kang, S. J., et al. *Nature Nanotech.* **2007,** 2, 230.

18. Bekyarova, E., et al. *J. Biomed. Nanotech.* **2005,** 1, 3.

19. Snow, E. S.; Perkins, F. K.; Houser, E. J.; Badescu, S. C.; Reinecke, T. L. *Science* **2005,** 307, 1942.

20. Ding, M. N.; Tang, Y. F.; Gou, P. P.; Reber, M. J.; Star, A. *Adv. Mater.* **2011,** 23, 536.

21. Itkis, M. E.; Borondics, F.; Yu, A.; Haddon, R. C. *Science* **2006,** 312, 413.

22. Lu, R. T.; Li, Z. Z.; Xu, G. W.; Wu, J. Z. *Appl. Phys. Lett.* **2009,** 94, 163110.

23. St-Antoine, B. C.; Menard, D.; Martel, R. *Nano Lett.* **2011,** 11, 609.

24. Wu, Z., et al. *Science* **2004,** 305, 1273.

25. Kaempgen, M.; Duesberg, G. S.; Roth, S. *Appl. Surf. Sci.* **2005,** 252, 425.

26. Zhang, D., et al. *Nano Lett.* **2006,** 6, 1880.

27. De, S.; King, P. J.; Lyons, P. E.; Khan, U.; Coleman, J. N. *ACS Nano* **2010,** 4, 7064.

28. McCarthy, M. A., et al. *Science* **2011,** 332, 570.

29. Gwinner, M. C.; Jakubka, F.; Gannot, F.; Sirringhaus, H.; Zaumseil, J. *ACS Nano* **2012,** 6, 539.

30. Wang, F.; Itkis, M. E.; Bekyarova, E.; Haddon, R. C. *Nature Photon.* **2013,** 7, 459.

31. Wang, F., et al. *Appl. Phys. Lett.* **2012,** 100, 223111.

32. Timms, P. L. *Chem. Commun.* **1969,** 1033.

33. Cloke, F. G. N. *Chem. Soc. Rev.* **1993,** 17.

34. Arnold, P. A., et al. *J. Organometal. Chem.* **2003,** 688, 49.

35. Collins, P. G.; Bradley, K.; Ishigami, M.; Zettl, A. *Science* **2000,** 287, 1801.

36. Doherty, E. M., et al. *Carbon* **2009,** 47, 2466.

37. Scardaci, V.; Coull, R.; Coleman, J. N. *App. Phys. Lett.* **2010,** 97, 023114.

38. Stauffer, D., *Introduction to Percolation Theory*. Taylor & Francis: London and Philadelphia, 1985.

39. Balberg, I.; Azulay, D.; Toker, D.; Millo, O. *Int. J. Mod. Phys. B* **2004,** 18, 2091.

40. Bekyarova, E., et al. *J. Am. Chem. Soc.* **2005,** 127, 5990.

41. Ural, A.; Behnam, A.; Johnson, J.; Choi, Y. *Proc. of SPIE* **2007,** 6769, 67690B.

42. Bauhofer, W.; Kovacs, J. Z. *Comp. Sci.Tech.* **2009,** 69, 1486.

43. Kogut, P. M.; Straley, J. P. *J. Phys. C: Solid State Phys.* **1979,** 12, 1.

44. Balberg, I. *Phys. Rev. Lett.* **1987,** 59, 1305.

45. Dresselhaus, M. S.; Dresselhaus, G., Intercalation compounds of graphite. In *Advances in Physics*, Martin, D. H., Ed. Taylor & Francis Ltd: London, 1981; Vol. 30, pp 139.

46. Haddon, R. C. *Acc. Chem. Res.* **1992,** 25, 127.

47. Lee, R. S.; Kim, H. J.; Fischer, J. E.; Thess, A.; Smalley, R. E. *Nature* **1997,** 388, 255.

48. Wang, F., et al. *J. Phys. Org. Chem.* **2012,** 25, 607.

49. Haaland, A. *Acta Chem. Scand.* **1965,** 19, 4146.

50. Thess, A., et al. *Science* **1996,** 273, 483.

51. Elschenbroich, C., *Organometallics*. Third ed.; Wiley-VCH: Weinheim, 2006.

52. Avdoshenko, S. M.; Ioffe, I. N.; Cuniberti, G.; Dunsch, L.; Popov, A. A. *ACS Nano* **2011,** 5, 9939.

53. Li, E. Y.; Marzari, N. *ACS Nano* **2011,** 5, 9726.

54. Dai, J.; Zhao, Y.; Wu, X.; Zeng, X. C.; Yang, J. *J. Phys. Chem. C* **2013,** 117, 22156.

55. Kalinina, I., et al. *Fullerenes, Nanotubes and Carbon Nanostructures* **2014,** 22, 47.

56. Zan, R.; Bangert, U.; Ramasse, Q.; Novoselov, K. S. *Nano. Lett.* **2011,** 11, 1087.

57. Di Nardo, S., et al. *Surf. Sci.* **1994,** 307, 922.

58. Ohno, T. R., et al. *Phys. Rev. B* **1993,** 47, 2389.

59. Niyogi, S., et al. *Acc. Chem. Res.* **2002,** 35, 1105.

60. Hu, H., et al. *J. Am. Chem. Soc.* **2003,** 125, 14893.

61. Haddon, R. C. *Acc. Chem. Res.* **1988,** 21, 243.

Chapter 3. Optical and Electronic Properties of Graphene and Related Carbon Materials

3.1 Introduction

Two-dimensional carbon materials such as graphene, graphene oxide, and reduced graphene oxides continue to attract attention due to their promise as nanoelectronic components, transparent conductors, composites, thermal interface materials, energy storage systems and nano-bio hybrids [1-7].

Oxidation of graphite leads to the formation of graphene oxide (GO), a material that is processable in water and alcohols, and which has proven to be a viable starting point for a wide-range of applications. GO contains a range of oxygen functionalities and defects [8-10], and due to its excellent solubility it is widely employed as a graphene precursor.[8, 10, 11] Chemical reduction of graphene oxide (GO) is the most common technique for the regeneration of the graphene electronic structure.[12-15] The materials derived from this process (RGO), typically lack the high degree of perfection, which is required for an electronic material and do not exhibit high conductivities. In the last years significant efforts have been devoted to development of conductive transparent films based on solution processable GO, which afford uniform and controlled deposition of graphene-based thin films. In addition to chemical reduction, thermal annealing of GO films was found to be the most effective post-deposition treatment for improving the film conductivity.[16-21]

Reduced graphene oxide (RGO) often agglomerates because of its hydrophobic nature[12, 14, 22] unless stabilized in solution by additives such as polymers, surfactants, and bio-molecules. The controlled chemical modification of the graphene sheets can impart sufficient solubility to aid processability of the material and at the same time preserve its electronic, thermal and mechanical properties. In analogy with carbon nanotubes[23], covalent attachment of long-chain amines to the graphene sheets has proven to be a viable approach in this respect.[1, 24-28]

In this work we covalently modify graphene sheets with octadecylamine (ODA) to study their spectroscopic and electrical properties. We demonstrate that the direct reaction of GO with ODA in the presence of dicyclohexylcarbodiimide (DCC) is able to partially regenerate the π-conjugated electronic structure of graphene, while maintaining excellent solubility of the derived material (ODA-G1) in organic solvents. We suggest that the DCC/ODA reaction cleaves the epoxides, dehydrates the GO and converts the carboxylic acid groups to octadecylamide functional groups thereby extending the π-conjugation and conferring organic solubility. In addition we provide a benchmark analysis of the solution and solid state spectroscopy of representative soluble graphene derivatives and the conductivity properties of their thin films. The ODA-functionalized graphene materials exhibit moderate conductivities with partial regeneration of the π-conjugated structure, which is sufficient, and even beneficial, for certain applications.[29]

3.2 Experimental

Materials Natural graphite flakes (NG) with an average size of 300 μm were obtained from TIMCAL Graphite and Carbon. Potassium chlorate ($KClO_3$, FW = 138.55), sulfuric acid (H_2SO_4, 95-98%), nitric acid (HNO_3, 69.4%), octadecylamine (ODA, FW = 269.52, mp = 52^oC), *1,3*-dicyclohexylcarbodiimide (DCC, FW = 206.33, mp = 34-35 ^oC), hydrazine hydrate (FW= 50.05), and N,N-dimethylformamide(DMF, FW = 73.09) were obtained from Sigma-Aldrich.

Preparation of expanded graphite (XG) Nature graphite flakes (NG) 10g were mixed with sulfuric acid (90 mL) and nitric acid (30 mL) and kept at room temperature for 15h. The materials were then filtered and washed with water until the filtrate showed neutral pH, and then the solid material exfoliated by thermal shock treatment at 800^oC for 3 min[30].

Synthesis of graphene oxide (GO) The expanded graphite (XG) was oxidized to graphite oxide (GO) using a modified Staudenmaier method [31]; in a typical experiment, concentrated H_2SO_4 (35 mL) and fuming nitric acid (32 mL) were mixed in a flask placed in an ice bath, and XG (2g) was added to the mixture with stirring followed by slow addition of $KClO_3$ (22 g). The mixture was stirred overnight. The product was separated by filtration and washed with 5% HCl and DI water until the pH of the filtrate became neutral. The solid GO material was dried in an oven at 100^oC.

Synthesis of reduced graphene oxide (RGO) A reference reduced graphene oxide (RGO) material was synthesized by hydrazine reduction of

graphene oxide (GO). In a typical procedure, GO (100 mg) was dispersed in 100 mL of water by shear mixing for 15 min and sonication for 1h. The reduction was performed by adding hydrazine to the GO solution (weight ratio 7:10 of hydrazine:GO). The reaction was heated to 100 ^{o}C and stirred under argon for 1 day. The resulting solution was filtered (Millipore, Fluoropore, 0.2 μm) and the solid was washed with water and methanol and then dried in a dessicator.

Synthesis of ODA-G1 One route to the synthesis of octadecylamine functionalized graphene is using the coupling agent 1,3-dicyclohexylcarbo-diimide (DCC). The octadecylamine functionalized graphene (ODA-G1) was prepared from GO using a process, similar to that applied to single-walled carbon nanotubes (SWNTs) [32]. Thus, GO (100 mg) in anhydrous N,N-dimethylformamide (DMF, 100 mL) was shear mixed for 30 min and sonicated for 5 h to produce a homogeneous dispersion, which was transferred to a three-neck flask and purged with argon overnight while stirring at room temperature. 1,3-dicyclohexylcarbo-diimide (DCC, 1 g) was added to the solution and stirred for 30 min at room temperature, flowed by the addition of octadecylamine (ODA, 1 g). The mixture was heated and stirred under argon at 120 ^{o}C for 5 days, cooled to room temperature, filtered and washed with DMF and ethanol and the resulting product (ODA-G1) was dried at room temperature under vacuum in a desiccator.

Synthesis of ODA-G2 Another synthetic route for the ODA-functionalization of graphene employs thionyl chloride, using previously reported procedure.[1]. In a

typical experiment, , 120 mg GO was refluxed in 25mL $SOCl_2$ in the presence of 0.6mL DMF at 70°C for 24h, followed by distilling the excess $SOCl_2$. 525mg ODA was added at 120°C under Argon for 4 days. The product was washed with ethanol and dried in a dessicator.

Synthesis of dehydrated GO (Dehy-GO) The dehydration of GO as a result of the reaction with DCC was conducted as follows: 1g DCC was added into the GO dispersion in DMF. The reaction was kept at 120°C under Argon for 5 days. The reaction conditions are similar to those of ODA-G1 (above).

Preparation of thin films Thin films of expanded graphite (XG), oxidized XG (graphene oxide, GO), reduced graphene oxide (RGO) and octadecylamine functionalized graphene (ODA-G1) were prepared by dispersing 10 mg of material in 100 mL ethanol through shear mixing for 30 mins and sonication for 2 hours. The film was prepared by filtering through an alumina membrane (Whatman, Anodisc 47, 0.02 μm, 47 mm diameter).

Preparation of C_{60} samples for absorption spectroscopy

Solution of C_{60}: C_{60} (10mg) was dispersed in 250 mL of hexane by overnight stirring. An aliquot of the stock solution was diluted to obtain a sample with concentration of 0.01 mg/mL for spectroscopic measurements.

Film of C_{60}: Films were deposited on sapphire substrates by thermal evaporation of C_{60} in a vacuum of 10^{-6} torr. The film thickness was obtained from the height profile obtained by AFM measurements.

Characterization

The TGA measurements were performed at a heating rate of 5 °C/min in air using a Pyris 1 thermo-gravimetric analyzer (Perkin Elmer).

The UV-vis spectra of solutions and films were measured using a Varian Cary5000 UV-Vis-NIR spectrophotometer. Dispersions of the materials in tetrahydrofuran (THF) were prepared by high-shear mixing for 30 mins and 2 hours bath sonication for 2 hours. The solution-phase spectra were recorded in a quartz cell of 1 cm path length. The films were produced by filtering the solutions of 0.1 mg/ml through an alumina membrane (Whatman, Anodisc 47, 0.02 μm, 47 mm diameter).

The ATR-IR spectra were taken using a Thermo Nicolet Nexus 670 FTIR instrument, equipped with an ATR sampling accessory using a diamond crystal.

Raman spectra were acquired with a Nicolet Almega XR Dispersive Raman microscope using 532 nm laser excitation.

SEM images were collected with Nova NanoSEM 50 instrument (FEI Company) at accelerating voltage of 10 kV and average working distance of 5 mm.

For conductivity measurements the films were prepared by filtration in the same way as the films for spectroscopy; all films contained the same mass of material per unit area (1 mg/cm^2). The sheet resistance was measured in a van der Pauw geometry with Keithley 2400 and Keithley 236 electrometers.

3.3 Results and discussion

The GO in our study was synthesized from expanded natural graphite (XG) by the Staudenmaier method. Thermogravimetric analysis data of the starting material, XG, and the synthesized samples are shown in Figure 3.1. The TGA of pristine graphite shows that burning commences at around 800°C. For GO, the weight losses at around 100 °C and 200 °C are attributed to absorbed water and the presence of oxygen functional groups and there is a 40% weight loss in the GO sample between 200 and 300°C. After chemical reduction, the weight loss in the 200-300°C range decreases to 20%, indicating remaining functional groups. For ODA-G1, the 30% weight loss at 200-300°C is attributed to the elimination of the ODA and oxygen functional groups.

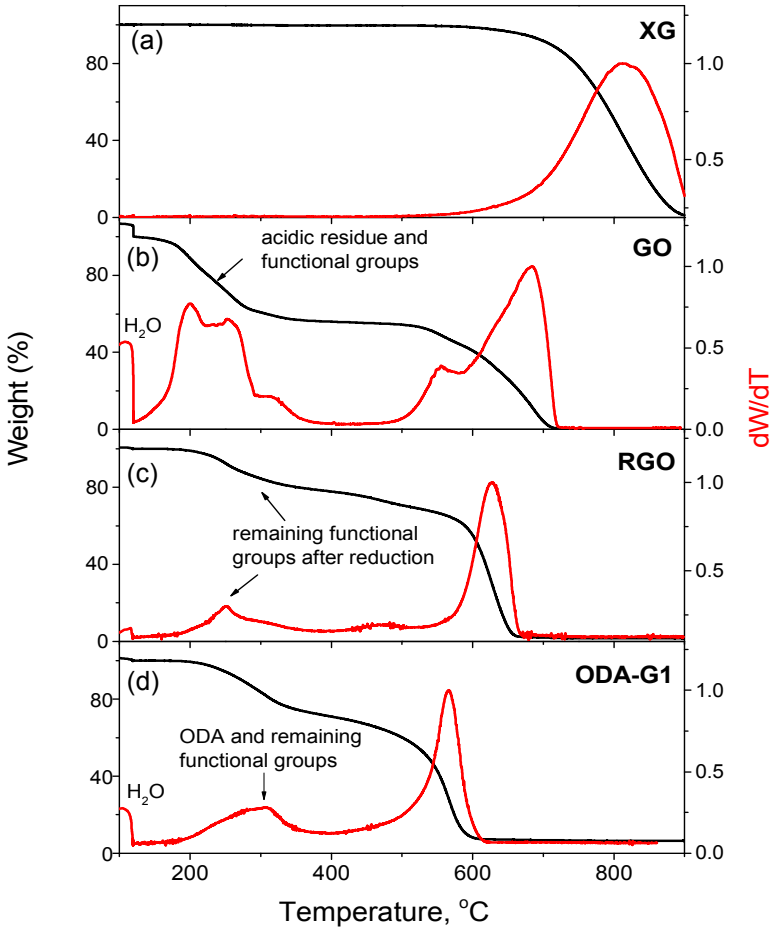

Figure 3.1 Thermogravimetric analysis (TGA) data (under dry air) of (a) expanded graphite (XG), (b) oxidized XG (GO), (c) reduced graphene oxide (RGO), and (d) octadecylamine functionalized graphene (ODA-G1).

Mid-infrared spectroscopy was used to analyze the chemical groups in the octadecylamine-functionalized graphene (ODA-G1) material and to quantitatively assess the amount of ODA attached to the graphene sheets. ATR spectra of the GO and ODA-G1 materials are illustrated in Figure 3.2. The GO spectrum shows typical features associated with the presence of epoxide groups (1254 cm^{-1}, asymmetric stretch; 829 cm^{-1}, bending vibration), phenolic groups (1104 cm^{-1}, C–O stretching vibration) and carboxylic groups (1662 cm^{-1}; C=O stretching vibration). The peak at ~1386 cm^{-1} is assigned to O–H deformations and the O–H vibrations are seen at 3050-3800 cm^{-1}. In the ODA-G1 spectrum the peaks are significantly broadened and the appearance of C=C (sp^2-hybridized carbon) in-plane vibrations at 1570 cm^{-1} may be related to the partial regeneration of the graphene electronic structure. The weak peak at 1650 cm^{-1} is associated with amide functional groups in ODA-G1 (C=O amide stretch). The C–H vibrations from the ODA groups appear at 1465 cm^{-1} (C-H bend) and 2850 cm^{-1} and 2918 cm^{-1} (C–H stretch). DCC is known to dehydrate alcohols and thus under the present (basic) conditions it may be effective in restoring the conjugation of carbon atoms, which carry epoxide or alcohol functionalities, as well as facilitating the formation of octadecylamido groups from carboxylic acids.[1]

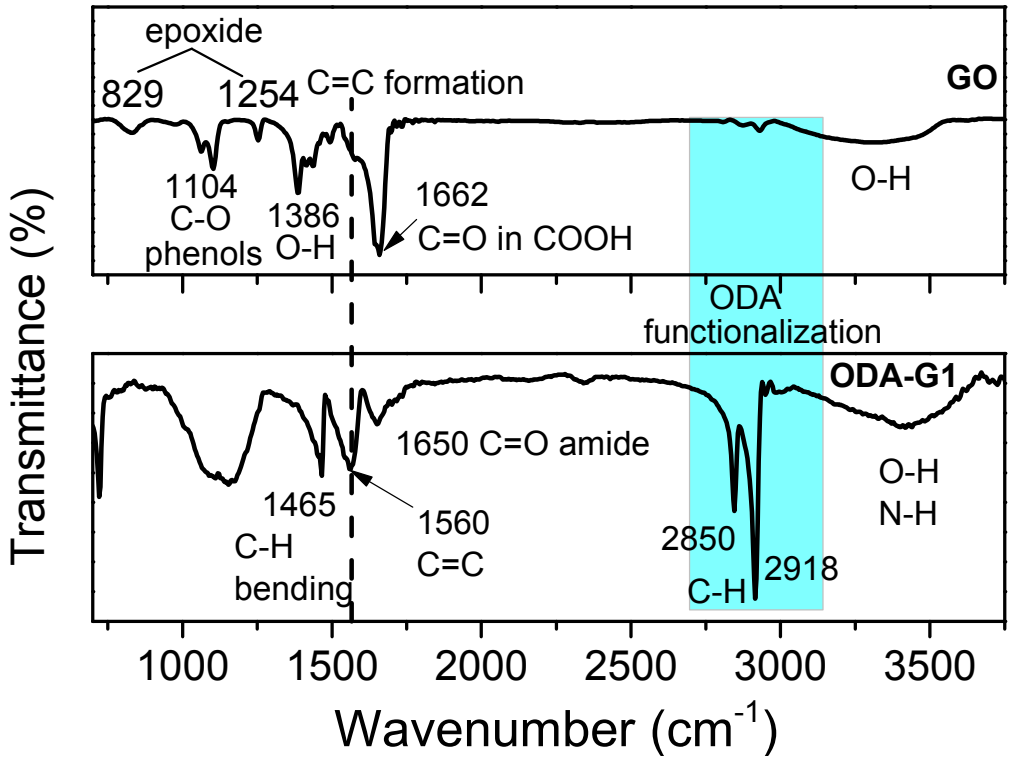

Figure 3.2 ATR-IR spectra of graphene oxide (GO) and octadecylamine functionalized graphene (ODA-G1).

In addition to qualitative assessment of the chemical groups, mid-IR spectroscopy provides valuable quantitative information regarding the amount of alkyl chain groups (ODA) attached to the graphene. A known amount of ODA-G1 was dispersed in CCl_4 by ultrasonication to prepare a 1mg/ml dispersion and the

spectrum was recorded in the range between 2700 and 3100 cm^{-1} (Figure 3.3). From the intensity of the peak at 2845 cm^{-1} and the extinction coefficient of ODA at this wavelength (ε = 606 L mol^{-1} cm^{-1}) we estimated that the weight concentration of the octadecylamide group in ODA-G1 is 20%. The calculation details are given below:

The absorbance of the solution is given by-

$$A = \varepsilon C b \tag{3.1}$$

where A is absorbance, ε = extinction coefficient (either L mol^{-1} cm^{-1} or L g^{-1} cm^{-1}), b = path length of the cuvette (cm), and C = concentration (either mol L^{-1}, g L^{-1}, or g cm^{-3}).

Thus from eq. 3.1, the concentration of ODA in the solution is:

$$C_{ODA} = {A}/{\varepsilon b} = \frac{0.046}{606\ {L}/{mol\,cm} \times 0.1\,cm} = 0.75\times10^{-3}\ {mol}/{L} \tag{3.2}$$

The MW of ODA is 269 g/mol, hence

$$C_{ODA} = 0.75\times10^{-3}\ {mol}/{L} \times 269\ {g}/{mol} = 0.2\ {g}/{L} \tag{3.3}$$

The mole ratio (n) of ODA in the ODA-SWNT material is

$$n = \frac{m_{ODA}}{m_{ODA-G}} = \frac{C_{ODA}\times V}{C_{ODA-G}\times V} = \frac{C_{ODA}}{C_{ODA-G}} \tag{3.4}$$

Thus for $C_{ODA\text{-}G1}$ of 1 mg/mL we obtain n = 0.2 or 20 wt. %

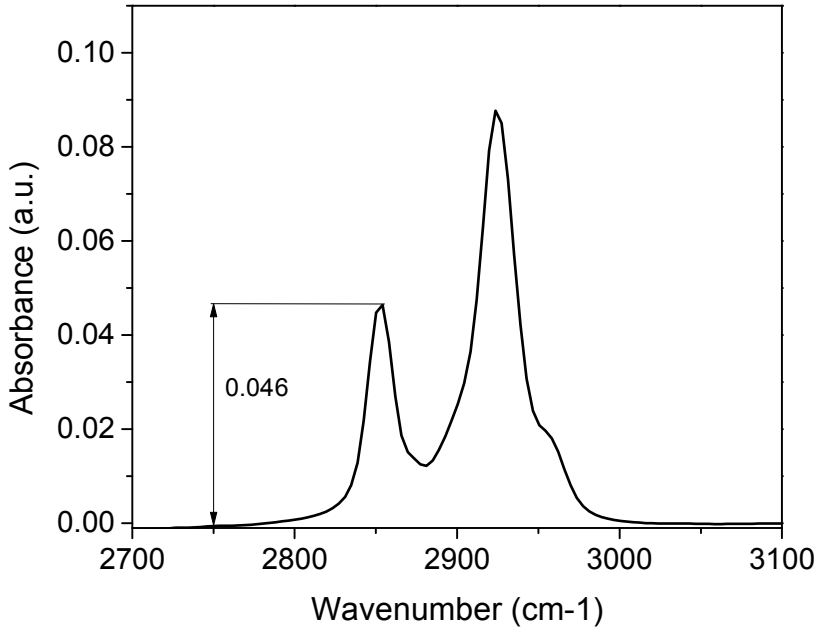

Figure 3.3 Absorbance spectrum of the ODA-G1 solutions in CCl_4 at a concentration of 1mg/ml (quartz cell, 1mm light path, Nicolet Nexus FT-IR spectrometer), showing ν(C-H) stretching vibrations.

The effect of the chemical reaction on the reduction of GO was further examined by Raman spectroscopy. The Raman spectra of GO, and ODA-G1 are compared in Figure 3.4. The ratio of the integrated intensities of the D and G peaks (I_D/I_G) provides a measure of the content of the sp^3 carbon centers and is a useful

index of the degree of chemical functionalization.[33, 34] The G-band in GO appears at 1590 cm^{-1} and it is accompanied by a broad D-band; I_D/I_G = 1.39. The chemical treatment shifts the G band back to ~1580 cm^{-1} in ODA-G1 and gives an I_D/I_G ratio of 1.11. In addition the FWHM of the D-band decreases from over 150 in GO to below 50 in ODA-G1. Other characteristic features in the Raman spectra are the 2D- and D+D* bands, which appear to be better defined in the ODA-G1 material, suggesting partial regeneration of the electronic π-conjugation.[35].

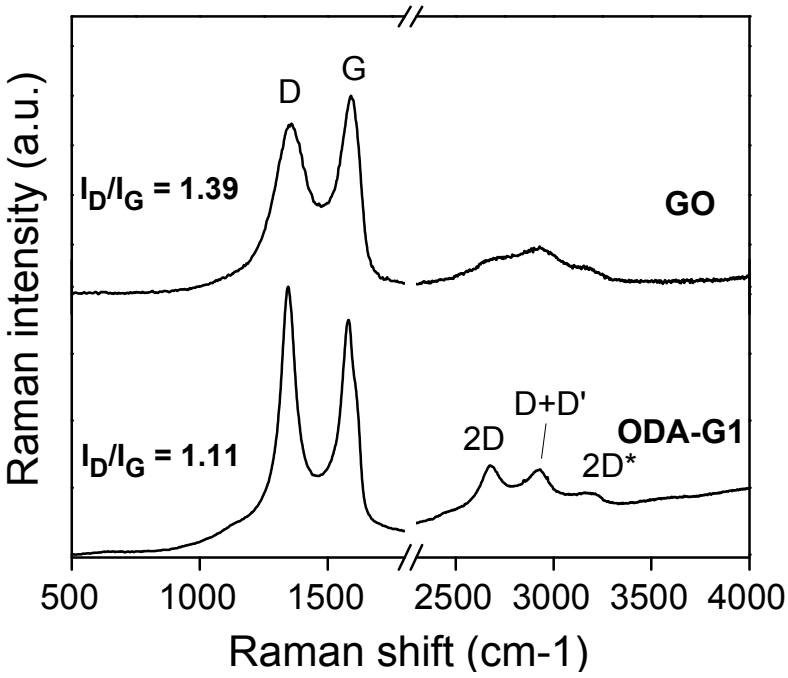

Figure 3.4 Raman spectra (λ_{ex} = 532 nm, spot size = 0.6 μm) of oxidized XG (GO), and octadecylamine functionalized graphene (ODA-G1).

In order to examine the solubility of ODA-G1 in organic solvents and compare it to that of XG, RGO and GO, the materials were dispersed in tetrahydrofuran (THF) at a concentration of 0.2 mg/mL. GO gave a stable brown solution, while the ODA-G1 and RGO solutions were black in color [36, 37], which after overnight standing gave rise to precipitates (Fig. 3.5a). The UV absorption spectra of the dispersions are compared in Fig. 3.5b. The spectrum of GO agrees with previous reports exhibiting a shoulder at ~ 300 nm due to the n→π* transitions of C=O [38]. At the same concentration, the absorbance intensities of the RGO and ODA-G1 solutions are noticeably higher than that of GO and the spectra are featureless in the visible-IR range of the spectrum, with a peak at ~270 nm. The increased absorbance and the presence of a peak at ~ 270 nm suggest a regeneration of the electronic conjugation within the graphene sheets [36, 37, 39-41]. The degree of conjugation present in the graphene materials is expected to affect their extinction coefficient and we examined the Lambert-Beer behavior of the materials in the visible spectral range (660 nm).

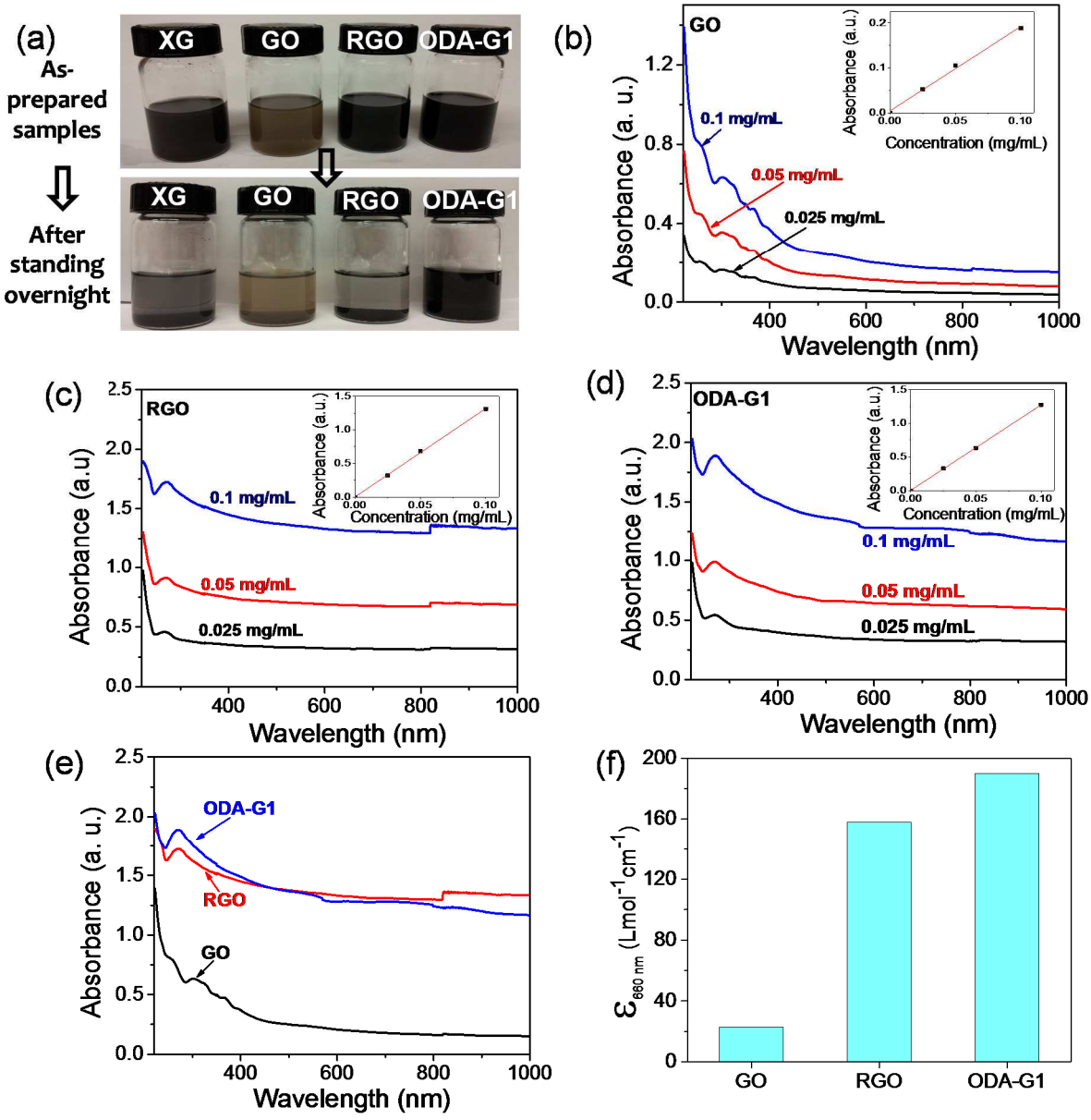
(a)
As-prepared samples
After standing overnight
XG
GO
RGO
ODA-G1
(b)
GO
0.1 mg/mL
0.05 mg/mL
0.025 mg/mL
Absorbance (a. u.)
Wavelength (nm)
Absorbance (a.u.)
Concentration (mg/mL)
(c)
RGO
0.1 mg/mL
0.05 mg/mL
0.025 mg/mL
Absorbance (a.u)
Wavelength (nm)
(d)
ODA-G1
0.1 mg/mL
0.05 mg/mL
0.025 mg/mL
Absorbance (a.u.)
Wavelength (nm)
(e)
ODA-G1
RGO
GO
Absorbance (a. u.)
Wavelength (nm)
(f)
$\varepsilon_{660\,nm}$ (Lmol^{-1}cm^{-1})
GO
RGO
ODA-G1

Figure 3.5 (a) Optical images of THF dispersions of expanded graphite (XG), oxidized expanded graphite (GO), reduced graphene oxide (RGO), and octadecylamine functionalized graphene (ODA-G1). Absorption spectra of dispersions of (b) GO, (c) RGO, and (d) ODA-G1 in THF at different concentrations. The insets in b, c, and d show the absorbance of GO, RGO, and ODA-G1 at 660 nm as a function of concentration. (e) Absorption spectra of dispersions of GO, RGO, and ODA-G1 in THF at concentration of 0.1 mg/mL. (f) Extinction coefficient of GO, RGO and ODA-G1 at 660 nm.

As shown in the insets of Figure 3.5c-e, all solutions obey the Lambert-Beer's law as evidenced by the linear relation between absorbance and concentration in the range of concentrations between 0.025 mg/mL and 0.1 mg/mL, which allows the calculation of the extinction coefficients (ε_{660}). GO has a molar extinction coefficient of 23 L mol^{-1} cm^{-1}, which after chemical reduction by hydrazine (RGO) increases to 158 L mol^{-1} cm^{-1}. ODA-G1 shows an extinction coefficient of 190 L mol^{-1} cm^{-1}, which is similar to RGO in our experiments (158 L mol^{-1} cm^{-1}) and comparable with that of liquid exfoliated graphene solutions (295 L mol^{-1} cm^{-1}, 167 L mol^{-1} cm^{-1}).[42, 43]

To understand the role of ODA and DCC in restoring electronic conjugation, we prepared a reference sample (ODA-G2) according to previous literature procedure [1] without the presence of DCC. The GO material was reacted directly with DCC. The UV-Vis-NIR absorbance spectra of the ODA-G2 and Dehy-GO samples are compared with those of GO, and ODA-G1 in Fig. 3.6. The extinction coefficient of ODA-G2 prepared by the synthetic route without DCC is 52 L mol^{-1} cm^{-1}, which agrees with previously reported value.[1] The low extinction coefficient of ODA-G2 indicates the importance of DCC in restoring the conjugation of the graphene sheets. When GO is reacted with DCC directly, the extinction coefficient increases to 155 L mol^{-1} cm^{-1}, indicating the DCC could help to restore the electronic conjugation by dehydrating the graphene oxide.

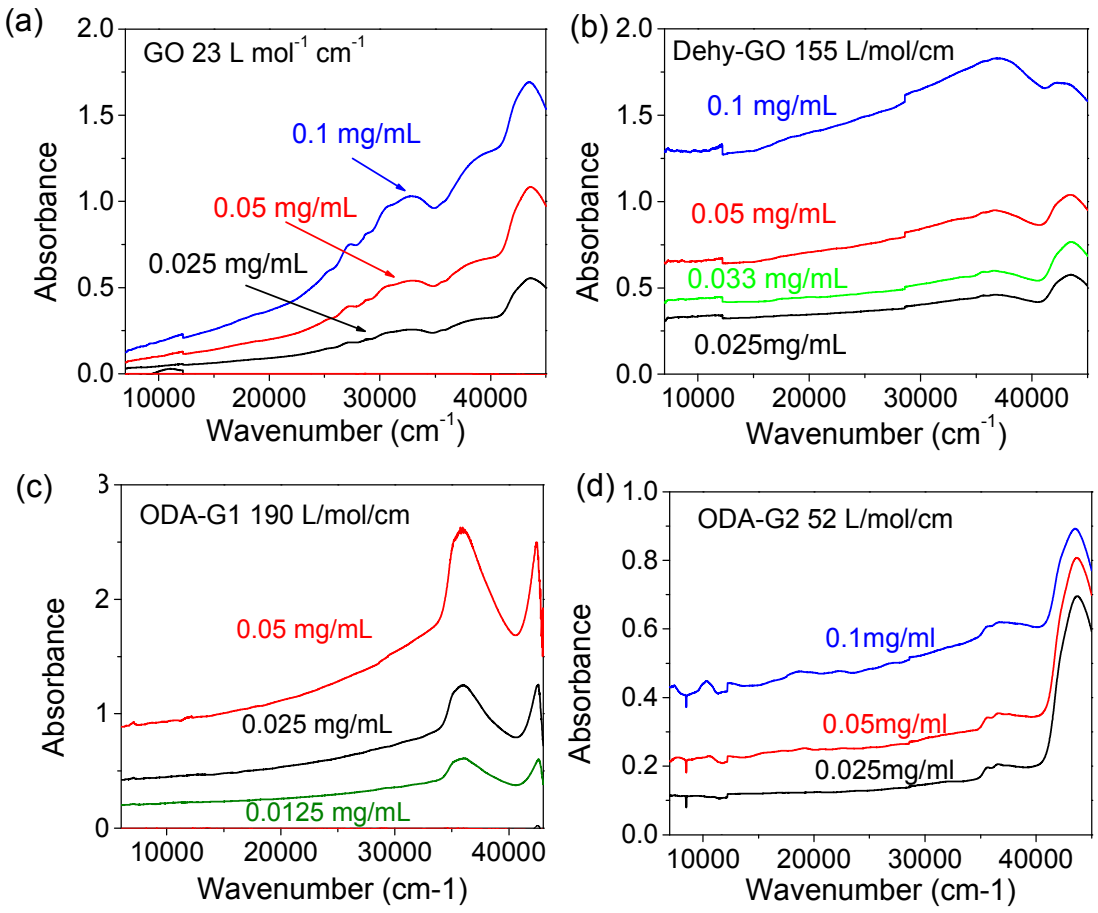

Figure 3.6 UV-Vis NIR spectra of (a) GO, (b) Dehy-GO, (c) ODA-G1, and (d) ODA-G2.

It is useful to be able to directly compare the spectroscopic properties of dispersions and films of carbon materials. We developed an analytical relationship between the absorption coefficients of films and the solution state extinction coefficients of materials that are held in the same orientation with respect to the path of the light beam; thus the relationship is valid for isotropic materials. This problem is relevant to the interpretation of the results obtained on single and multilayer films of oriented sheets of graphene that have been examined by absorption spectroscopy,[44] and their relationship to solution studies.

We carry out the calculation in two steps, beginning with the transformation of the solid state absorption coefficient of a single layer graphene to a suspended single layer of solution state graphene in which the graphene layer maintains the same (perpendicular) orientation to the light beam of the spectrometer. Thus the calculation assumes that the material in question is isotropic and without orientational preferences; the treatment is general and applicable to any material (in the absence of anisotropy).

We begin with a geometrical representation of a single layer of material of width (*w*, cm), length (*l*, cm) and thickness (*x*, cm). The fundamental relationships are as follows:

Solid state films- $T = I/I_0 = e^{-\alpha x}$; $A = -\log_{10} T = \alpha x / 2.3026$ (3.5)

where *A* = absorbance, T = transmittance, I_0 = intensity of incident light, I = intensity of transmitted light, α = absorption coefficient (cm^{-1}), and *x* = thickness of film (cm).

Solutions- $A = \varepsilon b C$ (3.1)

where ε = extinction coefficient (either L mol^{-1} cm^{-1} or L g^{-1} cm^{-1}), *b* = path length of cuvette (cm), and *C* = concentration (either mol L^{-1}, g L^{-1}, or g cm^{-3}).

Thus from eqs 3.1 and 3.5, we obtain-

$$\varepsilon = \frac{\alpha x}{2.3026\, b C} \tag{3.6}$$

In order to obtain the solid state analog of the passage of light through a cell of path length *b* containing a solution of concentration *C*, we express the geometry of the solution sample in units appropriate for a solid state sample (g cm^{-3}), Figure 3.7.

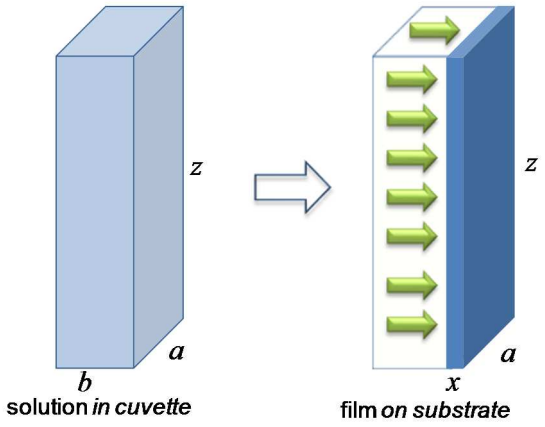

Figure 3.7 Schematic illustration of the idealized transformation between a dispersion of material in a cuvette (left), and the corresponding film formed by deposition of the material in the solution on a substrate with the same areal dimensions.

The quantity *bC* (eqs 3.1 and 3.6), is the effective mass of sample per unit area (cm^2) on the face of the cuvette if the solvent is removed to give a uniform layer, and the equivalent thickness of the resulting film (*x*), is given by $x = bC/d$, where C is expressed in g cm^{-3} and *d* is film density in g cm^{-3}; thus $bC = xd$ and eq 6 becomes

$$\varepsilon = \frac{\alpha}{2.3026d} \text{ (cm}^3\text{ g}^{-1}\text{ cm}^{-1}\text{)} \tag{3.7}$$

$$\varepsilon = \frac{\alpha}{2302.6d} \text{ (L g}^{-1}\text{ cm}^{-1}\text{)} \tag{3.8}$$

$$\varepsilon = \frac{\alpha}{2302.6d} MW \text{ (L mol}^{-1}\text{ cm}^{-1}\text{)} \tag{3.9}$$

where *MW* is the molecular or atomic weight.

We applied this analysis to the isotropic molecule C_{60} for which the thin film absorption coefficients are reported as: $\alpha = 6.07 \times 10^5$ cm^{-1} (λ = 220 nm), $\alpha = 6.70 \times 10^5$ cm^{-1} (λ = 268 nm), $\alpha = 3.75 \times 10^5$ cm^{-1} (λ = 346 nm), $\alpha = 1.21 \times 10^5$ cm^{-1} (λ = 442 nm)[45]. The experimental extinction coefficients of C_{60} in hexane[46], together with the values calculated from eq 3.6 are: ε = 135,000 [95,900] (λ = 209 nm), ε = 175,000 [105,800] (λ = 255 nm), ε = 51,000 [59,200] (λ = 327 nm), ε = weak [19,100]. The agreement is reasonable, but in general the peak heights for the solutions are higher than those in the films; this is probably due to the broadening of the absorptions by solid state interactions[45].

For monolayer graphene of thickness, x = 0.34 nm, transmittance, T = 0.977,[44] and density d = 2.23 g cm^{-3} we obtain from eq 6, $\alpha = 6.84 \times 10^5$ cm^{-1}; thus eq 3.8 and 3.9, give ε = 133.3 L g^{-1} cm^{-1} and 1599.4 L mol^{-1} cm^{-1}.

In the case of as-prepared electric arc single-walled carbon nanotubes (EA-AP-SWNTs), a film of thickness, x = 40 nm, gives an absorbance, A = 0.19 at the S_{22} interband electronic transition[47], which corresponds to $\alpha = 1.09 \times 10^5$ cm^{-1}, and ε = 39.6 L g^{-1} cm^{-1} and 475 L mol^{-1} cm^{-1} in good agreement with the solution extinction coefficients (for EA-P2, ε = 38 L g^{-1} cm^{-1} and 450 L mol^{-1} cm^{-1})[48, 49].

The results for these carbon materials are summarized in Table 3.1; the extinction coefficients derived for graphene from the thin films are much higher than values in the literature, which could be a result from the rotational reorientation of the graphene films due to tumbling in solution.

Table 3.1 Absorption Coefficients and Extinction Coefficients of Thin Films and Solutions of Carbon Materials.[a]

Material	Wavelength λ, nm	Absorption Coefficient $\alpha \times 10^5$, cm^{-1}	Ref.	Extinction Coefficient ε $L\ g^{-1}cm^{-1}$	Method / Ref.	Extinction Coefficient ε $L\ g^{-1}cm^{-1}$	Method / Ref.
ODA-G1 (film)	660	0.031		16.8	C8	202	C9
ODA-G1 (dispersion, THF)	660			15.8		190	
Graphene (film, single layer)		6.84	44	133.2	C8	1600	C9
Graphene (dispersion, NMP)	660			24.6	42	295	
Graphene (aqueous dispersion, surfactant)	660			66	50	792	
Graphene (exfoliated, ball mill, melamine)	660			9.3	51	112	C9
Graphene (expanded, ODCB)	660			27.5	52	330	C9
EA-SWNTs (film)	1000 (S_{22})	1.09	47	39.4	C8	473	C9
EA-SWNTs (dispersion, DMF)	1000 (S_{22})			38	48, 49	450	
C_{60} (film)	220 268 346 442	6.07 6.70 3.75 1.21	45	159.8 176.3 98.7 31.8	C8	95,900 105,800 59,200 19,100	C9

C_{60} (dispersion, hexane)	209 255 327					135,000 175,000 51,000	46
	210 256 328 404					143,280 148,104 43,200 2,160	

[a]C8 − derived from solid state value by use of eq 3.8; C9 − derived from solid state value by use of eq 3.9; Densities: d = 1.65 g cm^{-3} (C_{60}), 1.2 g cm^{-3} (EA-SWNTs), 0.08 g cm^{-3} (ODA-G1) . EA-SWNT – electric arc single-walled carbon nanotubes, ODA-G1 – octadecylamine functionalized graphene with the presence of DCC. Note that experimental solution state extinction coefficient of graphene could be reduced by rotational averaging

The absorption spectra of the isotropic molecule C_{60} in solution and in a thin film form are shown in Fig. 3.8. It is apparent that the peaks are sharper and more intense in the solution spectra than those in the film, as a result of solid state interactions [45]. Nevertheless for most of the carbon nanomaterials in Table 3.1, including the functionalized graphene (ODA-G1) and single walled carbon nanotube (EA-SWNT) samples the correspondence is surprising good, suggesting that orientational effects do not play a major role in the solid state spectra of these materials. In the case of pristine single layer graphene, where the film is held perpendicular to the light beam, the solid state absorption coefficient suggests a much higher extinction coefficient for the solution state than the observed experimentally (due to the neglect of rotational averaging).

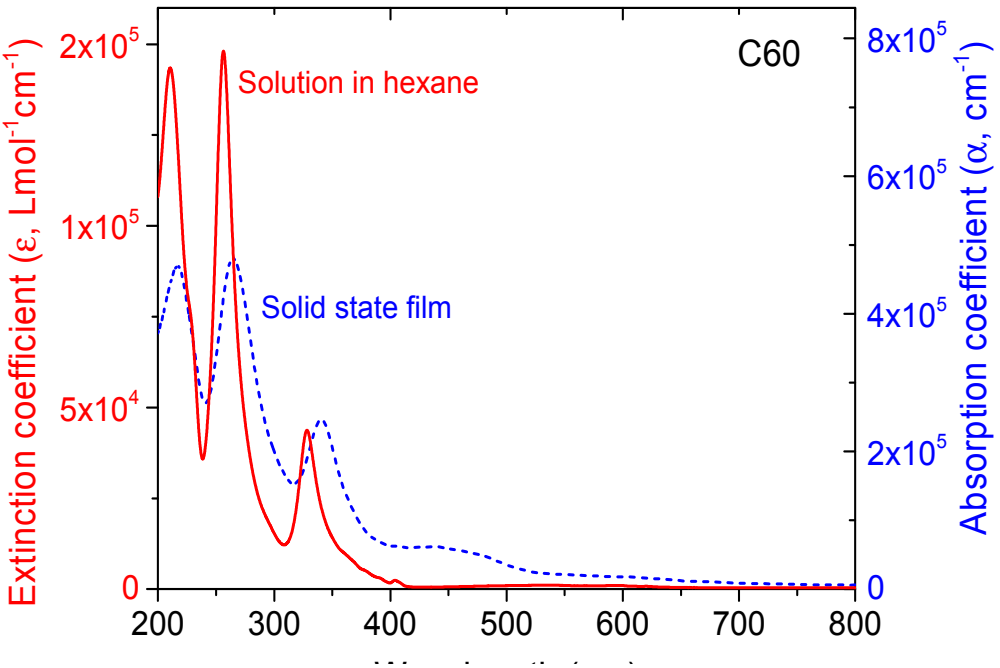

Figure 3.8 Absorption spectra of a solution of C60 in hexane at a concentration of 0.01 mg/mL and an 80 nm C60 film deposited on a sapphire substrate; the extinction and absorption coefficients are interrelated by Eq 3.9.

It is important to note that the ODA functionalization of GO with the help of DCC resulted in predominantly few-layer and/or individual graphene sheets as observed by SEM and shown in Figure 3.9a. In order to explore the effect of the reduction process on the electronic properties of ODA-G1 we measured the sheet resistance of films (thickness of 100 μm) in a van der Pauw configuration. Figure 3.9b compares the conductivity of GO, OGA-G1, RGO, and XG films.

As expected the GO film displays the lowest conductivity (~1x 10^{-7} S cm^{-1}). Chemical reduction of GO partially restores the conjugated structure of the graphene flakes [13] and the conductivity of the ODA-G1 film increases by five orders of magnitude to 0.05 S cm^{-1}. Interestingly, ODA-G1 has comparable electrical properties to that of ODA functionalized single-walled carbon nanotubes [47]. Thus, the functionalization of graphene sheets with ODA in the presence of the coupling agent DCC, leads to a significant regeneration of its electrical properties. For comparison the direct reaction of GO with ODA yields a material with conductivity of 1.2 x 10^{-4} S/cm [26] Furthermore, thermal treatment of the ODA-G1 film at 300°C for 3 hours in vacuum at 10^{-7} torr, led to a 100-fold increase of the conductivity ($\sigma_{a\text{-}ODA\text{-}G1}$ = 4.5 S cm^{-1}). The conductivity of the derived material, a-ODA-G1, is higher than that of the conductivity of RGO, prepared by hydrazine reduction, (σ_{RGO} = 1.9 S cm^{-1}).

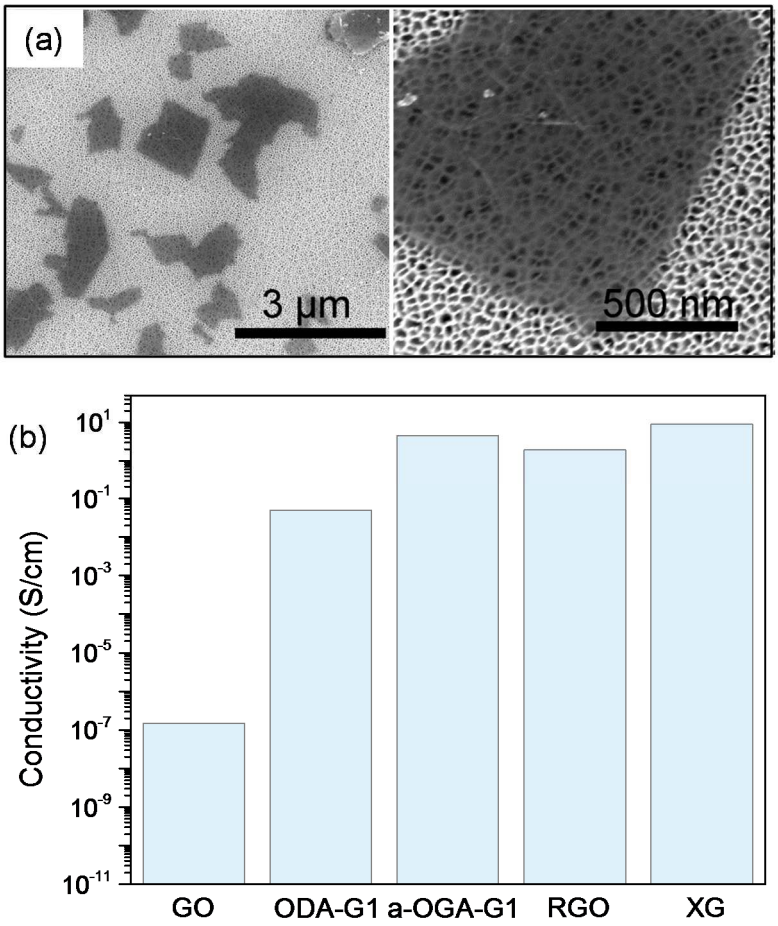

Figure 3.9 (a) Scanning electron microscopy (SEM) images of octadecylamine functionalized graphene with DCC (ODA-G1). The SEM images of ODA-G1 on the alumina membrane illustrate that the graphene flakes are semi-transparent and the alumina substrate texture is visible under the thin ODA-G1 sheets. (b) Conductivity of 100 µm films of expanded graphite (XG), oxidized XG (GO), reduced graphene oxide (RGO), octadecylamine functionalized graphene (ODA-G1) and annealed ODA-G1 (a-ODA-G1)

3.4 Conclusion

The combination of electronic absorption spectroscopy and conductivity measurements provides a powerful tool for the characterization of carbon materials and the extent of conjugation in their electronic structure which is further strengthened by the ability to directly compare the electronic absorptions of the materials in the form of solid state thin films and as dispersions. We examined the electronic absorption spectroscopy and conductivity of octadecylamine (ODA) functionalized graphene, which was obtained by the direct coupling of ODA with graphene oxide (GO) in the presence of dicyclohexydiimide (DCC). We found that the extent of the regeneration of the conjugation by DCC/ODA functionalization is comparable to that achieved by the chemical reduction of GO by hydrazine (RGO). The spectroscopic absorption and extinction coefficients were used to benchmark the reduced graphene materials and the Raman and conductivity measurements confirm the regeneration of the π-conjugation in ODA-G1; the material provides organic solubility and processability in combination with well developed π-conjugation.

References

1. Niyogi, S., et al. *J. Am. Chem. Soc.* **2006,** 128, 7720.
2. Tung, V. C.; Allen, M. J.; Yang, Y.; Kaner, R. B. *Nature Nanotech.* **2009,** 4, 25.
3. Zhu, Y.; James, D. K.; Tour, J. M. *Adv. Mater.* **2012,** 24, 4924.
4. Bekyarova, E.; Sarkar, S.; Niyogi, S.; Itkis, M. E.; Haddon, R. C. *J. Phys. D: Appl. Phys.* **2012,** 45, 154009.
5. Luo, J.; Kim, J.; Huang, J. *Acc. Chem. Res.* **2013,** 46, 2225.
6. Mohanty, N.; Berry, V. *Nano Lett.* **2008,** 8, 4469.
7. Simon, P.; Gogotsi, Y. *Nature Mater.* **2008,** 7, 845.
8. Marcano, D. C., et al. *ACS Nano* **2010,** 4, 4806.
9. Erickson, K., et al. *Adv. Mater.* **2010,** 22, 4467.
10. Dreyer, D. R.; Park, S.; Bielawski, C. W.; Ruoff, R. S. *Chem. Soc. Rev.* **2010,** 39, 228.
11. Stankovich, S., et al. *Nature* **2006,** 442, 282.
12. Stankovich, S., et al. *Carbon* **2007,** 45, 1558.
13. Shin, H. J., et al. *Adv. Funct. Mater.* **2009,** 19, 1987.
14. Salas, E. C.; Sun, Z.; Luttge, A.; Tour, J. M. *ACS Nano* **2010,** 4, 4852.
15. Dreyer, D. R.; Murali, S.; Zhu, Y.; Ruoff, R. S.; Bielawski, C. W. *J. Mater. Chem.* **2011,** 21, 3443.
16. Eda, G.; Fanchini, G.; Chhowalla, M. *Nature Nanotech.* **2008,** 3, 270.
17. Wang, X.; Zhi, L. J.; Mullen, K. *Nano Lett.* **2008,** 8, 323.
18. Becerril, H. A., et al. *ACS Nano* **2008,** 2, 463.
19. Xu, Y., et al. *Carbon* **2010,** 48, 3308.
20. Wang, S., et al. *Nano Lett.* **2010,** 10, 92.

21. Wassei, J. K.; Kaner, R. B. *Mater. Today* **2010,** 13, 52.

22. Stankovich, S., et al. *J. Mater. Chem.* **2006,** 16, 155.

23. Chen, J., et al. *Science* **1998,** 282, 95.

24. Bourlinos, A. B., et al. *Langmuir* **2003,** 19, 6050.

25. Wang, S., et al. *Adv. Mater.* **2008,** 9999, 1.

26. Li, W., et al. *Carbon* **2011,** 49, 4724.

27. Wang, G. Z.; Shen, X.; Wang, B.; Yao, J.; Park, J. *Carbon* **2009,** 47, 1359.

28. Lin, T.; Tang, C.; Shi, J. *App. Phys. Lett.* **2013,** 103, 132407.

29. Jha, N.; Ramesh, P.; Bekyarova, E.; Itkis, M. E.; Haddon, R. C. *Adv. Energy Mater.* **2012,** 2, 438.

30. Yu, A.; Ramesh, P.; Itkis, M. E.; Bekyarova, E.; Haddon, R. C. *J. Phys. Chem. C* **2007,** 111, 7565.

31. Hontorialucas, C.; Lopezpeinado, A. J.; Lopezgonzalez, J. D. D.; Rojascervantes, M. L.; Martinaranda, R. M. *Carbon* **1995,** 33, 1585.

32. Worsley, K. A.; Kalinina, I.; Bekyarova, E.; Haddon, R. C. *J. Am. Chem. Soc.* **2009,** 131, 18153.

33. Niyogi, S., et al. *Nano Lett.* **2010,** 10, 4061–4066.

34. Sarkar, S.; Bekyarova, E.; Haddon, R. C. *Angew. Chem. Int. Ed.* **2012,** 51, 4901.

35. Zhan, D., et al. *Carbon* **2011,** 49, 1362.

36. Zhou, Y.; Bao, Q.; Tang, L.; Zhong, Y.; Loh, K. P. *Chem. Mater.* **2009,** 21, 2950.

37. Mohanty, N.; Nagaraja, A.; Armesto, J.; Berry, V. *Small* **2010,** 6, 226.

38. Paredes, J. I.; Villar-Rodil, S.; Martinez-Alonso, A.; Tascon, J. M. D. *Langmuir* **2008,** 24, 10560.

39. Li, D.; Muller, M. B.; Gilje, S.; Kaner, R. B.; Wallace, G. G. *Nature Nanotech.* **2008,** 3, 101.

40. Englert, J. M., et al. *Adv. Mat.* **2009,** 21, 4265.

41. Englert, J. M., et al. *Chem. Commun.* **2012,** 8, 5025.

42. Hernandez, Y., et al. *Nature Nanotech.* **2008,** 3, 563.

43. Lotya, M., et al. *J. Am. Chem. Soc* **2009,** 131, 3611.

44. Nair, R. R., et al. *Science* **2008,** 320, 1308.

45. Hebard, A. F.; Haddon, R. C.; Fleming, R. M.; Kortan, A. R. *Appl. Phys. Lett* **1991,** 59, 2109.

46. Hare, J. P.; Kroto, H. W.; Taylor, R. *Chem. Phys. Lett.* **1991,** 177, 394.

47. Bekyarova, E., et al. *J. Am. Chem. Soc.* **2005,** 127, 5990.

48. Zhao, B., et al. *J. Nanosci. Nanotechnol.* **2004,** 4, 995.

49. Zhao, B., et al. *J. Phys. Chem. B* **2004,** 108, 8136.

50. Lotya, M.; King, P. J.; Khan, U.; De, S.; Coleman, J. N. *ACS Nano* **2010,** 4, 3155.

51. Quintana, M.; Vazquez, E.; Prato, M. *Acc. Chem. Res.* **2013,** 46, 138.

52. Hamilton, C. E.; Lomeda, J. R.; Sun, Z. Z.; Tour, J. M.; Barron, A. R. *Nano Lett.* **2009,** 9, 3460.

Chapter 4. Thin Thermal Interface Layers of Graphite Nanoplatelet-Based Composites

4.1 Anisotropic thermal and electrical properties of thin thermal interface layers of graphite nanoplatelet-based composites

4.1.1 Introduction

Thermal interface materials (TIMs) are crucial components of advanced high density electronic packaging and are necessary for the heat dissipation which is required to prevent the failure of electronic components due to overheating.[1, 2] Conventional TIMs are manufactured by introducing highly thermally conductive fillers, like metal or metal oxide microparticles, into the polymer matrix.[3-5] With the rise of graphene,[6] a product of graphite exfoliation,[7, 8] graphite nanoplatelets (GNPs), have been receiving significant attention as a new form of thermally conducting filler.[9-24] The GNPs are 2D high aspect ratio nanoparticles containing a few to hundreds of stacked graphene layers and because they possess the high in-plane thermal conductivity of graphite (~2,000 W/m*K), are expected to form a very efficient heat conduction pathway in polymer matrices. Indeed a tenfold enhancement of the thermal conductivity was achieved by adding only 5 to10 wt% of GNPs to the polymer matrix which allowed the preparation of composites with thermal conductivities up to 2 W/m*K,[10-13, 15, 19, 20, 22, 25] while conventional low aspect ratio fillers require a loading in the range of 60-90% to achieve a similar increase in the thermal

conductivity.[5] With further increase of the GNP filler loading, composites with very high thermal conductivities (5-10W/m*K) have been reported.[10, 11, 14, 24]

Most previous studies of GNP based TIM composites have focused on the bulk thermal properties of macroscopic solid state specimens with a typical thickness of 2-10 mm, while practical thermal management applications require thin TIM layers with a bondline thickness of 10-100 μm, in a spreadable and conformable state which can completely fill the gap between the contacting surfaces while penetrating the crevices associated with the microscale surface roughness.[2] The TIM layer is expected to provide efficient heat flow from the die to the heat sink in the direction normal to the thermal interface as shown in Fig.4.1a. Thus in such applications the ideal orientation of the GNPs is normal to the thermal interface plane which would take full advantage of the high in-plane thermal conductivity of graphite (Fig.4.1b), whereas the isotropic, random (Fig.4.1c) and parallel orientations (Fig. 4.1d) are expected to be much less favorable.

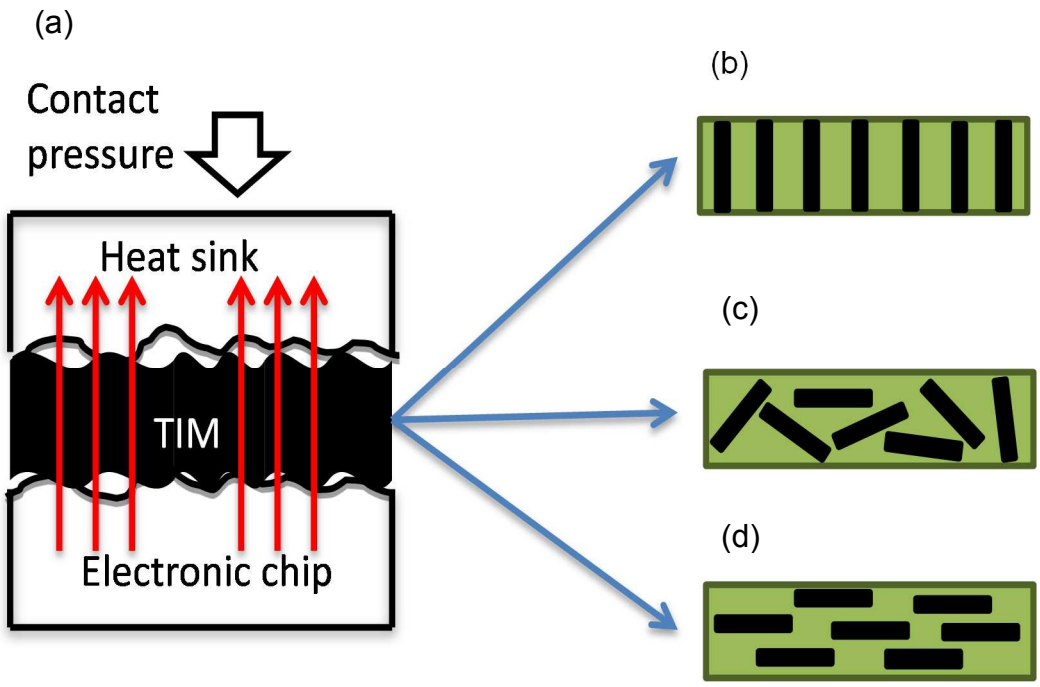

Figure 4.1 Orientations of high aspect ratio GNP fillers in thin thermal interface layer in electronic packaging applications. (a), Schematic showing the utilization of thermal interface material layer for heat removal in electronic packaging. Possible orientations of GNPs in thin TIM layer: (b), preferentially through-plane, (c), isotropic, and (d), preferentially in-plane.

In practice, the thin TIM layer is formed by spreading the material between the contacting surfaces under pressure or by underfilling the gap between parts by capillary flow.[2, 26, 27] During the spreading process the high aspect ratio of the

GNPs could lead to their preferential orientation within the thermal interface layer (Fig.4.1d), thus diminishing the contribution of the in-plane thermal conductivity of the graphitic layers.[16] An extreme example of such in-plane orientation of GNPs was recently demonstrated by the preparation of a GNP paper which showed a highly anisotropic thermal conductivity, with an in-plane thermal conductivity of ~ 100 W/m*K, whereas the through-plane thermal conductivities was less than 1 W/m*K.[17, 28] Similarly anisotropic heat conductance was recently demonstrated in boron nitride platelet thin films.[29] For practical application, GNP composite loadings in the range of 2-20 wt% are required but the orientational preferences of the GNPs in such composites has not been studied systematically and the thermal properties have often been assumed to be isotropic.[30] Here we report measurements which show a significant difference between the in-plane and through-plane electrical and thermal conductivities of thin layers of GNP-based thermal greases. We show that the anisotropic transport properties in the thin thermal interface layers originate from the preferential in-plane orientation of the GNPs and it is clear that the anisotropy of these composite matrices must be taken into account in the development of GNP based TIMs.

4.1.2 Experimental

Preparation of GNPs based thermal grease

In a typical experiment, 10g of natural graphite (TIMCAL Graphite and Carbon, Inc.) were treated for 12 hours at room temperature with a 120 mL

mixture of concentrated sulfuric and nitric acids (3:1). The intercalated graphite was filtered, washed with distilled water, air dried, and exfoliated in an oven at 800°C for 3 min under flow of argon. The exfoliated graphite was dispersed in acetone by high shear mixing for 30 min followed by bath sonication for 24h to produce GNPs dispersion. The polymers were added to the GNPs dispersions, high shear mixed for 30 minutes followed by removal of the solvent. The resulting mixtures were processed utilizing a dual asymmetric centrifuge Speed Mixer (DAC 150.1 FVZ, Flack Tek, Inc.) to produce homogeneous and spreadable thermal greases of a consistency which is typical of TIMs that are suitable for application. To prepare cured samples the curing agent (EPI-CURE W, Hexion) was added to the GNP-Epoxy 862 grease (1:4 ratio), the mixture was heated under a pressure of 40 psi at 80^{o}C for 2h, 100^{o}C for 2h and 150^{o}C for 2.5h to obtain thin films of thickness 100 to 300 μm.

Electrical conductivity measurement

For the in-plane electrical conductivity measurements the thermal greases were spread into a thin (75 μm) layer between two glass slides under a pressure of 40 psi at a temperature of 60°C, which is typical for TIM applications. The bottom slide was patterned with 4 in-line gold electrodes positioned 5 mm apart for 4-point electrical measurements (Fig.4.2a, inset). For through-plane electrical conductivity measurements 2-probe technique was applied; we measured the electrical resistances of three grease layers with thicknesses between 50 and

400 μm by sandwiching the grease layer between two gold coated glass slides (Fig.4.2b, inset) at the same pressure (40 psi) and temperature (60°C), which allows the calculation of the bulk through-plane electrical conductivity from the slope of the resistance as a function of thickness, thereby excluding the contact resistance.

Thermal conductivity measurement

The through-plane thermal conductivity of the GNP based greases was measured in the temperature range 30-60°C with a LW-9389 TIM Tester (Longwin, Taiwan) utilizing the steady-state heat flow technique according to ASTM D5470-06. The heat flow and the temperature across the TIM layer was measured utilizing a set of precision thermometers positioned in the Copper metal blocks along the direction of the thermal gradient (Fig.4.3a). The thermal resistances were measured for 3-4 thicknesses of the thermal grease layer (10 to 300 μm), and the bulk thermal conductivity of the grease was extracted from a plot of the resistance against thickness, thereby excluding the contact resistance (Fig.4.3c). The thermal conductivities of the polymer matrices Epoxy 862, PMM 1025 silicon oil and Hatcol 2372 measured by this technique were 0.15, 0.15 and 0.13 W/m*K, respectively. The in-plane thermal conductivity ($\kappa_{\parallel}$) of the GNP composite was measured in the temperature range 30-40°C by utilizing a comparative technique.[31-33] A thermal gradient was imposed by a miniature thermoelectric stage so as to direct the heat flow through the GNP sample and

the 0.5 mm diameter constantan wire of known thermal conductivity (19.5 W/m*K, reference sample), which was mounted in series. Miniature differential thermocouples were utilized to measure the temperature gradients across the GNP and the reference sample. The sign of the temperature gradient was alternated by reversing the voltage at the thermoelectric stage and the results of the two polarity measurements were averaged to exclude any contribution from black body radiation emanating from the sample. This freedom to invert the sign of the temperature gradient allowed us to position the same reference either before or after the sample with respect to the direction of heat flow, thereby measuring the heat flow entering or exiting the sample before or after the occurrence of radiative heat loss which is equivalent to using two references – a common practice in the comparative technique.[31-33] The experiment was enclosed in a vacuum chamber operating at a pressure of 10^{-6} Torr, and was tested on samples of known thermal conductivity.

Viscosity Measurements

The viscosity of the polymer matrices were measured using a Brookfield DV-II+Pro viscometer.

Thickness measurement

Procedures reported previously [20] were applied to measure the bondline thickness low to several micrometers. Certain amounts of paste were sandwiched between two Pyrex disks of 2 in. diameter. Under the pressure same

as what applied for thermal interface materials measurement, the paste spreads. And the thickness could be measured in two ways. One way is to measure the thickness of Pyrex disks before and after applying paste by micrometer. The other way is to measure the spreaded area, and calculate the thickness by the mass and density of paste sanwitched.

SEM study

SEM study was conducted utilizing Nova NanoSEM 50 instrument (FEI Company). The clean GNP film cross-sections were prepared by immersing the film in liquid nitrogen and breaking it in a frozen state by applying a shear force;[34]

4.1.3 Results and discussion

Three commonly used matrices of differing viscosities and chemical nature, Epoxy 862 (Hexion, viscosity ν=3050cP), PMM 1025 silicon oil (Gelest, ν=380cP), and Hatcol 2372 (Hatco, ν=234cP), were used to produce GNP-based thermal greases with GNP loadings of 10-14 wt.%, denoted as GNP-Epoxy862, GNP-Silicon oil and GNP-Hatcol 2372, respectively.

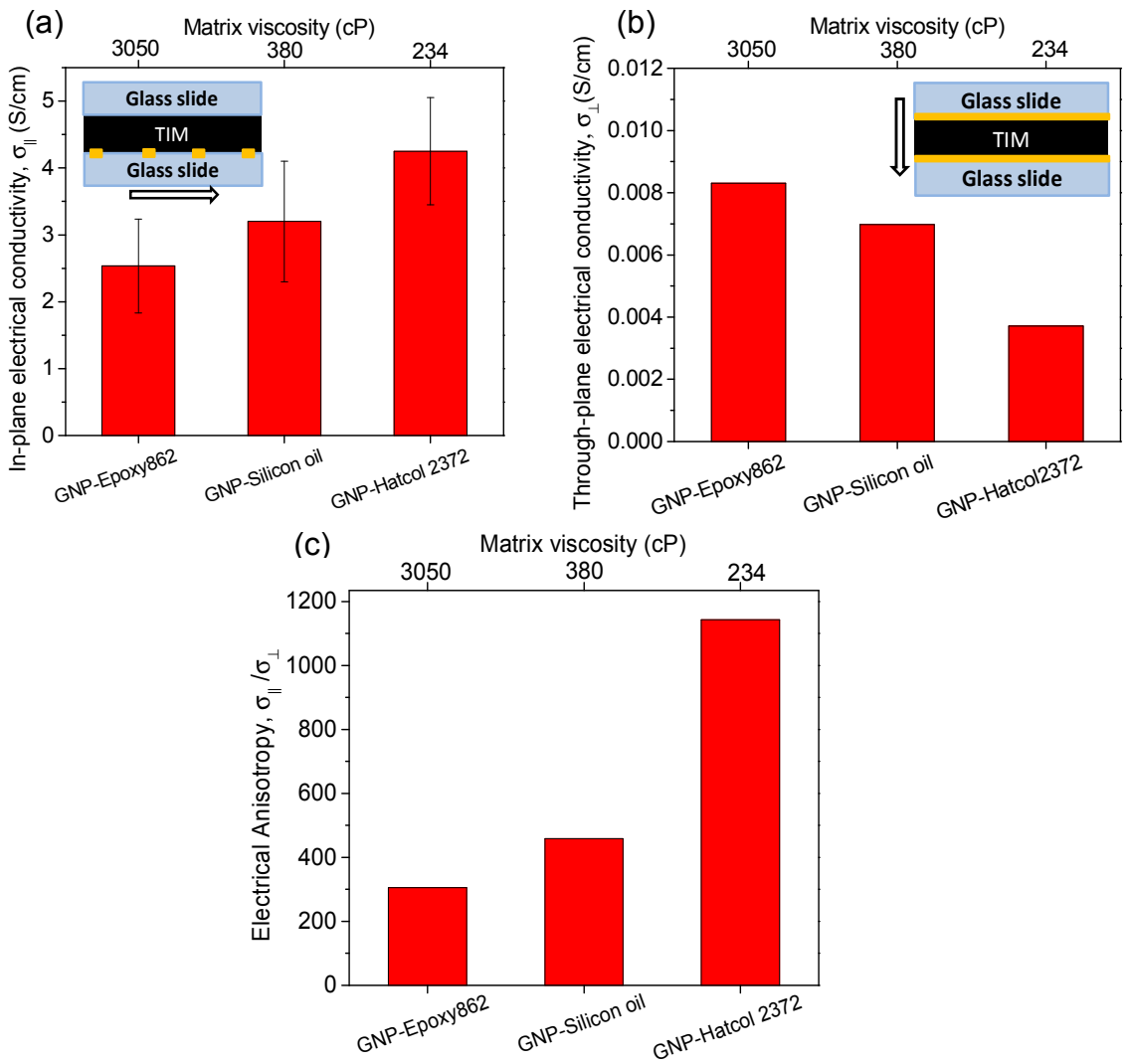

Figure 4.2 Measurements of anisotropic electrical conductivity in GNP-based thin thermal interface layers. (a), In-plane $\sigma_{\parallel}$ and (b), through-plane $\sigma_{\perp}$ electrical conductivities of GNP-based greases for matrices of different viscosities at GNP loading 14 Weight%, and (c), anisotropy values $\sigma_{\parallel}/\sigma_{\perp}$.for these greases. Insets in Fig.4.2a and Fig.4.2b show electrode configuration utilized for the in-plane and through-plane electrical measurements, respectively.

The in-plane and through-plane electrical conductivity data for the three GNP-based greases are presented in Fig.4.2(a, b). The results show that the in-plane and through-plane electrical conductivities of the GNP composites differ by several orders of magnitude. The in-plane electrical conductivity increases from $\sigma_{\parallel}$ = 2.4 to 4 S/cm with decreasing viscosity of the polymer matrix (Fig.4.2a), whereas the through-plane conductivity ($\sigma_{\perp}$) shows the opposite behavior (Fig.4.2b), and never exceeds 0.01 S/cm. Thus the electrical anisotropy increases with decreasing viscosity of the polymer and exceeds 1000 in the case of the low viscosity Hatco 2372 matrix (Fig.4.2c); these values are much higher than the anisotropies (~ 10) reported for bulk GNP based composites.[23, 34].

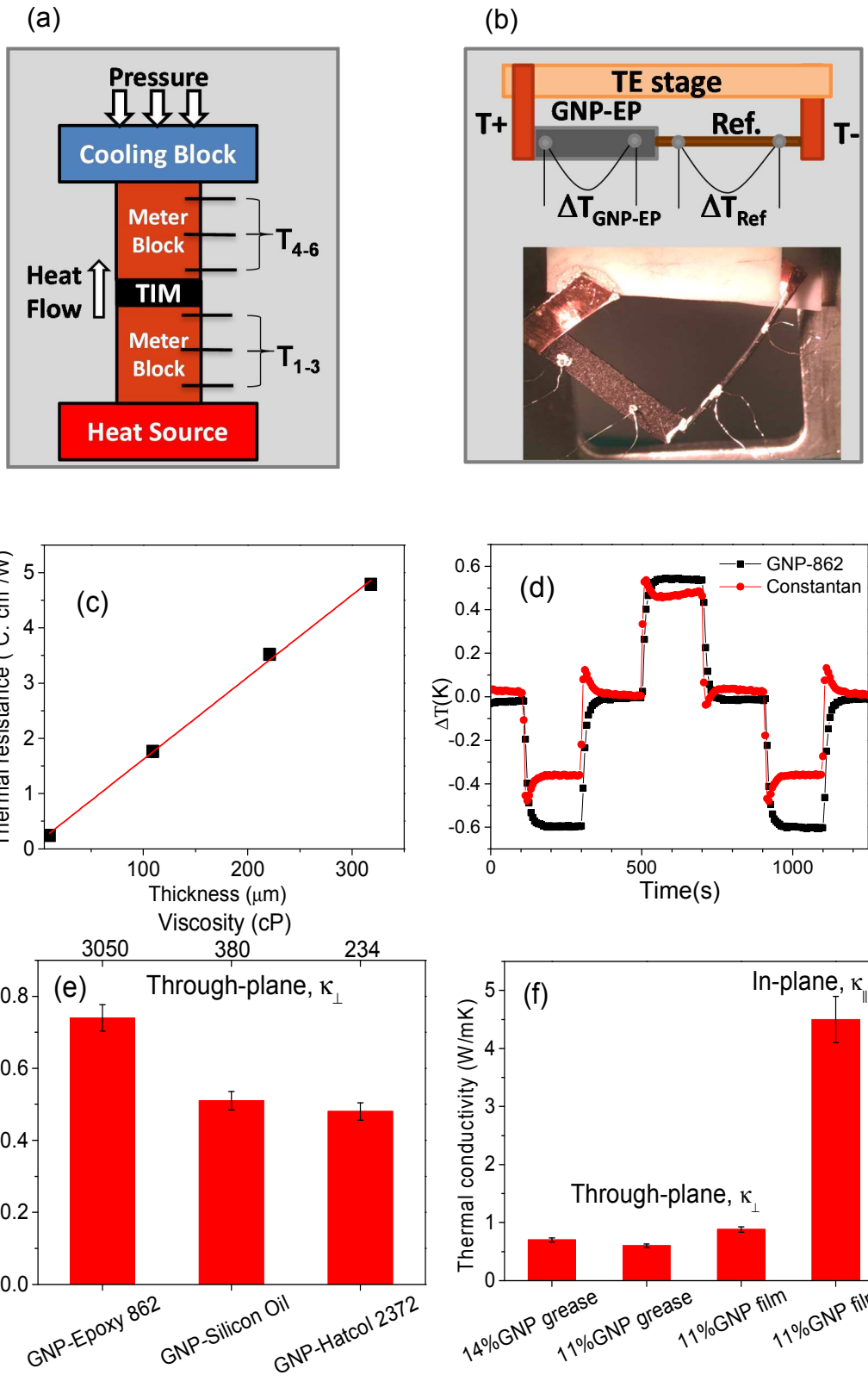
(a)
Pressure
Cooling Block
Meter Block
T_{4-6}
Heat Flow
TIM
Meter Block
T_{1-3}
Heat Source
(b)
TE stage
T+
GNP-EP
Ref.
T-
ΔT_{GNP-EP}
ΔT_{Ref}
(c)
Thermal resistance (^{0}C. cm^2/W)
Thickness (μm)
Viscosity (cP)
3050
380
234
(d)
GNP-862
Constantan
ΔT(K)
Time(s)
(e)
Through-plane, $\kappa_\perp$
Thermal conductivity, $\kappa_\perp$ (W/mK)
GNP-Epoxy 862
GNP-Silicon Oil
GNP-Hatcol 2372
(f)
In-plane, $\kappa_\parallel$
Through-plane, $\kappa_\perp$
Thermal conductivity (W/mK)
14%GNP grease
11%GNP grease
11%GNP film
11%GNP film

Figure 4.3 Measurements of anisotropic thermal conductivity in GNP-based thin thermal interface layers. (a), Schematic of TIM Tester for through-plane thermal conductivity measurements; (b), Schematic of the setup for in-plane thermal conductivity measurements of GNP-epoxy thin films by use of the comparison technique, and its experimental realization; (c), Thermal resistance as a function of thickness for the determination of through-plane thermal conductivity of thin TIM layers; (d), Thermal pulses along the GNP-epoxy thin film (red circles) and reference constantan wire (black squares) recorded during comparative technique data acquisition; (e), Through-plane ($\kappa_{\perp}$) thermal conductivities of GNP based greases for polymer matrices of different viscosities; (f), Through-plane ($\kappa_{\perp}$) and in-plane ($\kappa_{\parallel}$) thermal conductivities of thin GNP-epoxy layers.

The experimental setups for the through-plane and in-plane thermal conductivity measurements are presented in Fig.4.3a and Fig.4.3b, respectively, and were discussed in section 4.1.2. The through-plane thermal conductivities $\kappa_{\perp}$ of GNP-Silicon oil, GNP-Hatcol 2372 and GNP-Epoxy862 based composites at the same filler loading (14 wt.%) are presented in Fig. 4.3e and show a decrease of $\kappa_{\perp}$ with decreasing viscosity similar to the case of the through-plane electrical conductivity (Fig. 4.2b). Typical values of the through-plane thermal conductivity were $\kappa_{\perp}$ = 0.7 - 0.9 W/m*K for GNP loading between 11 and 14 wt.%. (Fig.4.3e). The in-plane thermal conductivity ($\kappa_{\parallel}$) of the GNP composite was measured by utilizing a comparative technique which was previously applied to the measurement of the thermal conductivities of carbon nanotube (CNT) bundles and CNT-epoxy composites.[31-33] This technique is not fully transferable to the grease samples and we found it necessary to cure the greases under pressure at elevated temperature, which resulted in thin film samples of thickness 100 to 300 μm. In order to preserve the GNP orientation throughout the curing, the processing conditions of the thin film were designed to mimic the parameters adopted in the TIM tester. As an internal check, Figure 4.3e includes data for both the in-plane ($\kappa_{\parallel}$) and through-plane ($\kappa_{\perp}$) thermal conductivities of the cured (solid film) specimens, together with results obtained on the grease samples.

Fig.4.3b shows the schematics and microscopy images of the experimental implementation of the comparative technique. The in-plane oriented

sample with lateral dimensions of 6×2 mm^2 and thickness ~200μm was cut from the cured GNP film. A thermal gradient was imposed by a miniature thermoelectric stage so as to direct the heat flow through the GNP sample and the 0.5 mm diameter constantan wire of known thermal conductivity (19.5 W/m*K), which was mounted in series. The sign of the temperature gradient was alternated by reversing the voltage at the thermoelectric stage and the results of the oppositely polarized measurements were averaged to exclude any contribution from black body radiation. Representative results from the experiments are included in Figure 4.3d in the form of the temperature gradients as a function of polarity. Measurements of several thin film samples gave value for the in-plane thermal conductivity of the GNP-based TIM layer of $\kappa_{\parallel}$ = 4.5± 0.5 W/m*K (Fig.4.3e) corresponding to an anisotropy in the thermal conductivity of ~5, which is very significant for TIM applications.

The electrical and thermal measurements show anisotropic electron and phonon transport in thin TIM layers which may originate from the preferential in-plane orientation of the GNPs; in order to directly address this question, we conducted SEM studies of the cross-sections of the GNP films. The resulting images are presented in Fig.4.4 and clearly indicate preferential in-plane orientation of the GNPs, thereby providing an obvious rationale for the observed anisotropy of the electrical and thermal conductivities.

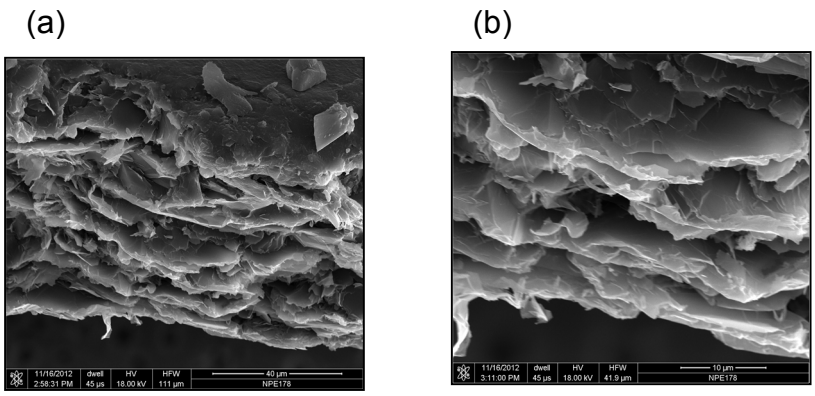

Figure 4.4 SEM images of the cross-section of a thin layer of the GNP-epoxy composite thin film at different magnifications with scale bars: (a) 40 μm and b) 10 μm.

The present measurements show strongly anisotropic electron and phonon transport in GNP-based thin TIM layers and the SEM study directly associates the observed anisotropy with the preferential in-plane alignment of the GNPs established during lateral flow of the GNP-based grease under applied pressure. The increase in the anisotropy of the electrical conductivity with decreasing viscosity of the polymer matrix (Fig.4.2) suggests that at low viscosities the polymer matrix is unable to resist the natural alignment of the GNPs. The decrease of the through-plane thermal conductivity with decreasing viscosity of the polymer matrix (Fig.4.3e) provides additional support for this interpretation. The thermal anisotropy is about two orders of magnitude smaller than the electrical anisotropy; this difference is not surprising taking into account

the fact that the electrical conductivities span a range of more than 30 orders of magnitude between the best electrical conductors such as copper ($\sigma \approx 6 \times 10^5$ S/cm) and electrical insulators such as Teflon ($\sigma \approx 10^{-26}$ S/cm), while the difference between the best thermal conductors such as graphite (~2000 W/m*K) and copper (~400 W/m*K), and thermal insulators such as Teflon (~0.25 W/m*K) is only 5 orders of magnitude.[35, 36] This can be explained by the fact that electronic component is dominated by the concentration of mobile electrons which is strongly material dependent. However these mobile electrons make a very small contribution to the thermal transport,[36] which is dominated by the phonons. Even when phonon scattering is very strong the localized vibrations in a solid material ensure a background contribution to the thermal transport which does not allow a dramatic decay and this minimizes the range of the thermal conductivities.

The quality of TIMs is typically evaluated by measurement of the thermal interface resistance R_{TIM}, which depends on the bulk thermal conductivity of TIM, the bond line thickness (BLT) of the TIM layer and the contact resistance R_C between the TIM and the contacting surfaces.[37] The thermal interface resistance can be decreased by increasing the bulk thermal conductivity of the TIM, reducing the BLT or reducing the contact resistance between the chip and heat sink.[27] Current commercially available thermal interface materials provide R_{TIM} in the range 0.1-0.4 °C-cm^2/W,[37-39] whereas it is anticipated that in the future, electronic packaging will require R_{TIM} in the range 0.05-0.01°C-cm^2 /W and a BLT in the

range 10-50 μm. Based on a BLT=20 μm, the required bulk thermal conductivity should be > 4 W/m*K which is in the range of the measured in-plane thermal conductivity of GNP based TIMs, but much higher than the current through-plane values.

4.1.4 Conclusion

The TIM layer is expected to provide efficient heat flow from the die to the heat sink in the direction normal to the thermal interface (Fig.4.1a), but we found that orientation of the GNPs follows the in-plane alignment pattern illustrated in Fig.4.1d, in contrast to ideal orientation of the GNPs normal to the thermal interface plane (Fig.4.1b); the latter orientation would take full advantage of the high in-plane thermal conductivity of graphite although the isotropic, random orientation of GNPs (Fig.4.1c) would be also acceptable. We suggest that the observed thermal anisotropy imposes a significant limitation on the performance of GNP fillers as the through-plane heat dissipation is crucial in thermal management applications; thus further practical advancements in this field will probably require the disruption of the in-plane orientation of the two-dimensional GNPs. Because the alignment in the thermal interface layer suppresses the through-plane component of the thermal conductivity, the anisotropy acts to strongly degrade the performance of the GNP-based composites in the geometry required for typical thermal management applications and must be taken into account in the future development of GNP-based thermal interface materials.

4.2 Application of hybrid fillers for improving the through-plane heat transport in graphite nanoplatelet-based thermal interface layers

4.2.1Introduction

In the previous section, we observed that the pre-dominantly in-plane alignment of 2D GNPs in thin TIM layers resulted in an increased in-plane electrical and thermal conductivity at the expense of the through-plane transport properties which were significantly suppressed.[40] GNP and boron nitride 2-D filler alignment has been reported by several groups,[17, 22, 28, 41] and has been found to be beneficial for some electronic packaging applications such as heat spreaders.[42, 43] However, in many cases the heat should be transferred across the TIM layers, so the suppression of the through-plane component of the heat conductance is detrimental for the performance of graphene-based fillers in thermal management applications. A promising direction for the enhancement of through-plane thermal conductivity is associated with utilization of vertically grown carbon nanotubes or aligned carbon fibers, but a remaining challenge appears to associated with the difficulty in achieving a sufficient loading of the filler in this configuration.[44-47]

The utilization of multicomponent fillers which include particles of different shapes and dimensions is a common practice in the manufacture of commercial TIMs.[48-53] Mostly, this is directed towards a more complete filling of the voids which must be occupied by the thermal interface layer including micro(nano)-cavities formed due to roughness of the contacting surfaces of the electronic

modules and the electronic packaging components. In recent work by the Haddon research group 1D CNTs and 2D GNPs were combined to formulate a hybrid filler which showed a synergistically enhanced bulk thermal conductivity as a result of decreasing inter-particle junction resistance within the hybrid heat conducting network.[15] In this section we utilize similar methods to study the combination of GNPs with conventional low aspect ratio aluminum (Al) and aluminum oxide (Al_2O_3) micro-particle fillers in order to suppress the in-plane alignment of the GNP filler and to enhance the through-plane component of the heat conductance.

4.2.2 Results and discussion

For this study, the size of isotropic spherical Al and Al_2O_3 microparticles was chosen to match the average lateral dimensions of ~10 μm (aspect ratio of ~ 300) of highly anisotropic GNPs[19] which intuitively should best serve to disrupt the in-plane alignment of the GNPs. Multiple individual and hybrid fillers formulations were tested and the resulting values of the thermal conductivities are presented in Fig. 4.5. The maximum practical filler loading was limited by the viscosity and spreadability of the thermal paste. The thermal conductivity was calculated from the slope of the dependence of thermal resistance on grease layer thickness (Fig 4.5a inset). For the single component Al micro-particle filler we observed typical percolation behavior with a strong upturn in the thermal conductivity in the 45-60 Vol% loading range at which point the concentration of

filler particles became sufficient to form a percolating thermally conducting network across the polymer matrix, in agreement with literature data.[54]

At low filler loadings (below 10 Vol%), the single component GNP filler is much more efficient than Al and Al_2O_3 spherical particles showing a linear increase of thermal conductivity with increasing filler loading in agreement with previous reports.[11, 18] However, the increasing viscosity and reduced spreadability of the paste limits the GNP loading to ~15-20 Vol% and within this range no sign of percolation is observed. The absence of percolation can be attributed to the high interparticle junction resistance in comparison with the intra-particle thermal resistance.[35]

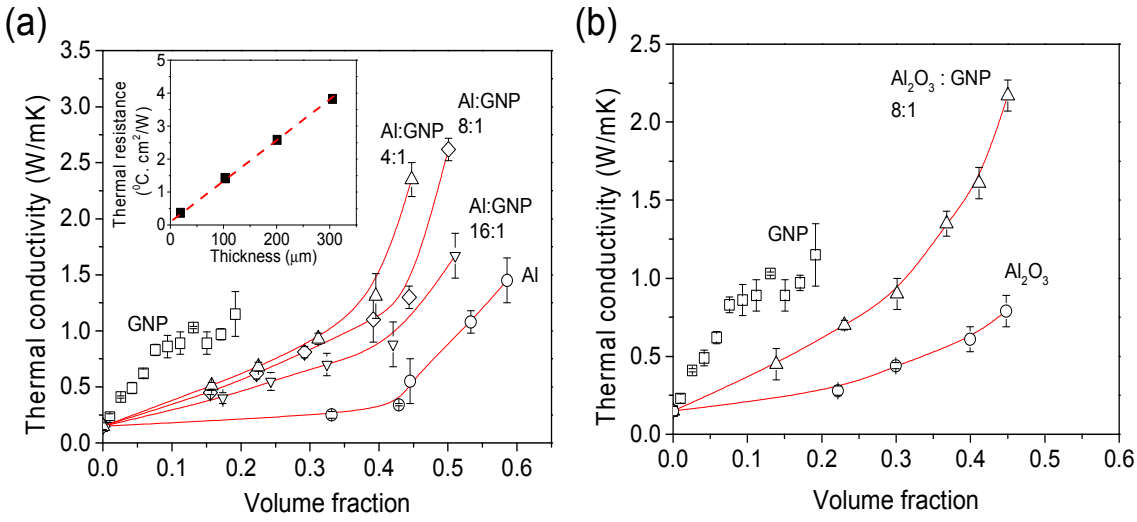

Figure 4.5 Through-plane thermal conductivity of the epoxy-based composites with (a) GNP-Al and (b) GNP-aluminum oxide hybrid fillers of different formulations as a function of the volume fraction of the hybrid filler. Inset in (a) shows an example of the dependence of the thermal resistance of the composite layer on the layer thickness utilized for calculation of through-plane electrical conductivity.

Hybrid filler formulations with volume proportions of Al and GNP fillers of 4:1, 8:1 and 16:1 produce greases which combine the advantages of the individual fillers as evidenced by the increasing slope of the dependence of thermal conductivity on the filler loading in the low loading range and the

percolation-induced sharp increase of thermal conductivity at high loadings (Fig.4.5a). The percolation threshold for hybrid fillers is lower than that of individual Al or Al_2O_3 fillers because of the high aspect ratio of GNP component. The highest gain in performance was achieved for an 8:1 Al to GNP volume ratio formulation resulting in a through-plane thermal conductivity of the grease, $\kappa_{\perp}$ = 2.6 W/mK, which is almost two times higher than the composites with individual fillers of similar viscosity and spreadability. Substitution of aluminum with aluminum oxide filler provide qualitatively similar results (Fig.4.5b), but with less pronounced percolation behavior, more likely, due to the almost order of magnitude lower intrinsic thermal conductivity of aluminum oxide. Nevertheless, aluminum oxide may have some other advantages because it can provide an electrically insulating thermal grease.[55-59] Below, we examine the origin of the improving performance of the hybrid fillers and evaluate the correlation of the observed enhancement of thermal conductivity with the degree of GNP in-plane alignment and its suppression upon addition of the spherically shaped filler.

Our study in the previous section demonstrated that the natural in-plane alignment of GNPs during formation of TIM layer leads to a high electrical anisotropy of the electrical conductivity with a ratio of in-plane ($\sigma_{\parallel}$) to through-plane ($\sigma_{\perp}$) components exceeding 1000.[40] Thus we used electrical anisotropy to qualitatively follow the suppression of the in-plane alignment of GNPs upon addition of spherically shaped filler particles. Electrically insulating Al_2O_3 particles

of diameter 10 μm were utilized for the electrical anisotropy measurements so that only the contribution of the electrically conductive GNP filler is assessed. Through-plane and in-plane electrical conductivity measurements were conducted on the layers of thermal grease placed on the sample stage of the TIM tester between two glass slides under the same pressure and temperature as in case of the thermal conductivity measurement so as to closely reproduce the formation of a TIM layer under normal operating conditions. The schematics of the 2-probe through-plane and 4-probe in-plane electrical conductivity measurements are presented in Fig.4.6a (inset) and Fig.4.6c (inset), respectively. Fig.4.6b and 4.6c show the through-plane and in-plane electrical conductivities of the greases with two filler formulations: i) thermal grease with a single filler of 5 Vol% GNP loading, and ii) thermal grease containing a hybrid filler combining 5 Vol% GNP and 40 Vol% Al_2O_3, and Fig.4.6d shows the electrical anisotropy of these greases. Greases with individual GNP (5 Vol%) fillers is strongly anisotropic with $\sigma_{\parallel}$ = 0.94 S/cm and $\sigma_{\perp}$ = 0.006 S/cm, and a corresponding anisotropy ratio $\sigma_{\parallel}/\sigma_{\perp}$ ~ 160. The hybrid filler grease shows increased through-plane conductivity $\sigma_{\perp}$ = 0.01 S/cm (fig.4.6b) and significantly decreased in-plane conductivity $\sigma_{\parallel}$ = 0.03 S/cm, which corresponds to a strongly decreased anisotropy, $\sigma_{\parallel}/\sigma_{\perp}$~3. These data provide a clear indication of the disruption of the in-plane alignment of the GNPs on addition of the Al_2O_3

spherical filler and we provide further information on this question in the SEM studies.

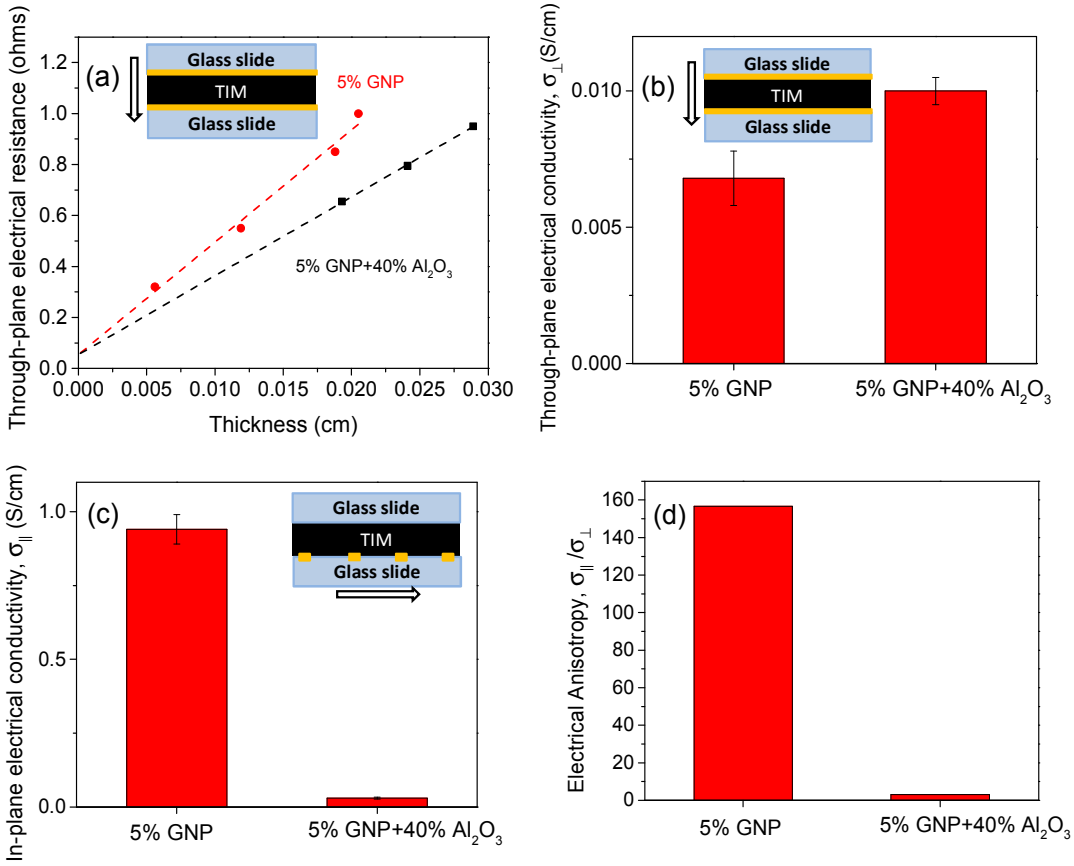

Figure 4.6 (a) Dependence of the 2 probe through-plane electrical resistance of TIM layer on layer thickness. (b) Through-plane, and (c) in-plane, electrical conductivities of GNP and GNP/Al_2O_3 hybrid composites. Insets show schematics of the electrical measurements. (d) Electrical anisotropy of the composites.

Scanning electron microscopy (SEM) imaging allows the direct observation of the orientation of GNPs in the TIM layer: the cross-sectional SEM images are presented in Fig.4.7.

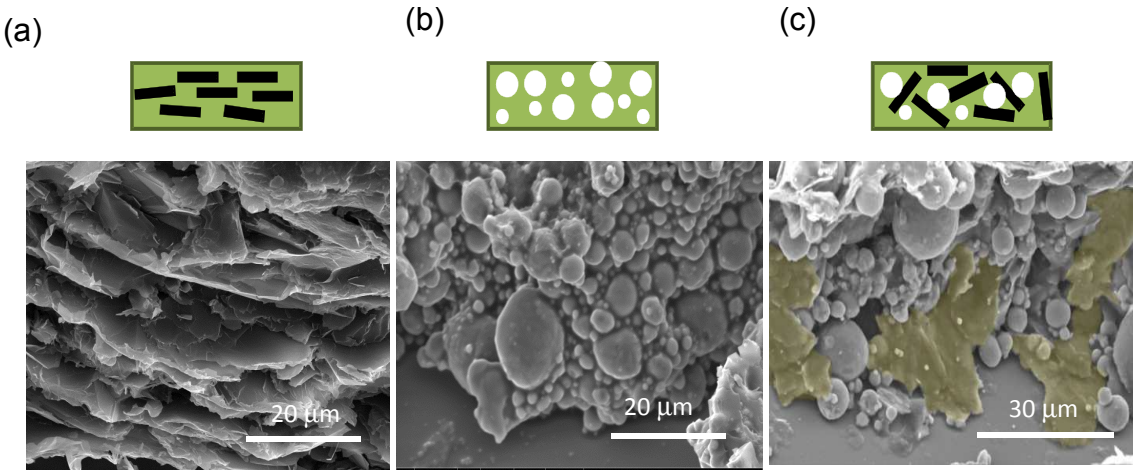

Figure 4.7 SEM imaging of cross-sections of composites with different fillers. (a) GNP filler; (b) Aluminum oxide filler; (c) hybrid GNP/Al_2O_3 filler. Schematics of filler particles orientation are presented on top of the SEM images.

Fig.4.7a clearly demonstrates in-plane alignment of the GNPs in agreement with our previous report.[40] Figure 3b shows that the Al_2O_3 filler which adopts a uniform, isotropic distribution of spherical particle of size 1-10 µm. In the case of the hybrid filler in Fig.4.7c, the in-plane alignment of the GNPs is disrupted by the presence of the Al_2O_3 spherical filler supporting the conclusions of the electrical anisotropy study.

Figure 4.8 summarizes the effect of hybrid filler formulation on the improvement of the through-plane thermal conductivity of the thermal greases in

terms of thermal conductivity enhancement, TCE = $(\kappa_{\perp} - \kappa_0)/ \kappa_0$, %, where κ_0 is thermal conductivity of uncured epoxy matrix, 0.15 W/mK, and $\kappa_{\perp}$ corresponds to the thermal conductivity of the particular filler formulation. As shown in Fig.4.8a, a GNP filler of loading 5.5 Vol% provides a TCE of ~400%, an Al filler of loading 44.5 Vol% provides TCE of ~370%, whereas combined, these loadings provide TCE of ~1750% which is more than twice the simple sum of the individual fillers contributions, thus showing the synergistic character of the enhancement. Similar results were obtained for combination of GNP and Al_2O_3 filler as shown in Fig. 4.8b. This synergistic enhancement of the through plane thermal conductivity of the TIM layer is in correlation with the disruption of GNPs in-plane alignment following the addition of the spherical filler, as confirmed by electrical anisotropy and SEM studies, leading to the improved through-plane percolating pathways for the heat transport. Performance of the hybrid filler can be further improved by tuning the filler formulation and decreasing the interparticle thermal resistance along the filler network and at the filler-polymer matrix interfaces, for example, by chemically modifying the surface of the filler components. This would allow achieving high TIM performance at lower filler loading in the range of optimum viscosity and spreadability of the thermal grease.[4]

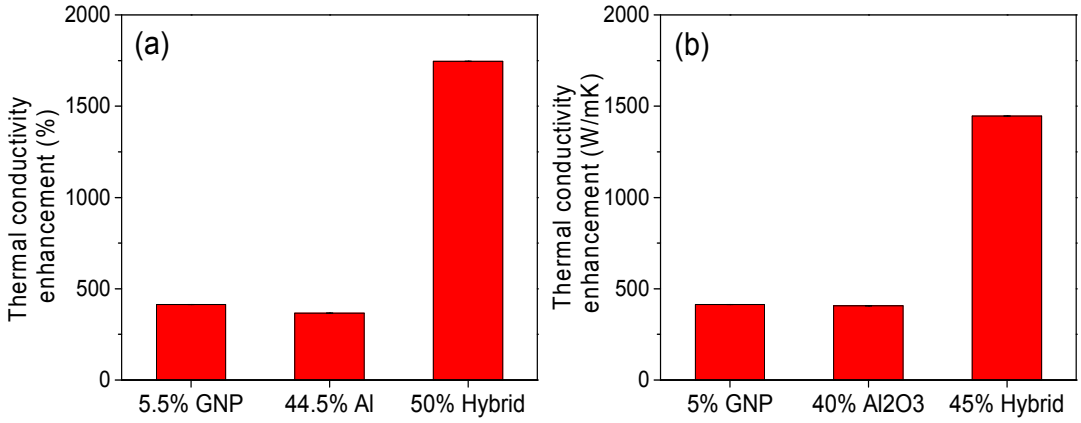

Figure 4.8 Through-plane thermal conductivity enhancement of hybrid fillers in comparison with the contribution of individual filler components: a) GNP/Al formulations; b) GNP/Al_2O_3 formulations.

4.2.3 Conclusion

In summary, disruption of the in-plane alignment of GNPs in thin thermal interface layer was achieved by addition of conventional spherical shape Al_2O_3 or Al filler particles. This disruption was confirmed by studies of the electrical anisotropy and SEM imaging. This hybrid filler formulation resulted in a synergistic enhancement of the through-plane thermal conductivity of the hybrid GNP/Al or GNP/Al_2O_3 based TIM layer. The enhancement of the out-of-plane orientation of GNPs therefore emerges as an important tool for expanding the potential of GNPs and other 2D fillers to contribute to high performance thermal management applications.

References

1. Schelling, P. K.; Shi, L.; Goodson, K. E. *Mater. Today* **2005,** 8, 30.
2. Prasher, R. *Proc. IEEE* **2006,** 94, 1571.
3. Xu, Y. S.; Chung, D. D. L. *Compos. Interfaces* **2000,** 7, 243.
4. Prasher, R. S.; Shipley, J.; Prstic, S.; Koning, P.; Wang, J. L. *ASME J. Heat Transfer* **2003,** 1170.
5. Lu, D.; Wong, C. P.; Prasher, R.; Chiu, C. P., Thermal Interface Materials. In *Materials for Advanced Packaging*, Springer US: 2009; pp 437.
6. Geim, A. K.; Novoselov, K. S. *Nature Mater.* **2007,** 6, 183.
7. Dresselhaus, M. S.; Dresselhaus, G.; Eklund, P. C.; Chung, D. D. L. *Mater. Sci. Eng.* **1977,** 31, 141.
8. Chung, D. D. L. *J. Mater. Sci.* **1987,** 22, 4190.
9. Yasmin, A.; Daniel, I. M. *Polymer* **2004,** 45, 8211.
10. Fukushima, H.; Drzal, L. T.; Rook, B. P.; Rich, M. J. *J. Therm. Anal. Calorim.* **2006,** 85, 235.
11. Yu, A.; Ramesh, P.; Itkis, M. E.; Bekyarova, E.; Haddon, R. C. *J. Phys. Chem. C* **2007,** 111, 7565.
12. Kalaitzidou, K.; Fukushima, H.; Drzal, L. T. *Carbon* **2007,** 45, 1446.
13. Debelak, B.; Lafdi, K. *Carbon* **2007,** 45, 1727.
14. Ganguli, S.; Roy, A. K.; Anderson, D. P. *Carbon* **2008,** 46, 806.
15. Yu, A., et al. *Adv. Mater.* **2008,** 20, 4740.
16. Lin, C.; Chung, D. D. L. *Carbon* **2009,** 47, 295.

17. Veca, L. M., et al. *Adv. Mater.* **2009,** 21, 2088.

18. Kim, S.; Drzal, L. T. *Sol. Energy Mater. Sol. Cells* **2009,** 93, 136.

19. Sun, X.; Ramesh, P.; Itkis, M. E.; Bekyarova, E.; Haddon, R. C. *J. Phys.: Condens. Matter* **2010,** 22, 334216.

20. Sun, X., et al. *J. Electron. Packaging* **2011,** 133, 020905.

21. Yavari, F., et al. *J. Phys. Chem. C* **2011,** 115, 8753.

22. Raza, M. A.; Westwood, A.; Brown, A.; Hondow, N.; Stirling, C. *Carbon* **2011,** 49, 4269.

23. Raza, M. A.; Westwood, A.; Stirling, C. *J. Mater. Sci.* **2012,** 47, 1059.

24. Shahil, K. M. F.; Balandin, A. A. *Nano Lett.* **2012,** 12, 861.

25. Xiang, J.; Drzal, L. T. *Sol. Energy Mater. Sol. Cells* **2011,** 95, 1811.

26. Kooi, C. C., et al. In *Capillary Underfill and Mold Encapsulation Materials for Exposed Die Flip Chip Molded Matrix Array Package with Thin Substrate*, Electronics Packaging Technology, 2003 5th Conference (EPTC 2003), 2003; 2003; pp 324.

27. Samson, E. C., et al. *Intel Tech. J.* **2005,** 09, 75.

28. Xiang, J. L.; Drzal, L. T. *Carbon* **2011,** 49, 773.

29. Song, W. L., et al. *Angew. Chem. Int. Ed.* **2012,** 51, 6498.

30. Li, J.; Kim, J. K. *Compos. Sci. Technol.* **2007,** 67, 2114.

31. Hone, J., et al. *Appl. Phys. Lett.* **2000,** 77, 666.

32. Biercuk, M. J., et al. *Appl. Phys. Lett.* **2002,** 80, 2767.

33. Tritt, T. M., *Thermal Conductivity: Theory, Properties and Applications*. Kluwer Academic/Plenum Publishers: New York, New York, 2004; p 290.

34. Raza, M. A.; Westwood, A. V. K.; Brown, A. P.; Stirling, C. *Comp. Sci. Technol.* **2012,** 72, 467.

35. Shenogina, N.; Shenogin, S.; Xue, L.; Keblinski, P. *Appl. Phys. Lett.* **2005,** 87, 133106.

36. Itkis, M. E.; Borondics, F.; Yu, A.; Haddon, R. C. *Nano Lett.* **2007,** 7, 900.

37. Gwinn, J. P.; Webb, R. L. *Microelectron. J.* **2003,** 34, 215.

38. Narumanchi, S.; Mihalic, M.; Kelly, K.; Eesley, G. In *Thermal Interface Materials for Power Electronics Applications* NREL/CP 540-42972 Itherm Conference Florida, USA, May, 208, 2008; Florida, USA, 2008.

39. Liu, J., et al. In *Recent progress of thermal interface material research - an overview*, Thermal Inveatigation of ICs and Systems, 2008. THERMINIC 2008. 14th International Workshop on, 24-26 Sept. 2008, 2008; 2008; pp 156.

40. Tian, X.; Itkis, M. E.; Bekyarova, E.; Haddon, R. C. *Sci. Rep.* **2013,** 3, 1710.

41. Tanimoto, M.; Yamagata, T.; Miyata, K.; Ando, S. *ACS Appl. Mater. Interfaces* **2013,** 5, 4374.

42. Mahajan, R.; Chiu, C. P.; Chrysler, G. In *Cooling a Microprocessor Chip*, Proceedings of the IEEE, August 2006, 2006; 2006.

43. Moore, A. L.; Shi, L. *Mater. Today* **2014,** 17, 163.

44. Chhowalla, M., et al. *J. Appl. Phys.* **2001,** 90, 5308.

45. Murakami, Y., et al. *Chem. Phys. Lett.* **2004,** 385, 298.

46. Tong, T., et al. *IEEE Trans. Compon. Packag. Technol* **2007,** 30, 92.

47. Uetani, K., et al. *Adv. Mater.* **2014,** 26, 5857.

48. Peterson, A. L. In *Silicons with Improved Thermal Conductivity for Thermal Management in Electronic Packaging*, Electronic Components and Technology Conference, Las Vegas, NV, 20-23 May 1990, 1990; IEEE: Las Vegas, NV, 1990; pp 613.

49. Xu, Y. S.; Chung, D. D. L.; Mroz, C. *Composites Part A* **2001,** 32, 1749.

50. Hu, X.; Jiang, L.; Goodson, K. E. In *Thermal Conductance Enhancement of Particle-Filled Thermal Interface Materials Using Carbon Nanotube Inclusions*, 9th Intersoc. Conf. Thermal and Thermomechanical Phenomena in Electronic Systems, Las Vegas, NV, 1-4 June 2004, 2004; Las Vegas, NV, 2004; pp 63.

51. Lee, G. W.; Park, M.; Kim, J.; Lee, J. I.; Yoon, H. G. *Composites Part A* **2006,** 37, 727.

52. Yung, K. C.; Liem, H. *J. Appl. Poly. Sci.* **2007,** 106, 3587.

53. Teng, C.-C.; Ma, C.; Chioub, K.; Lee, T.; Shih, Y. *Mater. Chem. Phys.* **2011,** 126, 722.

54. Prasher, R. S.; Koning, P.; Shipley, J.; Devpura, A. *J. Electron. Packaging* **2003,** 125, 386.

55. Das, S. K.; Putra, N.; Thiesen, P.; Roetzel, W. *J. Heat Transfer* **2003,** 125, 567.

56. Sim, L. C.; Ramanan, S. R.; Ismail, H.; Seetharamu, K. N.; Goh, T. J. *Thermochimica Acta* **2005,** 430, 155.

57. Lin, C. G.; Howe, T. A.; Chung, D. D. L. *J. Electron. Mater.* **2007,** 36, 659.

58. Im, H.; Kim, J. *J Mater Sci* **2011,** 46, 6571.

59. Lingamneni, S.; Marconnet, A. M.; Goodson, K. E. In *3D Packaging Materials Based on Graphite Nanoplatelet and Aluminum Nitride Nanocomposites*, Proceedings of the ASME 2013 International Mechanical Engineering Congress and Exposition, San Diego, California, USA, November 15-21, 2013; San Diego, California, USA, 2013.

Conclusions

The new low dimensional carbon allotropes, including single-walled carbon nanotubes (SWNTs) and graphene, have attracted strong interest because of their unique properties and wide applications. During my graduate study, I focused on the organometallic chemistry of SWNTs and GNPs, graphene derivatives from chemical functionalization and GNPs as fillers in thermal interface materials.

There are four different kinds of interactions between metal atoms and graphitic surfaces. a) Weak physisorption of metal atoms, which generally happens when the metal atom has filled d-orbitals (such as gold) (b) Ionic doping chemisorption interaction from metals of low ionization energy such as alkali metals (Li, Na, K) and alkaline earth metals (Ca, Sr, Ba). Metals with low work function result in the injection of electrons into the conduction band of graphitic materials (n-type doping). (c) Covalent chemisorption of metals to graphitic systems leads to strong (destructive) rehybridization of the graphitic band structure. One such example is the formation of metal carbides. My PhD study is focused on understanding the effect of covalent chemisorption of Group 6 transition metals on the conductivity of SWNT networks. The formation of organometallic hexahapto (η^6)−metal bonds, such as those in (η^6-SWNT)-Cr-(η^6 -SWNT), preserves the graphitic band structure (constructive rehybridization, d) and by interconnecting adjacent graphitic surfaces it significantly reduces the

internanotube electrical junction resistance in SWNT networks. The organometallic hexahapto functionalization of SWNTs with transition metals does not cause significant structural rehybridization of the graphitic surface, providing a new way for modification of graphitic structures that does not saturate the functionalized carbon atoms. This type of functionalization preserves the structural integrity and maintains the delocalization in these extended periodic π-electron systems, thus offering the possibility for three dimensional (3D) interconnections between adjacent graphene surfaces.

Graphene oxide is the precursor for a range of graphene derivatives. This thesis presents optical and electronic characterization of graphene oxide derivatives – reduced graphene oxide (RGO) and octadecylamine-functionalized RGO. Chemical reduction of graphene oxide is applied to restore the electronic conjugation and the degree of restoration is characterized by absorption spectroscopy, Raman, and electrical conductivity measurements. The materials produced by ODA functionalization provide organic solubility, and partially regenerate the π-conjugation. Importantly, a correlation between the optical properties of these materials in solution and film form is presented.

GNPs are applied as fillers in thermal interface materials because of their outstanding thermal conductivity along graphene layer surface and high aspect ratio. In practical applications, the GNPs align along the in plane direction indicated by anisotropy of transport properties and SEM images on the cross

section. The alignment prohibits the efficiency of thermal interface materials since it is the through-plane direction that heat generated by electronics transfers to the heat sink. 3D sphere particles are added to interrupt the alignment. The hybrid fillers decrease the anisotropy of electrical properties, and results in synergistic enhancement of through-plane thermal conductivity.